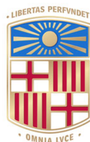

UNIVERSITAT DE BARCELONA

Multiscale Modeling of Organic Electronic Biosensor Response

Larissa Huetter

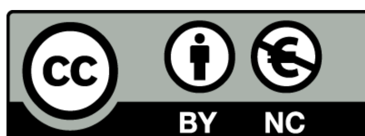

Aquesta tesi doctoral està subjecta a la llicència ***Reconeixement- NoComercial 4.0. Espanya de Creative Commons***.

Esta tesis doctoral está sujeta a la licencia ***Reconocimiento - NoComercial 4.0. España de Creative Commons.***

This doctoral thesis is licensed under the ***Creative Commons Attribution-NonCommercial 4.0. Spain License.***

Multiscale Modeling of Organic Electronic Biosensor Response

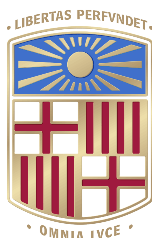

UNIVERSITAT DE BARCELONA

FACULTY OF PHYSICS

Doctoral Thesis
submitted by
M.Sc. Larissa Huetter

under supervision of
Prof. Dr. Gabriel Gomila
2022

Modelado Multiescala de la Respuesta de Biosensores Electrónicos

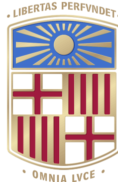

UNIVERSITAT DE BARCELONA

Memoria presentada para optar al grado de doctor por la Universitat de Barcelona.

Programa del doctorado en Biomedicina
Autora Larissa Huetter
Director y Tutor Prof. Dr. Gabriel Gomila
Lugar de realización de la tesis Instituto de Bioingeniería de Cataluña

M. Sc. Larissa Huetter

Doctoral program in biomedicine, biomedical engineering research line at the Universitat de Barcelona, Faculty of Physics.

In cooperation with In cooperation with Institute for Bioengineering of Catalonia, Nanoscale bioelectrical characterization.

This project has received funding from the European Union's Horizon 2020 research and innovation program, under the Marie Sklodowska- Curie grant agreement no. 813863.

Für meine Oma, in der Hoffnung, eines Tages wie sie zu sein.

"You cannot hope to build a better world without improving the individuals."
Marie Skłodowska–Curie

Abstract

There have been significant advances in organic bioelectronic devices in recent years. These devices are capable of stimulating excitable cells and can generate data to facilitate disease diagnostics and monitoring. Electrolyte-gated organic field-effect transistors (EGOFETs) are powerful organic bioelectronic devices. EGOFETs are a group of thin-film transistors used as the sensing units within organic bioelectronic devices due to their ability to strongly amplify the signal and natural biocompatibility [1]. EGOFETs can detect minor voltage variations of electrically excitable cells [2] or when analyzing biomarkers. Organic semiconductors offer various advantages over inorganic ones, such as low-cost production, flexibility, printability as well as allowing easy integration into sensing devices or textiles [3].

Due to the lack of specific physical-mathematical modeling of EGOFETs, they are often approximated using ideal field-effect transistor (FET) models. Whilst these models can be useful, they are not capable of accommodating ionic diffusion effects generated by nanoscale variations at the electrolyte/semiconductor and electrolyte/gate interfaces within EGOFETs. This thesis presents the a finite element model of EGOFETs to provide a deeper physical understanding of these devices. We show the changes in the macroscale current correlated to the nanoscale conductivity when changing the device geometries. Further, we observe the voltage shifts due to ionic concentrations and evaluate the role of interfacial layers and fixed charges at the gate electrode.

Different levels of complexity of the models have been considered. The simpler Helmholtz model, where the electrolyte is mimicked as a Helmholtz capacitance, was selected initially. Using this, we determined that many of the transfer and output current-voltage curves of EGOFETs could be reproduced. This enabled the identification of local conductivity changes in the different operating regimes.

We subsequently expanded the physical model by incorporating the electrolyte's ionic diffusive effects and compact interfacial layers' presence using the Nernst-Planck-Poisson (NPP) framework. Initially, a one-dimensional capacitor structure model was used to gain fast results without neglecting the physics of the device. This model demonstrated the change in device characteristics following the addition of biorecognition layers to the gate electrode for biosensing applications. Developing this further, we considered the NPP model in two-dimensional structures, which allowed investigating changes to device geometry, including channel and gate length in the NPP framework. This provides a deep insight into the voltage and charge density distributions to reveal the formation of space charge layers, including accumulation and ionic diffusive layers. The potential profiles over semiconductors and electrolytes demonstrate the differences in charge accumulation for gate modifications with self-assembled monolayers, ion concentrations, and material parameters. We correlate the charge accumulation along the conductive channel with the distribution of ions. The results of these studies allowed us to provide further explanations of the behavior of EGOFETs and have opened the door to a rational design and characterization of the devices for future biosensing applications.

Resumen

Los dispositivos bioelectrónicos orgánicos han avanzado enormemente en los últimos años. Estos dispositivos se están desarrollando para estimular células excitables y controlar y detectar analitos para el diagnóstico de enfermedades. Entre los distintos dispositivos electrónicos orgánicos que se están desarrollando, los transistores orgánicos de efecto de campo con electrolitos (EGOFET) desempeñan un papel esencial. Los EGOFET se utilizan como dispositivos de detección ya que tienen un carácter de amplificación grande y son naturalmente biocompatibles [1]. Los EGOFET forman parte de un grupo de transistores de una capa fina que utilizan un semiconductor orgánico rodeado por una solución iónica. Son capaces de registrar pequeñas variaciones de voltaje cuando se detectan biomarcadores o se monitorizan células eléctricamente excitables [2]. Un semiconductor orgánico ofrece varias ventajas, como el bajo coste de producción, la flexibilidad y la posibilidad de impresión, lo que permite una integración fácil en dispositivos o tejidos [3].

Actualmente, no existen modelos físico-matemáticos específicos para modelar los EGOFET. Debido a esto, su caracterización y descripción se realiza comúnmente utilizando modelos de transistores de efecto de campo (FET) ideales. Sin embargo, en los EGOFET, las variaciones a la nanoescala en las interfaces electrolito/semiconductor y electrolito/puerta controlan la respuesta del dispositivo, incluidos los efectos de difusión iónica. El modelo ideal de los FET no tiene en cuenta estos efectos y, por tanto, no es adecuado para reproducir toda la física de los EGOFET.

Esta tesis presenta un modelo físico de los dispositivos EGOFET con el fin de proporcionar una comprensión física más profunda de estos dispositivos. Se han considerado diferentes niveles de complejidad de los modelos. El punto de partida fue el modelo de Helmholtz en dos dimensiones, en el que el electrolito se modela como una capacitancia de Helmholtz. Demostramos que, con esta simplificación, ya podemos reproducir muchas de las curvas de transferencia y de

corriente-tensión de salida de los dispositivos EGOFET y permite visualizar los cambios locales de conductividad en los diferentes regímenes de funcionamiento. A continuación, generalizamos el modelo físico de Helmholtz incorporando los efectos iónicos difusivos en el electrolito y la presencia de capas interfaciales compactas, modelando los EGOFET en el marco de la teoría de Nernst-Planck-Poisson (NPP). En el primer paso, consideramos un modelo para una estructura unidimensional con el fin de obtener resultados rápidos sin descuidar la física del dispositivo. Este modelo permitió investigar ya los cambios en las características del dispositivo cuando se usa en aplicaciones biosensoras, como por ejemplo, cuando se añaden capas de bioreconocimiento al electrodo de puerta. En un segundo paso, consideramos el modelo NPP en estructuras de dos dimensiones. Con este modelo, pudimos investigar los efectos de la geometría del dispositivo, incluyendo la longitud del canal y de la puerta en el marco de la teoría NPP, y obtener una visión profunda de las distribuciones de voltaje y densidad de carga dentro del dispositivo, que revelan la formación de capas de carga espacial, como capas de acumulación y capas iónicas difusivas. Con estos estudios, hemos podido ofrecer una comprensió física más amplia sobre el comportamiento de los EGOFET y hemos abierto la puerta a poder realizar un diseño y caracterización racionales de estos dispositivos para futuras aplicaciones como biosensores.

Acknowledgments

First, I want to thank my supervisor Prof. Dr. Gabriel Gomila, for teaching me so much over these past three years. Thank you for your valuable comments, suggestions and ideas, which taught me a lot, personally and academically. Thank you to Adrica for giving me the chance to be part of this project and thank you to the current and former members of the Nanoscale Bioelectrical Characterization group at IBEC. I will always be thankful for my family, friends, Matthi, Tanja and Corinna and their understanding and support. You have always been there for me. I want to especially thank my parents for supporting me with the many ideas I had, the stays abroad and for making my path until here possible. Thank you, Mama, for leading me through school with long hours of studying, even until I fell asleep. Thank you, Papa, for the patience to teach me programming and many more things which have provided me with the most valuable skills throughout my Ph.D. Thanks to my parents and my grandma, Gisela, for giving me good advice, even when I am mostly far away from home.

I am very grateful for the people I met on the BORGES team and that we could take this journey together. We had a lot of fun in network meetings, regardless of the pandemic situation, which gave us an additional challenge in this project. I want to thank the people who made my secondments a great time and helped me in the writing stage of my thesis: Panos, Pamela, Kateryna and Roger. Thousands of thanks for correcting these pages, especially to my dad, Panos and Tobias.

I want to thank Paul Docherty, who encouraged me to enroll in a Ph.D. program, believed in me and gave me the chance to experience the researcher's life.

Finally, I want to remark on the great chances the European Commission created with the Marie Skłodowska-Curie Actions under Horizon 2020. These networks create opportunities for international cooperation and interdisciplinary working, where people will benefit from collaboration and skills far beyond the Ph.D.

Abbreviations

BC	Boundary condition
BDF	Backward differentiation formula
EDL	Electrical double layer
EGOFET	Electrolyte-gated organic field-effect transistor
FEM	Field effect transistor
FET	Field-effect transistor
MES	Metal\Electrolyte\Semiconductor
MOSFET	Metal oxide semiconductor field effect transistor
NPP	Nernst-Planck-Poisson
OECT	Organic electrochemical transistor
OFET	Organic field effect transistor
OLED	Organic light emitting diode
OTFT	Organic thin film transistor
PDE	Partial differential equation
SAM	Self-assembled monolayer
TFT	Thin-film transistor

List of Publications

Parts of this thesis have been published in the following publications and conferences:

- **Larissa Huetter**, Adrica Kyndiah, Gabriel Gomila, *Analytical Physical Model for Electrolyte Gated Organic Field Effect Transistors in the Helmholtz Approximation*, (under preparation)

- **Larissa Huetter**, Adrica Kyndiah, Gabriel Gomila, *Analytical Physical Modelling of Organic Metal-Electrolyte-Semiconductor Capacitors*, (under preparation)

- **Larissa Huetter**, Adrica Kyndiah, Gabriel Gomila, *Physical Modelling of Electrolyte Gated Organic Field Effect Transistors in the Nernst-Planck-Poisson framework*, (under preparation)

List of Conferences

Parts of this thesis have been presented in the following conferences and symposiums:

- Biosensors for Pandemics, Online conference, 2020
- 13th IBEC Symposium - Bioengineering for Future and Precision Medicine, Barcelona, Spain 2020, Poster, *Multiscale Modeling of Organic Electronic Biosensor Response*,
  Larissa Huetter, A. Kyndiah, G. Gomila
- COMSOL Conference, Online conference, 2020
- 14th IBEC Symposium - Bioengineering for Regenerative Therapies, Barcelona, Spain 2021, Poster, *Multiscale Modeling of Organic Electronic Biosensor Response* ,
  Larissa Huetter, A. Kyndiah, G. Gomila
- Materials Research Society (MRS) Fall Meeting, Boston, USA 2021, Poster, *Nernst-Planck-Poisson Modelling of EGOFET Biosensors*,
  Larissa Huetter, A. Kyndiah, G. Gomila
- BioEl - International Winter School on Bioelectronics, Kirchberg, Austria 2022, Poster, *Multiscale Modeling of Organic Electronic Biosensor Response*,
  Larissa Huetter, A. Kyndiah, G. Gomila
- Materials Research Society Spring Meeting, Honolulu, USA 2022, Oral, *Role of interfacial layers in the performance of EGOFET-biosensors*,
  Larissa Huetter, A. Kyndiah, G. Gomila

Contents

Abstract i

Resumen iii

Acknowledgments v

Abbreviations vii

List of Publications and Conferences ix

I Fundamentals 1

1 Introduction 3
- 1.1 EGOFETs as Biosensors 5
- 1.2 Operating Principle of an EGOFET 6
  - 1.2.1 Electrical Double Layer 10
  - 1.2.2 Interfacial Capacitances and Fixed Charges 12
  - 1.2.3 Current-Voltage Characteristics of an EGOFET 13
- 1.3 Physics of Organic Semiconductors Devices 17
  - 1.3.1 Inorganic and Organic semiconductors 17
  - 1.3.2 Charge Transport in Organic Semiconductors 18
  - 1.3.3 The Drift-Diffusion Transport Model for Semiconductor Devices 21
  - 1.3.4 Nernst-Plank-Poisson Model 21
- 1.4 Finite-Element Numerical Modelling 23
  - 1.4.1 Meshing 24
  - 1.4.2 Boundary Conditions 25
  - 1.4.3 Solving the Equations 25

1.5 State of the Art in Numerical Modeling of EGOFETs 26
1.6 Aim of the thesis 29
1.7 Structure of the Thesis 31
1.8 Summary 32

II Methods 33

2 Finite-Element Modeling of EGOFETs 35
2.1 Two-dimensional Helmholtz Model 36
2.1.1 Description of the Model 36
2.1.2 Implementation of the Model in COMSOL Multiphysics 38
2.2 Nernst-Planck-Poisson Model 40
2.2.1 Description of the Model 40
2.2.2 Implementation of the 1D Model in COMSOL Multiphysics 44
2.2.3 Implementation of the 2D Model in COMSOL Multiphysics 47
2.3 Solver and Time-Step Adjustment 50
2.4 Model Validation and Verification 51
2.4.1 Verification of the 2D Helmholtz Model Implementation 51
2.4.2 Verification of the 1D NPP Model Implementation 54
2.4.3 Verification of the 2D NPP Model Implementation 58
2.4.4 Stationary Condition 61
2.5 Summary 66

III Results 67

3 EGOFET in the Helmholtz Approximation 69
3.1 Current-Voltage Characteristics 70
3.2 Semiconductor Conductivity Distribution and Voltage Dependence 74
3.3 Summary 84

4 MES Capacitor in the NPP Framework 85
4.1 Potential and Charge Distribution 86
4.2 Ionic Diffusive Effects on the Sheet Semiconductor Conductivity 89
4.3 Threshold Voltage Dependency on the Source-Gate Voltage . . . 91
4.4 Effect of the Interfacial Layers on the Semiconductor Conductivity 93
4.4.1 Self-Assembled Monolayer Interfacial Layers 94

4.4.2 Localization of the Distributed Interfacial Capacitances . 98
4.4.3 Influence of Fixed Charges at the Gate Electrode Functionalization Layer 99
4.5 Influence of the Ionic Strength of the Electrolyte 102
4.6 Summary 104

5 EGOFET two-dimensional model in the NPP framework 105
5.1 Current-voltage characteristics 106
5.2 Electric Potential Distribution 109
5.3 Free Carriers Concentration Distribution 112
5.4 Local Sheet Semiconductor Conductivity Distributions 115
5.5 Influence of Material Parameters 120
5.5.1 Hole Mobility of the Semiconductor 120
5.5.2 Injected Hole Concentration in the Semiconductor 122
5.6 Influence of Device Geometry 125
5.6.1 Influence of the Channel Length 125
5.6.2 Influence of the Gate Length 127
5.7 Summary 129

IV Final Remarks 131

6 Discussion 133

7 Conclusion and Perspectives 137

A Appendix 1 141

B Appendix 2 147

C Appendix 3 149

D Appendix 4 153

E Appendix 5 159

F Constants and Units 161

References 163

PART I

FUNDAMENTALS

Chapter 1

Introduction

Semiconductor-based technologies are one of the great advances of the last centuries. Our everyday electronics, like computers and phones, are made possible by this innovation. Semiconductors can act as a conductor, allowing an electrical current to flow like in metal and similarly stopping the electrical current, acting as an insulator. The semiconductor market is still rising, predicted to be doubled in the next ten years [4]. Inorganic semiconductors dominate the market, whereas silicon is the most common.

In 2000 when the Nobel Prize for chemistry was awarded for discovering conducting polymers [5], a new era for organic semiconductors began. Conducting polymers combines two major technological inventions of the last century: plastics and electronics. Organic semiconductors paved the way for future applications that will resolve everyday problems or improve existing solutions. Organic electronics offer several advantages: they are cheap, flexible, printable, and naturally biocompatible [6]. Organic materials contain carbon-hydrogen bonds or consist of carbon-rich compounds [7]. Recently, organic electronics made the step to real-life applications, like organic light-emitting diode (OLED) displays [8, 9]. OLEDs are self-illuminating, which leads to energy-efficient, thin, lightweight, and flexible displays. OLED displays are a rising multibillion-dollar industry [10]. So what are the future opportunities organic electronics are offering? Currently, researchers are exploring the field of organic transistors and their use in bioelectronics.

Transistors in electronic devices usually contain inorganic semiconductors. Substituting the inorganic with an organic semiconductor allows the transistor to

attach biological components like cells and proteins. Organic thin-film transistors (OTFTs) are easy to produce, even at room temperature, cheap, and printable [11]. Different types of OTFTs are organic field-effect transistors (OFETs), electrolyte-gated field-effect transistors (EGOFETs), and electrochemical transistors (OECTs). This thesis focuses on EGOFETs, where a more detailed description is given in Section 1.2.

Biosensors based on organic transistors are of particular interest for healthcare monitoring [12] as their advantages offer a variety of cheaper and faster solutions, as there is a wide range of biocompatible organic semiconductors, making them suitable for next-generation medical technologies [3, 13] . With these applications, organic semiconductor devices can fill a niche in healthcare devices, where conventional inorganic electronics are reaching their limits. The following sections give an overview of the motivation and functionality of EGOFETs as a biosensor and the open questions addressed in this thesis.

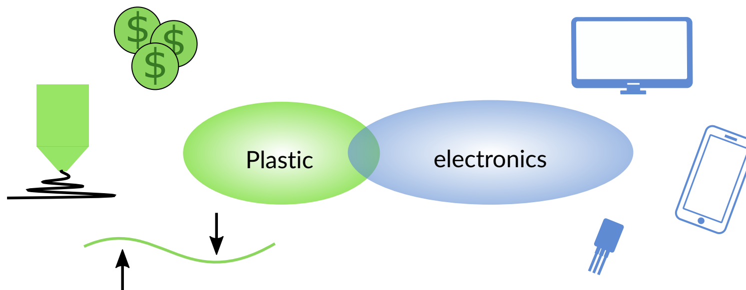

Figure 1.1: Plastic electronics offer printability, flexibility, and low-cost fabrication. Electronic devices like transistors are used daily in phones and computers and recently in organic light-emitting diodes (OLEDs) [8].

1.1 EGOFETs as Biosensors

OFETs are promising in healthcare applications as they are cheap, flexible, and naturally biocompatible. Of particular interest is the usage of EGOFETs and OECTs as biosensors. A biosensor provides an output signal corresponding to a biological signal [14]. Examples of biosensors are pregnancy tests or glucose meters to monitor diabetic patients. A biosensor is a device composed of i) a biorecognition unit/element, ii) a transducer that converts the binding event into a measurable signal, and iii) the read-out that displays the sensor response. A biorecognition element (e.g., antibody, enzymes, aptamers) binds specifically to the analyte of interest in those applications. The transistor transduces the binding event into an electrical signal. Ultimately, this allows the detection of diseases by employing an electrical signal. This approach can simplify and speed up prognosis and disease detection at a low cost.

Since the signal from biorecognition events is very low, researchers try to amplify it by introducing novel transistor configurations based on conductive polymers. One example of this new architecture is the EGOFET [15]. This transistor type offers fast response and high stability [3] while it can be intimately coupled with biological matter [16] compared to inorganic transistors. EGOFETs can be used to detect biomarkers, and it has been shown that monitoring electrically active cells is also possible, along with studying the effect of different drugs [2].

Organic electronics have gained widespread attention in the scientific and industrial community. However, we still require a deeper understanding of its functionalities to make EGOFET-based biosensors reliable and suitable for real-world applications.

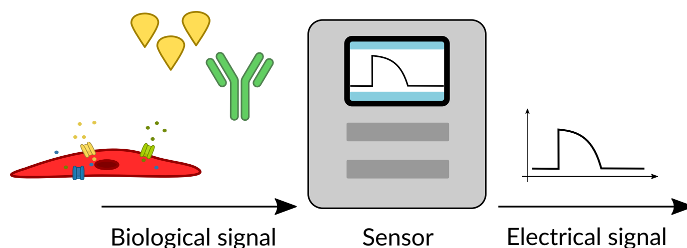

Figure 1.2: A biosensor transforms biological signals into an electrical or optical signal.

1.2 Operating Principle of an EGOFET

A field-effect transistor (FET) contains three electrodes: source, drain, and gate. The source-drain voltage drives the current between source and drain, whose magnitude is controlled electrically by the source-gate and source-drain voltage. To understand the principle of a FET, Figure 1.3 shows an analogy based on a pipe with a gate-controlled water flow. (a) When the gate between source and drain is closed, no current flows. (b) A current from the source to the drain flows when the gate is opened. The more the gate opens, the higher the current. (c) To increase the current further, the source-drain gradient has to be increased. This reaches a limit where the current is no longer dependent on the source-drain potential and only on the gate's opening.

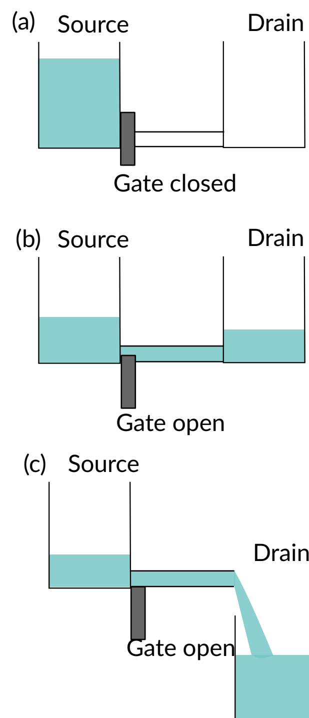

Figure 1.3: Principle of gating the current between source and drain. (a) The gate is closed, and no current flows. (b) The gate is opened. The current depends on the channel's open cross-section and the source and drain potential. (c) The potential between source and drain increases because the current only depends on the gate.

The characteristic structure of an EGOFET is shown in Figure 1.4. The organic semiconducting material is placed between source and drain, while an electrolyte (instead of a solid dielectric like in conventional FETs) is placed between the gate and the semiconductor film. In an EGOFET, the gate electrode is usually immersed in the electrolyte [17]. A transversal electric field is built up when a voltage of the appropriate value and sign is applied at the gate electrode, promoting the injection of holes from the source to the semiconductor film. Consequently, the semiconductor conductivity varies, and so does the electrical current flowing between the source and drain in response to a source-drain voltage.

Because of the amplifying behavior of a transistor, a small voltage change at the gate electrode results in a large current variation between source and drain according to the principle of gating amplification. This behavior makes the transistor interesting for biological applications like biosensors.

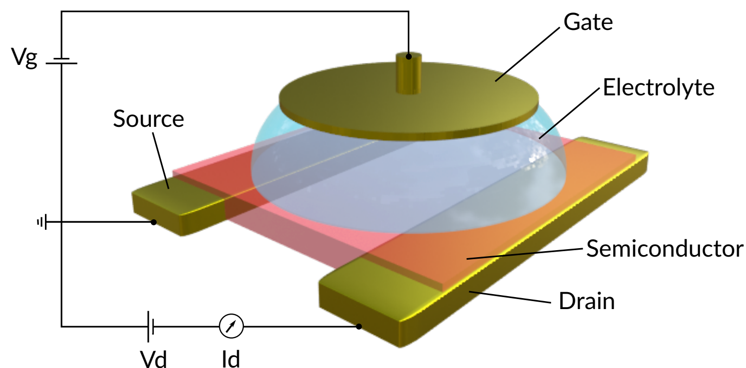

Figure 1.4: Electrolyte-gated organic field-effect transistor (EGOFET) connected via source, drain, and the gate electrode.

The current depends on the channel width to length ratio, so the aspirations often go towards big widths. To fit these big widths on a small surface, the electrodes can be interdigitated, in which source and drain appear alternately in the cross-section while the semiconductor covers the whole area. The gate electrode is not necessarily flat; wires or fibers are also possible (see Figure 1.5).

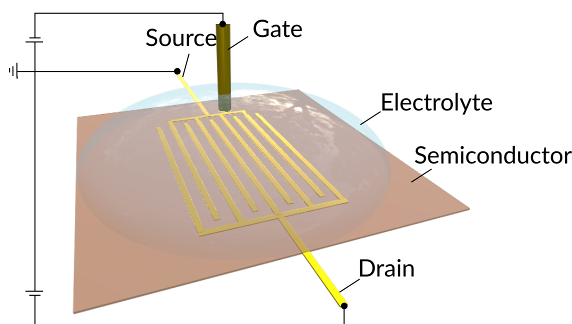

Figure 1.5: EGOFET with interdigitated electrodes.

In a simplistic description, when the voltage at the gate is $V_{GS} = 0\,V$, the ions inside the electrolyte are evenly distributed (see Figure 1.6, a). If a negative voltage at the gate electrode is applied, the positive ions move towards the gate. At the same time, the negative ions accumulate on the opposite side, towards the surface of the semiconductor film (see Figure 1.6, b). The negative charge accumulation at the interface between the semiconductor-electrolyte interface leads to an attraction of the positive charge carriers (holes) towards the interface. With the accumulation of holes, the semiconductor forms a conductive channel, where an electrical current between the source and drain can flow [18]. For a p-type semiconductor, the gate voltage has to be negative to turn the transistor to the on-state; for an n-type semiconductor, a positive gate voltage is required. In general, EGOFETs work in accumulation mode, where the charge carriers accumulate at the semiconductor/electrolyte interface. In contrast, metal-oxide-semiconductor FET (MOSFET), works in inversion mode. To achieve this, the MOSFETs require both types of doped semiconductors (n- and p-doped), whereas organic semiconductors usually work with a single carrier, due to the injection contact. EGOFETs exist in various geometries, where the distance L between the electrodes, the channel width W, and the semiconductor's thickness vary (thin-film semiconductors). Different configurations considering the position of the gate are possible depending on the use case. EGOFETs as biosensors which are top gated [18], side gated [19] floating gated [20] or bottom gated [21] are used, whereas the latter is relatively common. Direct contact with liquid opens possibilities to embed the EGOFET for studies in blood, saliva, tears, sweat, or cells in an aqueous environment. There are several interfacial physical phenomena at the

gate electrode-electrolyte and electrolyte-semiconductor interfaces dictating the modulation the electrical current flowing in an EGOFET, for example

- Interfacial capacitance variations
- fixed charge variations
- electrode work function variations.

How these different mechanisms induce modulations on the current is explained in more detail in what follows.

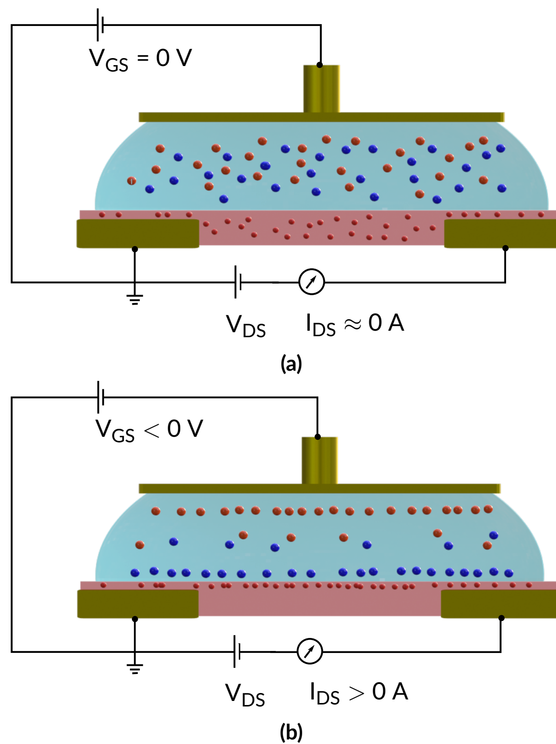

Figure 1.6: Working principle of an EGOFET. (a) When no gate voltage is applied, the ions in the electrolyte (red and blue) and the holes (red) in the semiconductor are evenly distributed. The semiconductor is not conductive, and nearly no current between source and drain is flowing. (b) When a negative gate voltage is applied, the positive ions accumulate at the gate interface. Meanwhile, the negative ions accumulate at the electrolyte/semiconductor interface, which promotes the injection of positive carriers and attracts the positive charge carriers to the semiconductor surface. These form the conductive channel.

1.2.1 Electrical Double Layer

The electrical double layer (EDL) appears when a charged solid is immersed in an electrolyte [22]. In the case of an EGOFET, the double layers are induced at the gate/electrolyte and the electrolyte/semiconductor interfaces. The electrolyte's positive ions are attracted to the negatively charged gate. A well-ordered layer of ions covers the metal-like skin. This layer is the compact layer, also called the Stern layer [23]. The Stern layer does not entirely neutralize the surface charge of the metal, so more positively charged ions are attracted toward the surface. A second layer is formed around the Stern layer, the diffuse ionic layer. As the attraction gets less with increasing distance to the surface, this layer is less ordered.

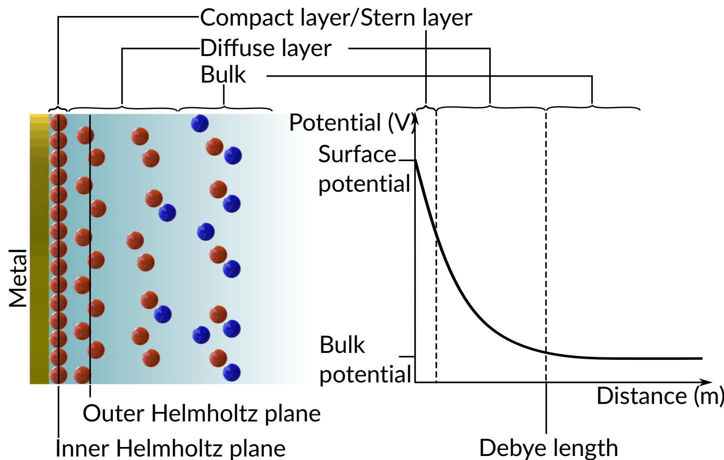

Figure 1.7: The double-layer formation scheme with the corresponding potentials at the surface. The compact layer/Stern layer caused a significant voltage drop. The voltage drop in the diffusive layer bridges toward the bulk potential. The characteristic decay distance of the potential from the surface is the Debye length [22].

In an ideal case, the voltage drop in the Stern layer is linear. The Stern layer is characterized by the Stern capacitance, which, due to its compact nature (thickness below 1 nm), usually takes relatively large values of $10\,\mu F/cm^2$ [24] to $20\,\mu F/cm^2$ [24]. In the diffuse layer, the voltage gradually decreases up to the transition to the bulk potential following an exponential decay (see Figure 1.1). In the Gouy-Chapman model of the EDL, the characteristic distance to the interfacial

layer where the bulk potential is reached is called the Debye length λ_D. It is defined by

$$\lambda_D = \sqrt{\frac{\varepsilon_0 \varepsilon_r k_B T}{n e^2}} \tag{1.1}$$

whereas ε_0 is the vacuum permittivity, ε_r relative permittivity of the electrolyte close to the surface, k_B is the Boltzmann constant, T is the temperature, n is the density of ions, and e is the elementary charge. As seen above, the Debye length depends on the ionic strength of the solution (see Figure 1.8). Usually, the capacitance of the diffusive layer also takes relatively large values of $10\,\mu F/cm^2$ to $20\,\mu F/cm^2$. Due to the double layer's large capacitance of $10\,\mu F/cm^2$ to $20\,\mu F/cm^2$, the EGOFET can be operated with low gate voltages $< 1\,V$ [25, 26].

The Gouy-Chapman-Stern theory predicts the EDL capacitance C_{EDL} to be the same as the equivalent parallel plate capacitor, consisting of the Stern and diffusive layers of thicknesses, $d_{SternLayer}$ and $d_{DiffuseLayer}$, respectively

$$C_{EDL} = \left[\left(\frac{\varepsilon_r \varepsilon_0}{d_{DiffusiveLayer}} \right)^{-1} + \left(\frac{\varepsilon_{r,S} \varepsilon_0}{d_{SternLayer}} \right)^{-1} \right]^{-1} \tag{1.2}$$

with ε_r and ε_S being the corresponding electric permittivities. These capacitance values correspond to zero applied voltages. When a voltage is applied, the accumulation of ions increases and the diffusion capacitance increases exponentially [27].

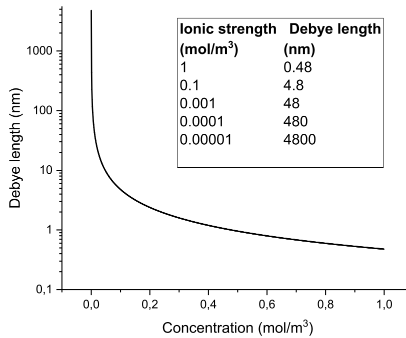

Ionic strength (mol/m³)	Debye length (nm)
1	0.48
0.1	4.8
0.001	48
0.0001	480
0.00001	4800

Figure 1.8: Debye length for different ionic solutions.

1.2.2 Interfacial Capacitances and Fixed Charges

The EDL is not the only interfacial capacitance that can be present in EGOFETs. When using the EGOFET as a biosensor, a functionalization layer is added to the gate or semiconductor surface, whose thickness and fixed charges can vary upon ligand binding. Consequently, the device response is modulated by interfacial capacitances and fixed charges. Additionally, the semiconductor material can have interfacial layers due to phase separations [28]. When a material is immersed in liquid, it is common to have fixed charges, which can be influenced by the ion concentration or the pH of the solution [23, 29–31]. In this case, a capacitor structure is present. A capacitor is an electrical device able to store electrical energy. The capacitance C is given by

$$C = \frac{q}{V} \tag{1.3}$$

where V is the applied voltage, and q is the charge. The capacitance of a parallel plate capacitor (see Figure) depends on the capacitor's geometry with the surface A, the distance d between the plates, the relative permittivity ε_r of the dielectric in-between, and the vacuum permittivity ε_0:

$$C = \varepsilon_0 \varepsilon_\mathrm{r} \frac{A}{d}\,. \tag{1.4}$$

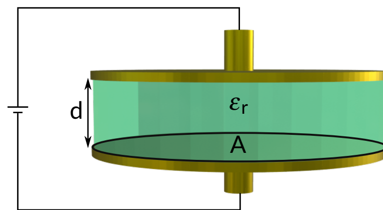

Figure 1.9: Parallel plate capacitor, where A is the surface of the plates with the distance d and a dielectric with the relative permittivity ε_r.

The interfacial layers on the functionalized electrode are defined by their relative permittivity ε_r. In the case of various interfacial layers, like in the case with an antigen and antibody, the capacitances act like individual capacitors C_i connected in series, defined by the equivalent capacitance C_{eq} by

$$\frac{1}{C_{eq}} = \sum_{i=1}^{N} \frac{1}{C_i}\,. \tag{1.5}$$

Additional interfacial layers are also possible at the semiconductor/electrode interfaces. It has been shown that self-assembled monolayers on the source and drain electrode improve the device performance by better aligning the work function of the electrode to the energy levels of the organic semiconductor [32]. The work function describes the needed energy to move an electron outside the material. Organic semiconductors work with an intrinsic charge injection, where the current depends on the contact resistance at the electrode/semiconductor interface [33]. Materials have different work functions, whereas some are more suitable for the device's electrode metal (see Section 1.3).

1.2.3 Current-Voltage Characteristics of an EGOFET

EGOFETs are available in various configurations by different geometries, materials, and electrolytes. The performance of the devices is measured electrically in the current-voltage (I-V) transfer and output characteristics (see Figure 1.10). The transfer curves are obtained by keeping the source-drain voltage constant (V_{DS1},V_{DS2},V_{DSx}) and sweeping the source-gate voltage V_g. The output curves are acquired by keeping the gate voltage (V_{GS1},V_{GS2},V_{GSx}) constant and sweeping the drain voltage V_{DS}.

In region (i) of the transfer I-V curve (see Figure 1.10, a), the transistor is in the off-state. The gate voltage is too low to accumulate enough charges at the interface. Hence there is no conductive channel in the semiconductor. However, the off-state current $I_{DS,off}$ is typically not zero, as there is a low amount of free charge carriers intrinsically in the material. When the gate voltage increases, the conductive channel becomes more populated and conductive as more charges accumulate at the interface—the current increases by increasing gate or drain voltage. The transistor is turned on (ii). From the transfer curve, we can extract an important quantity that defines the modulation efficiency and amplification of the

signal, called transconductance g_{m}, which is defined as the slope of the transfer's on-state curve at the set gate voltage given by

$$g_{\mathrm{m}} = \frac{\Delta I_{\mathrm{d}}}{\Delta V_{\mathrm{g}}} \,. \tag{1.6}$$

The transconductance is a function of both V_{GS} and V_{DS}. The linear regime is independent of V_{GS} (if the transistor behaves ideally). In practice, the maximum transconductance is of interest as an operating region for biosensing purposes.

The output curve (see Figure 1.10, b) is likewise parted in different regions: in (iii) linear regime, the transistor response is proportional to the increase of the drain voltage; in (v) saturation regime, the current saturates; and in (iv) there is wide non-linear transition regime. In the saturation regime, a further increase in the drain voltage does not increase the current; only an increase of the gate voltage gives further changes. In the transfer I-V curves, the saturation region can also be found with the highest $V_{\mathrm{DS}} = V_{\mathrm{DS4}}$, where it becomes independent from V_{DS}. In EGOFET biosensors, the linear regime's operation point is often chosen to get analog signals [34].

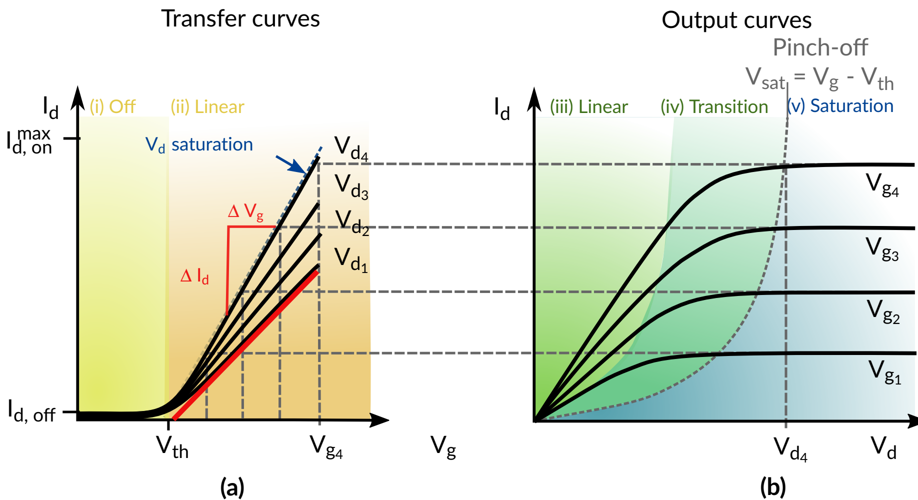

Figure 1.10: Typical transfer and output curve of a FET. The curves are divided into sub-threshold, linear, and saturation regimes.

The device's threshold voltage V_{th} is generally a phenomenological parameter that gives the characteristic gate voltage when the transistor is turned on. It can be extracted as the linear regime's intercept to the horizontal axis (see Figure 1.11, a). There are, however, several methods to extract V_{th}. The method mentioned above is applied in the linear regime, where V_{th} is the tangent's intercept in the maximum slope of the transfer curve. Another method in the linear regime is given by the peak of the second derivative (see Figure 1.11, a). The saturation regime's transfer characteristic has a quadratic dependency. Hence, V_{th} is the tangent's intercept in the maximum slope of the transfer curve's square root (see Figure 1.11, b) [35].

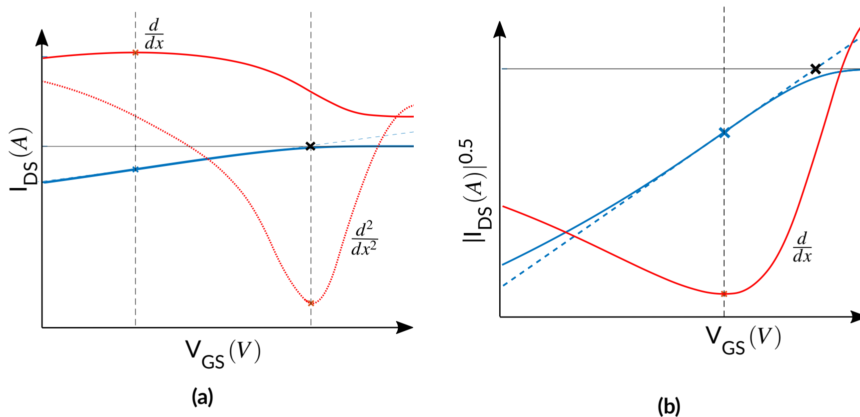

Figure 1.11: Methods to extract the threshold voltage. (a) Methods in the linear regime. V_{th} is the tangent's intercept in the maximum slope of the transfer curve. V_{th} is the position of the peak of the second derivative. (b) A method in the saturation regime. V_{th} is the tangent's intercept in the maximum slope of the transfer curve's square root.

The pinch-off line in Figure 1.11 (b) defines the beginning of the saturation region (vi). Each gate voltage has a corresponding drain voltage where the pinch-off in the conductive channel is happening. The pinch-off points indicate when the conductive channel extends the length between the source and the drain electrode (see Figure 1.12). With a drain voltage lower than the pinch-off point, there is a lack of free charge carriers (holes) close to the drain. However, the electric field between the channel and the drain electrode is high enough for conduction to occur with the few carriers remaining. For sensing devices, this is advantageous, as the current is weakly dependent on the drain voltage and is mainly controlled by the gate voltage.

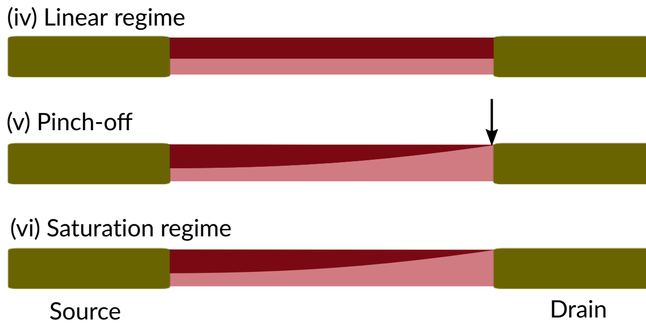

Figure 1.12: Scheme for pinch-off point.

The inorganic transistors model, like metal-oxide-semiconductor field-effect transistor (MOSFET) and thin-film transistors (TFT), is used to describe and fit experimental data mathematically [36, 37]. It describes two regions corresponding to the output curve for a V_{DS} higher or lower than the pinch-off voltage for V_{GS} above the threshold. The current V_{DS} for a p-type semiconductor is described by

$$\mathrm{I_{DS}} = \begin{cases} \mu_p \frac{W}{L} c_{DL} \left[-(V_{GS} - V_{th})V_{DS} + \frac{1}{2} V_{DS}^2 \right], & V_{GS} < V_{th}, V_{GS} - V_{DS} < V_{th}, \\ -\frac{1}{2} \mu_p \frac{W}{L} c_{DL} (V_{GS} - V_{th})^2, & V_{GS} < V_{th}, V_{GS} - V_{DS} > V_{th}, \\ \frac{W}{L} \mu_p c_0 V_{SS}^2 \exp\left(-\frac{V_{GS} - V_{th}}{V_{SS}} \right) \left(\exp\left(\frac{V_{DS}}{V_{SS}} \right) - 1 \right), & V_{GS} > V_{th}, V_{GS} - V_{DS} > V_{th}. \end{cases} \quad (1.7)$$

which contain a number of adjustable phenomenological like the double layer capacitance c_{DL}, the threshold voltage V_{th}, the sub-threshold capacitance c_0, and the sub-threshold sloped voltage V_{SS}. V_{SS} is sometimes expressed in terms of the sub-threshold slope S as $V_{SS} = S/ln(10)$. The relationship between the phenomenological parameters and the physical device parameters is not always clear or established. This fact has introduced ambiguity in interpreting the results and limited reproducibility and predictability. However, in these approximations, the physics of the electrolyte is not described explicitly as it is not needed to explain MOSFET operational principles. Consequently, despite their wide use, these models are insufficient to describe the properties of EGOFETs. In experimental setups, the mobility is often also a phenomenological parameter extracted from the slope of the transfer curve.

1.3 Physics of Organic Semiconductors Devices

The physics of inorganic and organic semiconductors differ considerably. In the following sections, organic and inorganic semiconductors are compared regarding their material behavior, while the charge transport in organic semiconductors is explained.

1.3.1 Inorganic and Organic semiconductors

FETs can be fabricated using inorganic and organic semiconductors [3]. Although inorganic semiconductors offer higher carrier mobility, which means a higher current can easily flow through the semiconducting channel, organic semiconductors have a series of competitive advantages. OFETs can be fabricated using 3D printing techniques under low temperatures. They can occur in low temperatures and even through 3D printing techniques. Using polymer printing to fabricate organic electronics significantly reduces the cost of production. Even more importantly, the flexibility and biocompatibility of the organic devices allow direct interfacing with skin and excitable cells (i.e., brain-electronics interfacing) [38].

Inorganic semiconductors have a crystalline structure, whereas organic semiconductors are disordered solids creating a completely different charge transport scheme that results in different charge carrier mobility. Table 1.1 compares the electrical and mechanical properties of inorganic and organic semiconductors.

Table 1.1: Differences between inorganic and organic semiconductors.

Material	Inorganic	Organic
Charge	Band transport	Hopping
Carrier mobility	$1000\,\mathrm{cm^2/(Vs)}$	$1\,\mathrm{cm^2/(Vs)}$
Mechanical property	Strong and rigid	Weak and flexible

1.3.2 Charge Transport in Organic Semiconductors

A device's electrical current is measured when the charge carriers in the semiconductor move from the source to the drain. The type of the main charge carriers depends on the material: In n-type semiconductors, the conduction is driven by electrons; in p-type material, the main charge carriers are holes. The holes behave similarly to electrons, whereas the direction of the electric field is opposite.

To fully grasp the movement of the charged carriers in semiconductors, we should use the Quantum Mechanical theory, which describes explicitly and predicts the location of electrons in a probabilistic fashion through electronic orbitals. Any electron movement in a sensing unit can be described as an effort of the electron to move in the neighboring atom if the energy barrier allows this hopping. In crystals/solids, the collection of atoms generates an orbital overlap, and consequently, the available energy states appear as a continuous energy band. The energy band filled with electrons is called the conduction band, while the band with no occupying electrons is named the valence band. The bandgap separates the two energy regions and refers to the energy range where no electronic state exists (see Figure 1.14).

As soon as the valence band and the conduction band overlap, the electrons have enough energy states to move, and the material is conductive (i.e. metals). The conductivity of semiconductors lies in between those of insulators and conductors, whereas organic semiconductors are generally less conductive than inorganic semiconductors (see Figure 1.13).

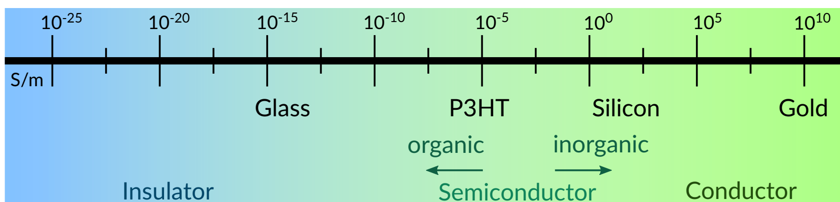

Figure 1.13: Conductivity range of insulators, semiconductors, and conductors. The magnitude of the conductivity at room temperature of the organic semiconductor P3HT [39], the inorganic semiconductor silicon [40], the insulator glass [41], and the conductor gold are shown.

The highest energy level that an electron can occupy in a material at absolute zero temperature is named Fermi level. When the valence and conduction bands lie apart, two different situations can occur. When the Fermi level lies in the bandgap, electrons cannot move from the conduction band to the valence band, and since the electrons cannot be excited to higher energy states, no electron-free carriers are transforming the material into an insulator. In a semiconductor, the Fermi level lies in the bandgap; however, the bands are so close that the highest occupied molecular orbital (HOMO) electrons can move to the lowest unoccupied molecular orbital (LUMO) due to some external low energy excitation. The density of states (DOS) defines the number of available energy states depending on energy. The mobility μ of charge carriers is dependent on the electric field $\vec{E}$ and carriers' velocity:

$$\mu = \frac{v}{\vec{E}}. \tag{1.8}$$

The conductivity σ is the proportionality constant between the current J, and the electric field $\vec{E}$, (Ohm's law) and defines the ability of a material to transport electricity. It depends on the mobility μ, the density of free charge carriers n, and the elemental charge e,

$$J = \sigma E \tag{1.9}$$

where

$$\sigma = ne\mu\,. \tag{1.10}$$

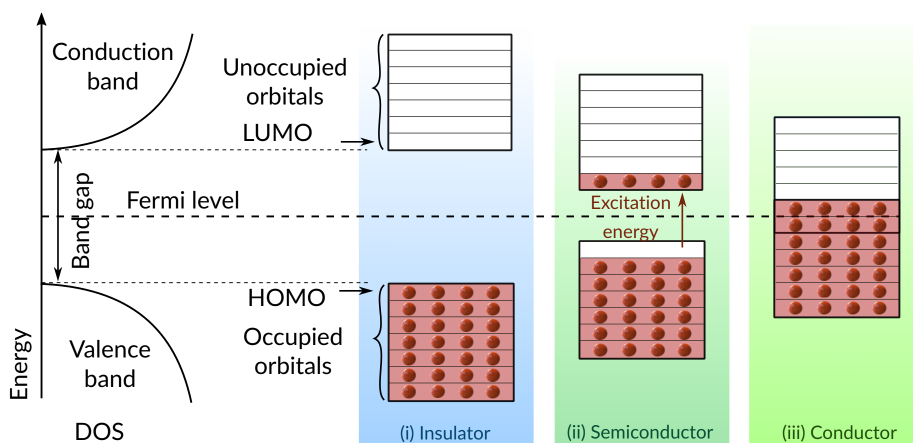

Figure 1.14: The bandgap of an insulator is large, whereas in metals, the conduction band and the valence band overlap. There is essentially no bandgap in metals, making them fully conductive, as electrons can easily move from one band to another. In insulators, the bandgap is large, so the electrons cannot overcome the energy barrier, and there are no free carriers. In semiconductors, the bandgap is small enough to allow for possible excitations of electrons from the highest occupied molecular orbitals (HOMO) to the lowest unoccupied molecular orbitals (LUMO). The density of states (DOS) describes the number of available states at a certain energy level.

1.3.3 The Drift-Diffusion Transport Model for Semiconductor Devices

The physical modeling of semiconductor devices is usually carried out through the drift-diffusion model [42]. In this model, the free carrier transport in the semiconductor is described by the electric potential ϕ and free carrier density (assumed to be holes) p, through the equations

$$\varepsilon_0 \varepsilon_{\mathrm{r,sem}} \nabla^2 \phi = ep\,, \tag{1.11}$$

$$\frac{\partial p}{\partial t} + \nabla \cdot \vec{J}_p = 0\,, \tag{1.12}$$

$$\vec{J}_p = -\mu_p p \nabla \phi - D_p \nabla p\,. \tag{1.13}$$

Here, e is the electron charge, $\vec{J}_p$ the hole number flux density, and D_p is the hole diffusion coefficient, which is assumed to be related to the hole mobility, μ_p, by Einstein's relation for non-degenerate semiconductors, $D_p = \mu_p k_B T/e$, where k_B is Boltzmann's constant and T the temperature. For simplicity, we have assumed the semiconductor is not doped.

1.3.4 Nernst-Plank-Poisson Model

As mentioned in Section 1.2, the commonly used approximations describing the EGOFET's response adapted from MOSFETs and TFTs do not describe the ionic behavior. Hence, it is impossible to investigate the effects of ionic concentration, ultrathin interfacial, or functionalization layers. To cope with this limitation, EGOFET has been modeled by coupling the semiconductor drift-diffusion model to the Nernst-Planck-Poisson (NPP) theory of electrolytes. The Gouy-Chapman theory of the EDL (see Chapter 1.2.1) is equivalent to the NPP framework at equilibrium. In the electrolyte (assumed to be 1:1), the electric potential $\phi(z)$, and ion number densities $n_\pm$ are described using the Nernst-Planck-Poisson model, which is formally identical to the drift-diffusion model for semiconductors, although the underlying transport physics is different:

$$-\varepsilon_0 \varepsilon_{\mathrm{sol}} \nabla^2 \phi = e(n_+ - n_-)\,, \tag{1.14}$$

$$\frac{\partial n_{\pm}}{\partial t} + \nabla \cdot \vec{J}_{\pm} = 0\,, \tag{1.15}$$

$$\vec{J}_{\pm} = \mp \mu_{\pm} n_{\pm} \nabla \phi - D_{\pm} \nabla n_{\pm}\,. \tag{1.16}$$

Here $\vec{J}_{\pm}$ are the ions number transversal flux densities, $\mu_{\pm}$ the ionic mobilities, and $D_{\pm}$ the ionic diffusion coefficients, related through Einstein's relation for diluted ionic solutions $D_{\pm} = \mu_{\pm} k_B T/e$. We assumed the electrolyte to be symmetric, that $\mu_{+} = \mu_{-} = \mu_{ion}$. The initial concentration of both ionic species is assumed to be the same and equal to n_0.

To solve the system of equations in the Helmholtz or NPP frameworks, one needs to define the boundary conditions and the continuity conditions between different materials based on certain assumptions. These assumptions often vary as they determine the complexity of the solution. Often the electrodes are assumed to be an ideal injecting diffusive contact [43]. The substrate can be taken as an insulating boundary condition. For EGOFET models, zero charges and zero flux can be assumed around the model, as well as zero flux between the electrolyte and the semiconductor. This is the difference to OECTs, where ions can penetrate into the semiconductor. However, solving the system numerically with zero flux boundary conditions is challenging due to numerical instabilities when the EDL is developed. In Chapter 2, we will discuss the applied boundary conditions further and give the mathematical description.

1.4 Finite-Element Numerical Modelling

For realistic geometries, the transport equations to describe the physics of semiconductor devices can not be solved analytically, and one has to resort to numerical resolution methods, like the Finite-element numerical method. Finite-element modeling (FEM) is a numerical method to solve differential equations in various engineering fields like electromagnetism, mass transport, heat transfer, fluid flow, and structural analysis. Partial differential equations (PDE) describe a body's behavior. The body is the domain that is discretized in time and space. The continuous domain is subdivided into smaller elements in the meshing process – a finite number of elements (see Figure 1.15). The problem is simplified by solving the equations only at the nodes of these elements. The equations are brought into a larger system of discretized equations and are solved numerically.

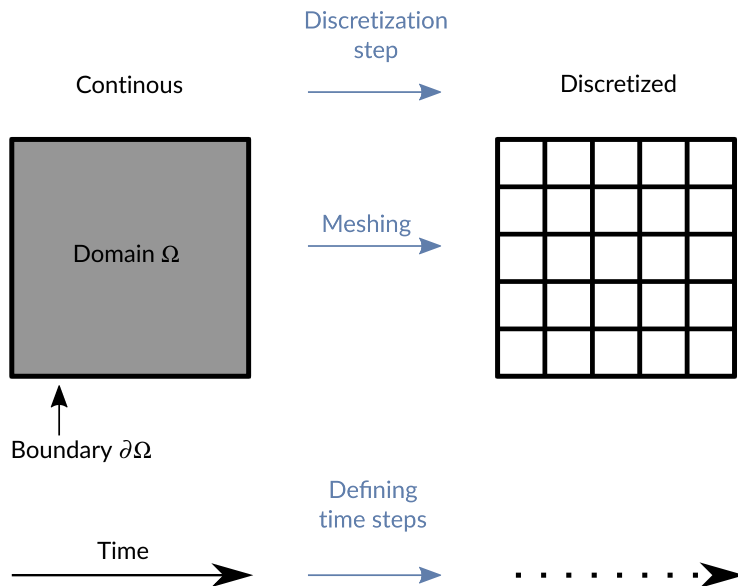

Figure 1.15: Transforming a continuous domain to a finite number of elements in the meshing process. For FEM, spatial and time discretization is required.

1.4.1 Meshing

The meshing process results in the subdivision of the domain. The challenge is to find the optimum between an accurate representation of the geometry and simplifying the problem as much as possible to save calculation time. Meshes are typically not uniformly distributed to capture local effects: in regions of significant changes, more elements are needed to achieve a higher resolution of the problem. The solution does not depend on the mesh when sufficiently fine-grained. Different types of elements are available, depending on the dimension of the model and the geometrical possibilities to define the mesh (see Figure 1.16). Rectangles offer high numerical stability; however, it is often impossible to mesh just with rectangles. Also, a combination of differently shaped elements is possible. The quality of the mesh depends on the element's geometry. More detailed information about mesh generation is found in Okereke and Keates [44].

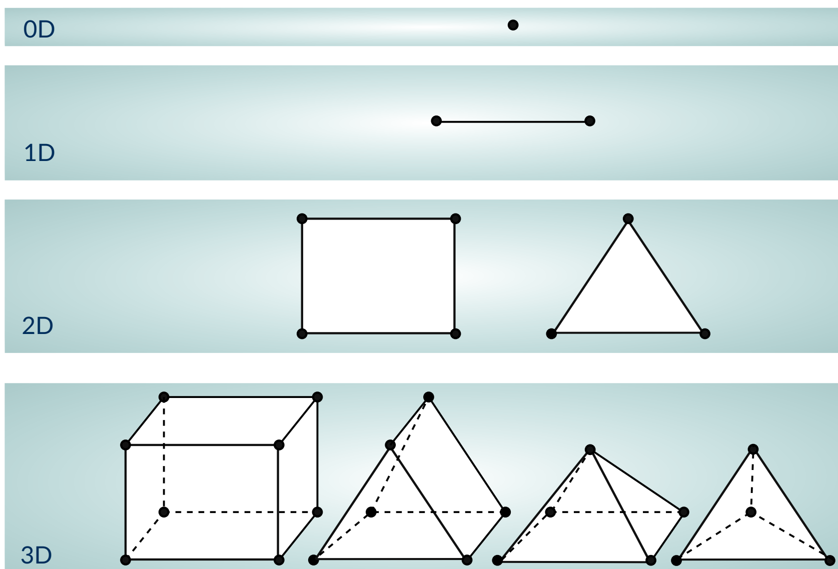

Figure 1.16: Element types for FEM techniques in different dimensions.

1.4.2 Boundary Conditions

The system of equations obtained constitutes a boundary value problem, so the solution is defined by the values defined at the domain's boundaries and the interfaces between different domains (materials). There are different types of Boundary Conditions (BC):

(i) Dirichlet boundary conditions are fixed BCs, which specify the value the equation needs to take at the boundary points. For $u(x) = u$ being the solution of the PDE, the Dirichlet boundary condition $f(x) = f$ on the boundary $\partial\Sigma$ is defined as

$$u = f \quad \text{on} \quad \partial\Omega. \tag{1.17}$$

(ii) Neumann boundary conditions define the value's derivative on the boundary with its normal vector n:

$$\frac{\partial y}{\partial n} = f \quad \text{on} \quad \partial\Omega. \tag{1.18}$$

Mixed BC, Cauchy BC, and Robin BC are combinations of Dirichlet and Neumann BC. Both Dirichlet and Neumann boundary conditions are used to solve the set of equations presented above.

1.4.3 Solving the Equations

Depending on the form of the PDE, different numerical methods are used to solve the system. Initial values are required for each unknown variable as a starting point. The residuum between the actual and the previous step is calculated in every iteration. The solution's approximation is calculated until the residuum is sufficiently small. Convergence towards a solution is achieved.

The equations can be stationary or time-dependent. For time-dependent problems with stationary BC, a quasi-stationary solution can be reached. The time step must be sufficiently small for time-dependent problems in explicit frameworks to follow the physics behavior for achieving convergence.

1.5 State of the Art in Numerical Modeling of EGOFETs

MOSFET and TFT modeling is a broad field [45], which is essential to know precisely the device behavior to have reliable devices when entering the market. However, the MOSFET works without an electrolyte and is an inorganic semiconductor, with its physical description instead of EGOFET characteristics [46]. Due to the complexity of the physical model for EGOFETs, there have been only a few attempts to address it [46–49]. Up to now, there is a lack of a specific EGOFET model, so the MOSFET and TFT models are widely used to fit experimental EGOFET data [36, 37]. Popescu et al. [48] highlight that an analytical solution to the full problem is missing due to the complexity, where the powerful numerical simulation options come into play. Melzer et al. [47] mimicked the EGOFET in the Helmholtz approximation, where the electrolyte is considered just by an equivalent Helmholtz capacitance between the gate electrode and the semiconductor (see Figure 1.17). It mimics the voltage drop across the electrolyte without considering ionic diffusive effects. On the same device, a back gate configuration with an oxide layer was modeled, where they used experimental data to extract the capacitances for different ion concentrations for input data for the simulation. With this approach, the capacitances of thin interfacial layers are considered, as they are included in the experimental measurements. However, this approach requires experimental measurements instead of a standalone simulation approach. To refine the model, Melzer stated that in future investigations, one needs to include the Poisson-Boltzmann description of the electrolyte domain, including the Stern layer.

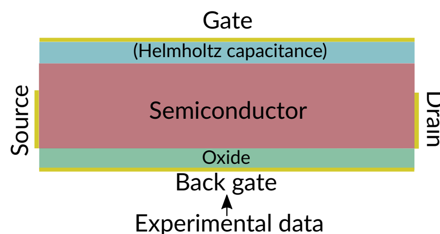

Figure 1.17: Scheme of modeling approach in [47]. The electrolyte is mimicked as a Helmholtz capacitance. The back gate configuration was used to fit the model to experimental data. The model does not represent the migration of ions in the electric field.

Popescu et al. [48] couple two numerical software (MCLite and Centaurus) to solve the electrolyte and the semiconductor, building up on the model mentioned above in the Helmholtz configuration. To achieve a self-consistent coupling, they calculate the potential at the interface in one software and feed it into the other software until the difference drops under a certain tolerance (see Figure 1.18). A back gate configuration with source and drain electrodes on the side was used to fit the system to experimental OFET data. The model includes voltage-dependent mobility and traps and agrees with experimental results for different ion concentrations. The Helmholtz approach is compared with the coupled model, where the electrolyte is mimicked as an equivalent Helmholtz capacitance. It was observed that the Helmholtz approach overestimates the source-drain current. However, the model does not include the interfacial layer at the gate electrode.

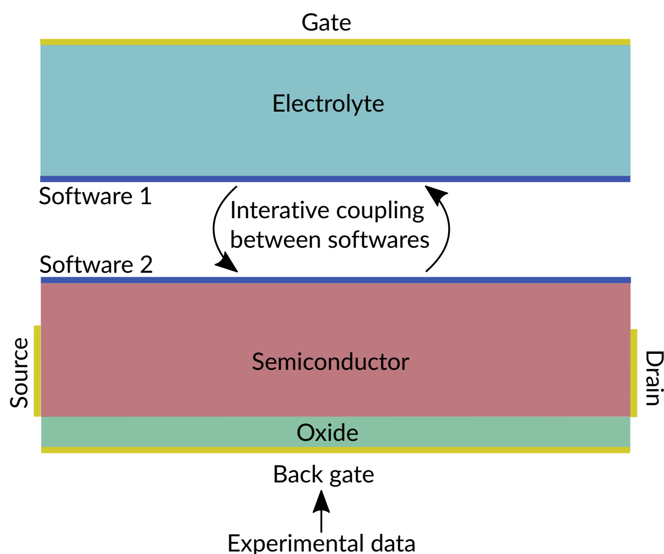

Figure 1.18: Scheme of modeling approach in Popescu et al. [48]. Two software were coupled in a self-consistent way, where the potential at the interface acts as an input parameter for the other software. The model treats only the interfacial layer with the help of experimental data feeding into the system.

Delavari et al. [46, 49] presented two EGOFET setups more completely and compactly than the above models. They used the NPP framework, where the movement of the charge carriers inside the semiconductors is directly coupled to

the ion's migration. To our knowledge, this is the first time an EGOFET model has been presented in this framework realized in a single software. In the first model (see Figure 1.19, a), a gate electrode is on top of the electrolyte, and a source and a drain electrode are on the semiconductor's bottom. This setup is representable for typical geometries of EGOFET devices. This study allowed them to investigate the potential distribution along with the device. The second model (see Figure 1.19, b) used interdigitated electrodes to compare with their experimental setup. The model determines the gate size's role with the electric field's distribution. The device could not be turned on for small gate electrodes as the electric field is low, and the small gate acts as a point source with circular field lines. They achieved a qualitative overlay with experimental data, showing the suitability of the NPP framework. However, the above-mentioned interfacial layers are not present in the model, leading to a mismatch of the physical material parameters while fitting with experimental data. Further, the FEM was performed on a relatively coarse mesh, which might influence the simulated device performance and distributions of charge carriers inside the electric field. To find a physical solution, a time-dependent solver was required. As numerical stability is challenging when directly solving time-dependent, the model was first solved stationary with a constant concentration boundary condition at the electrolyte interface. The solution was then used as an initial condition for the time-dependent solver. Although a stable solution could be achieved with this configuration, the ion concentration varies between the simulations, which might not be accurate in an experimental setup.

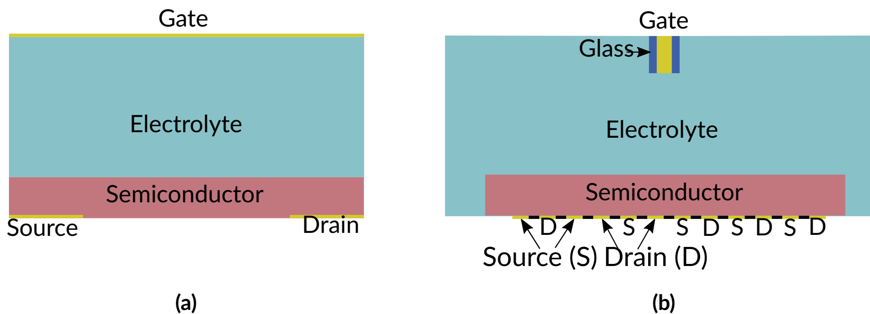

Figure 1.19: (a) Modeling approach in the NPP framework with a gate electrode on top of the electrolyte. Source and drain electrodes are on the button [49]. (b) The model scheme in the NPP framework with interdigitated source and drain electrodes and a top gate variable in size [46]. Both models do not represent interfacial layers.

1.6 Aim of the thesis

Computational models can help identify characteristic parameters and eventually improve and optimize the response and efficiency of a device or an experimental setup. Specifying the model as precisely as necessary to mimic the device response accurately while keeping computational calculation time as short as possible is crucial. Especially while fitting experimental data, fast calculations are needed as often an array of simulations is performed to find the suitable parameters. Using computational models, it is possible to predict the outcome or even replace in vitro experiments quickly, cost-effectively and safely. Precise data fitting allows the extraction and comparison of experimental setups and derivation of characteristic material behavior.

Over the years, some models have been developed to emulate the behavior of EGOFETs based on the Helmholtz approximation, where the effect of ionic contribution is missing. To couple the electrolyte characteristics with the electrical double layer formation, the few available EGOFET models use a Nernst-Planck-Poisson (NPP) framework [46, 48, 49]. These models do not include the ultrathin dielectric layer, which is crucial for the simulation of EGOFET biosensors when overlaying with experimental results.

The main aim of this work is to develop a finite element numerical framework for the modeling of EGOFETs. This enables us to consider realistic device geometries due to the inclusion of the essential physics related to the transport of ions in the electrolyte and the presence of compact interfacial layers. This consideration, in turn, allows us to investigate the physical effects in the device performance and its biosensing applications. To achieve the main objective, we have addressed the following partial objectives:

- To set up a finite element numerical framework to model EGOFETs in 2D in the Helmholtz approximation, in which ionic diffusive effects are neglected. This implementation will be used as a baseline for the complete physical model and a quick analysis of some effects.

- To set up a finite element numerical framework to model metal/electrolyte/ semiconductor capacitor 1D structures in the NPP framework to grasp the

physics associated with ionic diffusive effects and compact interfacial layers.

- To set up a finite element numerical framework to model EGOFETs in 2D in the NPP approximation, in which ionic diffusive and interfacial layer effects are included. This model will calculate the potential and charge distributions in a two-dimensional framework and the device's current-voltage characteristics to gain a complete electrostatic picture of the device.

1.7 Structure of the Thesis

This thesis is organized into seven chapters.

Chapter 1 introduces organic electronics, the fundamental physical equations used to describe the current transport in these systems, finite element numerical modeling, and the current state of the art in the numerical modeling of EGOFETs.

Chapter 2 defines the methods used to implement the numerical frameworks into the finite-element software COMSOL MULTIPHYSICS. It presents the model validation, including mesh independency studies to determine the necessary mesh resolution to mimic the electrical double layer.

Chapter 3 describes the results obtained for EGOFETs in the 2D Helmholtz approximation, where the electrolyte is mimicked as a Helmholtz capacitance. The current-voltage characteristics of the device are correlated to the conductivity changes in the semiconductor film.

Chapter 4 describes the results obtained for the one-dimensional NPP framework's metal/electrolyte/semiconductor capacitor structures. We showcase the role of the ionic concentration and the interfacial layers in the device operation and spot the differences with conventional metal/insulator/semiconductor capacitors.

Chapter 5 describes the results obtained from EGOFETs in the 2D NPP approximations. It provides the potential and the charge carrier concentration distribution of an operating EGOFET. The two-dimensional model helps correlate the macroscopic, measurable device response with processes inside the device. We overlay the simplified model discussed in the previous chapter to validate it with the two-dimensional one.

Chapter 6 discusses the results of this work and compares the outcome with existing models.

Chapter 7 presents the conclusion of the current work and provides a perspective for future work.

1.8 Summary

- EGOFETs are transistors gated by an electrolyte and they offer a strong amplification of the electrical signal.
- EGOFETs can be used as biosensors by functionalizing the gate electrode or the semiconductor.
- Interfacial capacitance induced by the electrical double layer or biorecognition layers modulates the device response.
- The Debye length gives the thickness of the double layer.
- The device response is measured in the current-voltage characteristics, so-called transfer, and output curves.
- EGOFETs are often approximated using the definition of inorganic transistors, which do not consider the formation of the double layer.
- In finite-element modeling, the domain is discretized in space (meshing) and time. The equations describing the system are only solved in the mesh nodes.
- Boundary conditions fix the solution of the equations to the specific problem.
- The Nernst-Planck-Poisson framework describes the movement of ions in the electric field.

PART II

METHODS

Chapter 2

Finite-Element Modeling of EGOFETs

This chapter discusses the implementation we have carried out and the assumptions made for modeling EGOFETs using the finite-element software COMSOL Multiphysics 5.5. We discuss the different levels of implementation: the 2D EGOFET Helmholtz approximation, the 1D NPP capacitor model, and the 2D EGOFET NPP model (see Figure 2.1).

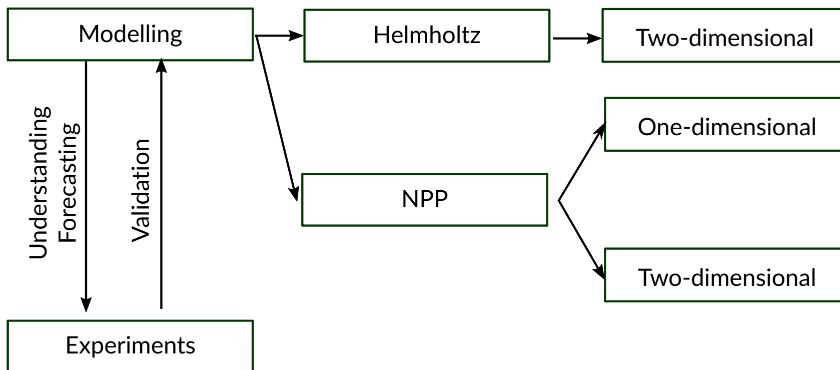

Figure 2.1: Overview of the modeling approach used in this thesis. The EGOFET is modeled in both the Helmholtz and the Nernst-Planck-Poisson (NPP) framework. A one-dimensional capacitor model is also considered.

2.1 Two-dimensional Helmholtz Model

The presence of the metal/electrolyte and semiconductor/electrolyte interfaces makes modeling EGOFETs challenging. These interfaces depend on ionic strength, electrochemical redox reactions, and ionic diffusive space charge layers, whose accurate description may require using atomistic models [50]. Usually, simplified descriptions based on continuum theories are considered, in which the interfaces are described using electrical double layers (EDLs). The simplest of such continuum models is based on the Helmholtz theory of solid/electrolyte interfaces [51], in which EDLs are simply treated as capacitors with a constant specific capacitance c_{H}.

2.1.1 Description of the Model

In the Helmholtz approximation, the electrolyte is substituted by just two Helmholtz capacitances, corresponding to the gate/electrolyte and the semiconductor/electrolyte interfaces, giving an overall equivalent Helmholtz capacitance of $c_{\mathrm{H}} = (c_{\mathrm{H,G}}^{-1} + c_{\mathrm{H,sem}}^{-1})^{-1}$, where $c_{\mathrm{H,G}}$ and $c_{\mathrm{H,sem}}$ are the respective gate and semiconductor/electrolyte Helmholtz capacitances. In this approximation, EGOFETs are equivalent to organic thin-film transistors (OTFT), with c_{H} playing the role of the gate insulator capacitance c_{i}. An essential difference between them is that c_{i} in TFTs is well defined by the properties of the gate dielectric film, while in the case of EGOFETs, the value of c_{H} depends on several phenomena at the electrolyte interface.

The values of c_{H} are usually much higher, in the range of $\mu\mathrm{F/cm}^2$,as compared to those of c_{i}. In EGOFET biosensors [52] c_{H} is one of the parameters that can vary during the sensing process, together with the fixed charges and other parameters. As a result, in EGOFETs, c_{H} is usually treated as a phenomenological parameter.

Here, we implement a numerical model to calculate the current-voltage characteristics of undoped EGOGETs in the Helmholtz approximation operating in the accumulation mode suitable for its simple use in EGOFET biosensor applications. The model continuously covers all the operating regimes (sub-threshold, linear, and saturation) and the more relevant physical device parameters, including those expected to vary during the biosensor response.

Figure 2.2 shows the EGOFET and its model in the Helmholtz approximation. The electrodes are not explicitly inside the modeled domain; they are realized as boundary conditions. Also, the electrolyte is modeled as implicitly as a distributed capacitance boundary condition. The remaining modeled domain is, therefore, the semiconductor domain with the

- insulator boundary condition (black lines),
- source and the drain electrode (yellow lines),
- and the distributed capacitance (blue field).

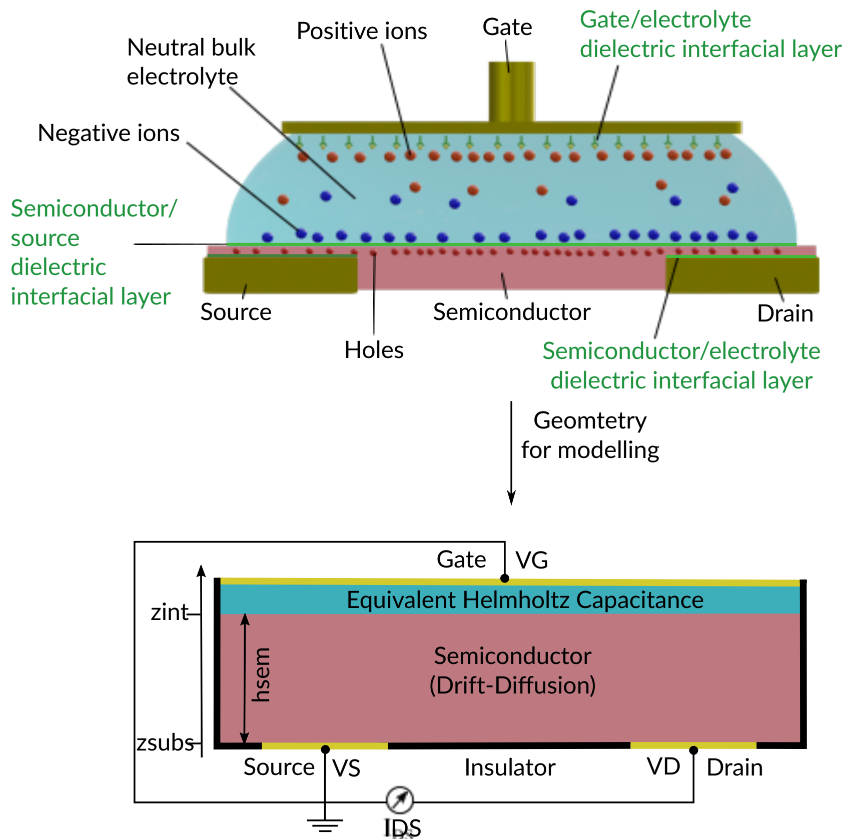

Figure 2.2: Scheme of Helmholtz model with an equivalent Helmholtz capacitance at the gate electrode to mimic the electrolyte of the EGOFET.

The semiconductor transport equations are given in Equations (1.11)-(1.13). These equations must be complemented with appropriate boundary and continuity conditions. At the bottom of the semiconductor film, we assume a fixed hole density boundary condition on top of the source and drain electrodes, corresponding to an ideal injecting diffusive contact [43], and an insulating boundary condition on top of the insulating substrate,

$$p\left(z_{subs}^{+}\right) = p_S\,, \quad \text{Source and Drain,} \tag{2.1}$$

$$\hat{n}\cdot\nabla\varphi\left(z_{subs}^{+}\right) = 0\,, \quad \text{Channel.} \tag{2.2}$$

We neglected non-ideal injection effects at the source and drain electrodes related to interfacial polarization and disorder [53] interfacial states' presence [54]. Within these approximations, p_S can be taken as a constant independent of the applied source-gate voltage. Zero flux boundary conditions are assumed at the gate/electrolyte and semiconductor/electrolyte interfaces as

$$\hat{n}\cdot\vec{J}_p\left(z_{\mathrm{int}}^{-}\right) = 0\,. \tag{2.3}$$

The Helmholtz simplification offers fast results in two dimensions, which help compare with the Nernst-Planck-Poisson model, where we can capture ionic diffusive effects. The following section explains the implementation in the finite element software COMSOL Multiphysics 5.5.

2.1.2 Implementation of the Model in COMSOL Multiphysics

In the Helmholtz simplification, the electrolyte is considered a distributed capacitance, which reduces computational costs. The device is realized with a top gated electrode (see Figure 2.2), with the voltage V_{GS} applied. The source and the drain electrode are flat on the bottom of the semiconductor, realized as boundary conditions with the voltage V_{S} and V_{DS}, whereas the source is grounded. The carrier concentration at the source and drain electrode is set constant. To describe the movements of the holes in the electric field, the COMSOL Multphysics 5.5 modules 'Transport of Diluted Species' and the 'Electrostatics' are coupled.

The electrostatics' boundary conditions (BC) include zero charged sides and underneath the channel given by Equation (2.2), where n is the normal vector to

the surface. The distributed capacitance in BC considers the applied voltage at the electrode in

$$-\hat{n} \cdot \nabla \phi \left(z_{subs}^{+}\right) = \varepsilon_0 \varepsilon_\mathrm{r} \frac{V_\mathrm{ref} - V}{d_\mathrm{s}}, \tag{2.4}$$

where V_ref corresponds to the gate voltage V_G, the source voltage V_S, or the drain voltage V_D. The thickness of the layer is given by d_s with the relative permittivity ε_r of the interfacial layer, here the Helmholtz layer. The boundary condition only depends on the specific capacitance, $c_\mathrm{H} = \varepsilon_0 \varepsilon_\mathrm{r} / d_\mathrm{s}$.

The migration of the holes in the electric field is expressed by the Space Charge Density Coupling' according to Equation (1.11)-(1.13). The mesh is set to rectangular elements, whereas the vertical resolution is higher at the interfaces at $z = z_\mathrm{subs}$, and $z = z_\mathrm{G}$ (see Figure 2.3).

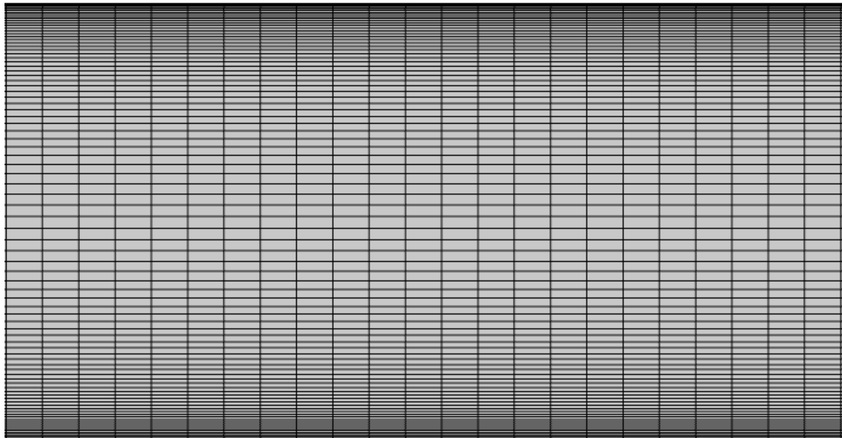

Figure 2.3: Mesh for the Helmholtz model. The interfaces at the domain's top and bottom have a higher resolution. A rectangular mesh discretizes the entire domain.

2.2 Nernst-Planck-Poisson Model

The Nernst-Plank-Poisson (NPP) framework describes the movement, concentration, and balance of charges in an electrolyte. In the semiconductor, the charges are transported by the holes and in the electrolyte by the ions. The advantage of modeling the EGOFET using the NPP theory is the explicit description of the electrolyte ions so that the electrical double layer (EDL) development is explicitly represented. This section describes the implementation of the NPP model for EGOFETs in COMSOL Multiphysics 5.5.

2.2.1 Description of the Model

The NPP model modifies the Helmholtz model described in Section 2.1. In the Helmholtz model, the electrolyte is only presented as a distributed capacitance, so ionic diffusive effects due to the migration of the ions in the electrolyte cannot be captured. By contrast, the NPP framework gives the local ion concentration in the electric field in the electrolyte. The following describes the implementation of the electrolyte replacing the distributed boundary condition of the Helmholtz model.

In contrast to existing EGOFET models [49], we include the presence of ultrathin dielectric layers with and without fixed charges in the model. Interfacial layers are, for example, Stern layers, SAMs, or biorecognition layers. With the same model, we can assume a thicker interfacial layer with charges, corresponding to functionalized interfaces found in EGOFETs used as biosensors [55]. We implemented the model without the interfacial layer at the electrolyte/semiconductor interface. The electrolyte is assumed to be 1:1 symmetric with an equal concentration of positive and negative ions, equal to the initial concentration of ions n_0. The electrolyte is described as a fixed static domain. We first describe the system in two dimensions since a three-dimensional FET can be described with two dimensions, as the third dimension is only the system's depth without any additional degree of freedom. The schematic representation of the two-dimensional NPP model is shown in Figure 2.4.

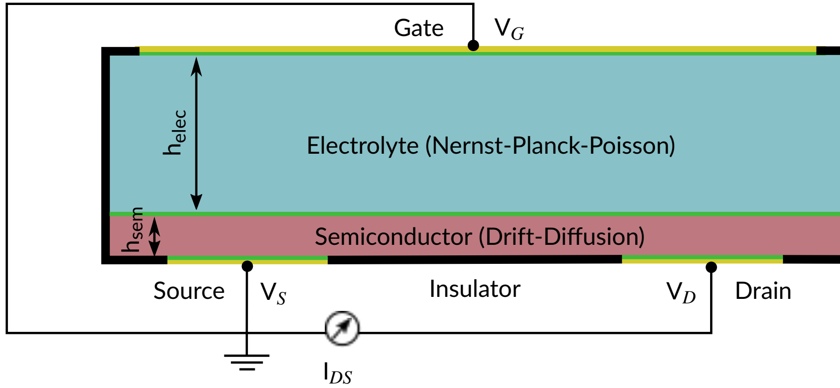

Figure 2.4: EGOFET model with the NPP model in the electrolyte domain and the drift-diffusion descriptions of the holes in the semiconductor domain. The semiconductor with the thickness h_{sem} is connected to the source and drain electrode. The electrolyte with the thickness h_{elec} is connected to the gate electrode.

The two-dimensional NPP model describes the EGOFET with its ionic diffusive effects and the formation of the EDL. However, the simulations are computationally expensive. Several studies with changing parameters are run to investigate the influence of material parameters like hole concentration or ionic concentration. These parameter studies can take days. To overcome this, we have also implemented the model in 1D to gain fast but still reliable results. With the 1D model, we can obtain capacitance, conductivity, and characteristics in less than a minute. This makes the one-dimensional model suitable for investigating the role of interfacial layer, mobility, ion, and hole concentration to define promising experiments and understand the EGOFET in more detail. In addition, we can assess the correct implementation of the numerical model by comparing it with the exact analytical solution for the one-dimensional model obtained in the course of this thesis by my thesis supervisor [56, 57]. This allows us the validation of the numerical implementation of the NPP models. The two-dimensional model is transformed into a one-dimensional model by taking cross-sections in the 2D EGOFET model (see Figure 2.5). Specifically, we define two cross-sections: cutline (I) models the transistor's behavior in the cross-section above the source, while cutline (II) models the behavior in the middle of the channel above the insulator (see Figure 2.5). A cross-section above the drain is equivalent to the cross-section above the source when the source-drain voltage is $V_{\text{DS}} = 0\,\text{V}$. The cutline on the source

corresponds to the behavior of a metal/electrolyte/semiconductor capacitor, which has intrinsic interest and will be studied separately.

We describe the one-dimensional system with the 'Coefficient From partial Differential Equation (PDE)' interface of COMSOL Multiphysics. This module allows for inserting the system of equations while not being bound by predefined options of the modules discussed in Section 2.1.2. Therefore, we could simply insert interfacial capacitances at the electrolyte/semiconductor and gate/semiconductor interfaces and even at the source/semiconductor interface to model a polarizable injecting electrode.

We have also modeled the one-dimensional model in the module-based setup equivalent to the two-dimensional model. We introduced the models with and without the interfacial capacitance at the source electrode for comparison. The interfacial capacitance at the gate electrode (Stern layer) is present in all the models.

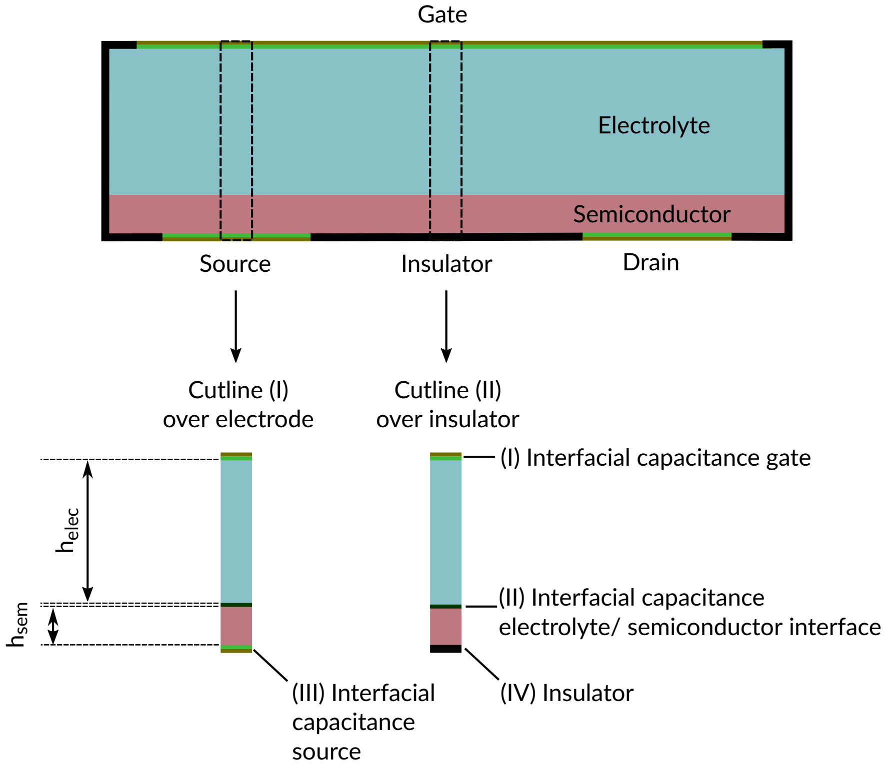

Figure 2.5: The one-dimensional models are obtained by taking cross-sections of the two-dimensional model. Two cutlines are defined to describe the potential and the charge distribution in the EGOFET. Cutline (I) gives the behavior above the electrode, and cutline (II) in the middle of the conductive channel over the insulator.

$$\hat{n} \cdot \vec{J}_{\mathrm{p}}\left(z_{\mathrm{int}}^{-}\right) = 0; \quad \hat{n} \cdot \vec{J}_{\pm}\left(z_{\mathrm{int}}^{+}\right) = 0; \quad \hat{n} \cdot \vec{J}_{\pm}\left(z_{\mathrm{G}}^{-}\right) = 0. \tag{2.5}$$

According to these relationships, no exchange of charges (ions or electrons) occurs at the semiconductor/electrolyte and gate/electrolyte interfaces, implying the lack of faradaic reactions and gate leakage currents. Finally, the boundary conditions set at the gate/electrolyte and semiconductor/electrolyte depend on the assumptions made in the analysis. The boundary conditions can vary in different models. The boundary conditions we present are partly used in previous numerical EGOFET models [46–49]. The difference to these existing models is that the electrolyte is a closed system with a defined ion concentration set to n_0. Further, we include fixed charges and interfacial layers at the interfaces. The

interfacial dielectric layers are described using distributed capacitance boundary and continuity conditions. For the gate electrode, one has

$$\varepsilon_0 \varepsilon_{\mathrm{sol}} \hat{n} \cdot \nabla \phi \left(z_{\mathrm{G}}^{-}\right) = -c_{\mathrm{G}} \left[\phi \left(z_{\mathrm{G}}^{-}\right) - V_{\mathrm{GS}} + \Delta V_{\mathrm{qfix}}\right], \tag{2.6}$$

where,

$$\Delta V_{\mathrm{qfix}} = q_{\mathrm{fix,G}} / c_{\mathrm{G}}, \tag{2.7}$$

$$\varepsilon_0 \varepsilon_{\mathrm{r,sem}} \hat{n} \cdot \nabla \phi \left(z_{\mathrm{int}}^{-}\right) = c_{\mathrm{int}} \left[\phi \left(z_{\mathrm{int}}^{+}\right) - \phi \left(z_{\mathrm{int}}^{-}\right)\right], \tag{2.8}$$

is the voltage shift due to the fixed surface charge at the gate interfacial dielectric layer and V_{GS} the potential of the gate electrode. For the semiconductor/electrolyte interface, one similarly has

$$\varepsilon_{\mathrm{r,sem}} \hat{n} \cdot \nabla \phi \left(z_{\mathrm{int}}^{-}\right) = \varepsilon_{\mathrm{sol}} \hat{n} \cdot \nabla \phi \left(z_{\mathrm{int}}^{+}\right). \tag{2.9}$$

Since the source/semiconductor interface is assumed to be ideal and non-polarizable and since we assumed no difference in the metal work functions of the source and gate electrodes, the source-gate and source-drain voltages are given by $V_{\mathrm{GS}} = V_{\mathrm{G}} - V_{\mathrm{S}}$ and $V_{\mathrm{DS}} = V_{\mathrm{D}} - V_{\mathrm{S}}$. If a work function difference existed, the corresponding shift in the V_{GS} value should be included.

Equations (1.11)-(1.16) subject to the boundary and continuity conditions in Equations (2.1)-(2.6), (2.8)-(2.9) constitute a complete set of equations to determine the electric potential and free carrier concentrations in a 2D undoped EGOFET in the NPP framework, including the presence of ultrathin interfacial dielectric layers, and to calculate the current-voltage characteristics. The fact that the magnitudes can vary along several orders of magnitude in space (from nanometers to tens of micrometers) makes the numerical resolution of the problem particularly challenging.

2.2.2 Implementation of the 1D Model in COMSOL Multiphysics

COMSOL Multiphysics has no straightforward module to include all the physics mentioned above. Instead, COMSOL Multiphysics offers an interface to define the coefficients of a general partial differential equation (PDE) tool. Applied

to the one-dimensional system of cutline (I) over the electrode, the system of equations given in Chapter 1.3.4 with the boundary conditions described above is transformed to

$$d_{\mathrm{a}}\frac{\partial u}{\partial t}+\nabla\cdot c\nabla u+\beta\cdot\nabla u=f\,, \tag{2.10}$$

with

$$u=\begin{pmatrix}\phi_1\\J_+\\n_+\\J_-\\n_-\end{pmatrix},\quad d_{\mathrm{a}}=\begin{pmatrix}0&0&0&0&0\\0&0&1&0&0\\0&0&0&0&0\\0&0&0&0&1\\0&0&0&0&0\end{pmatrix},\quad c=\begin{pmatrix}\varepsilon_0\varepsilon_{\mathrm{r,elec}}&0&0&0&0\\0&0&0&0&0\\0&0&0&0&0\\0&0&0&0&0\\0&0&0&0&0\end{pmatrix},$$

$$\beta=\begin{pmatrix}0&0&0&0&0\\0&1&0&0&0\\-\mu_{\mathrm{elec}}n_+&0&-D_{\mathrm{elec}}&0&0\\0&0&0&1&0\\\mu_{\mathrm{elec}}n_-&0&0&0&-D_{\mathrm{elec}}\end{pmatrix},\quad f=\begin{pmatrix}e(n_+-n_-)\\0\\J_+\\0\\J_-\end{pmatrix}.$$

The semiconductor domain is only solved for the holes as majority charge carriers by the following set of equations

$$u=\begin{pmatrix}\phi_2\\J_{\mathrm{h}}\\n_{\mathrm{h}}\end{pmatrix},\quad d_{\mathrm{a}}=\begin{pmatrix}0&0&0\\0&0&1\\0&0&0\end{pmatrix},\quad c=\begin{pmatrix}\varepsilon_0\varepsilon_{\mathrm{r,sem}}&0&0\\0&0&0\\0&0&0\end{pmatrix},$$

$$\beta=\begin{pmatrix}0&0&0\\0&1&0\\-\mu_{\mathrm{elec}}n_{\mathrm{h}}&0&-D_{\mathrm{sem}}\end{pmatrix},\quad f=\begin{pmatrix}en_{\mathrm{h}}\\0\\J_{\mathrm{h}}\end{pmatrix}.$$

To all interfaces, a no flux boundary condition is applied, which states at interfaces (II), (III) and (IV)

$$J_{\mathrm{h}}=0\,, \tag{2.11}$$

in the semiconductor and at interfaces (I) and (II)

$$J_{\pm}=0\,. \tag{2.12}$$

The potential transition between the two domains is described by

$$\phi_2 = \frac{1}{c_{\text{int}}}\left(-\varepsilon_0\varepsilon_{\text{r,elec}}\frac{\partial\phi_1}{\partial z} + c_{\text{int}}\phi_1\right), \tag{2.13}$$

where c_{int} is the interfacial capacitance (II) between the electrolyte and the semiconductor.

For the case of no interfacial capacitance, the value is set to a high value ($c_{\text{int}} = 10^4\,\text{F/m}^2$) as the capacitance term will tend to zero, and the transition condition will be a continuous potential $\phi_1 \cong \phi_2$.

The interfacial capacitance at the gate electrode is described by

$$\phi_1 = -\frac{1}{c_{\text{G}}}\varepsilon_0\varepsilon_{\text{r,elec}}\frac{\partial\phi_1}{\partial z} + V_{\text{GS}}, \tag{2.14}$$

where c_{G} is the interfacial capacitance and V_{GS} is the applied gate voltage.

Likewise, the interfacial capacitance over the source electrode at cutline (I)

$$\phi_2 = -\frac{1}{c_{\text{S}}}\varepsilon_0\varepsilon_{\text{r,sem}}\frac{\partial\phi_2}{\partial z} + V_{\text{S}}, \tag{2.15}$$

where c_{S} is the interfacial layer at the source electrode and VS the source potential, included here for generality. The cross-section over the drain can be described with the same model, using the drain voltage and the interfacial capacitance of the drain interfacial layer. This model corresponds to an organic metal/electrolyte/capacitor model (OMES).

In the case of cutline (II), the boundary condition underneath the semiconductor mimics an insulator. This describes the transistor's behavior at the cutline in the middle of the channel. The potential is described by

$$\frac{\partial\phi_2}{\partial z} = 0. \tag{2.16}$$

The hole density is fixed by the source, which is outside of the model, and leads to the boundary condition

$$n_{\text{p}} = n_{\text{p}}e^{\frac{-e(\phi_2 - V_{\text{S}})}{k_{\text{B}}T}} \tag{2.17}$$

Besides the coefficient form model, we also realized the 1D model with the modules is equivalent to the two-dimensional model described in Chapter 5. Cutline (I) is the same as the coefficient form model with the difference in the interfacial layer (II). However, the coefficient form modeling provides us more

freedom in implementing the boundary condition, whereas we could add the interfacial layer and the configuration of cutline (II). The one-dimensional module-based model allows an additional direct comparison with the two-dimensional model, apart from the fast calculation time. We will show that the module-based and coefficient form-based for cutline (I) are identical.

The spatial discretization of the one-dimensional model is done similarly to the two-dimensional Helmholtz model. The spatial resolution is more fine-grained at the interfaces, i.e., more nodes are inserted (see Figure 2.6). The mesh does not need to have many nodes in the bulk electrolyte, saving computational time.

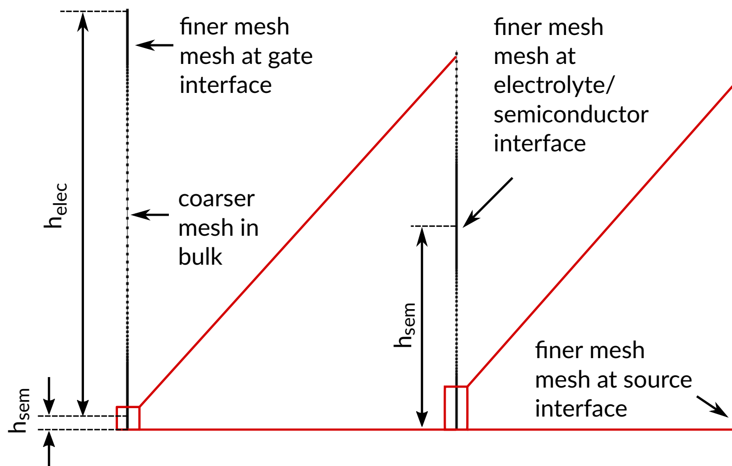

Figure 2.6: One-dimensional mesh with a small element size at the interfaces and a coarser mesh in bulk.

2.2.3 Implementation of the 2D Model in COMSOL Multiphysics

We describe the application of the NPP model for a two-dimensional model of an EGOFET using the finite-element software COMSOL Multiphysics 5.5. An overview of the applied formulas is given. The COMSOL Users Guides provide more information [58**?** , 59]. The model is implemented using the 'Electrostatics' and 'Transport of Diluted Species' modules. The semiconductor

domain's realization is equivalent to the Helmholtz model, described in Section 2.1.2. The difference is the interface to the electrolyte described in this section.

Figure 2.7 shows the simplified geometry of the EGOFET for FEM modeling. Domain (I) describes the electrolyte's potential ϕ and carrier concentration $n_{\pm}$ employing the equation of the NPP framework (see Section 1.3.4 At the same time, domain (II) resolves the semiconductor's potential and hole distribution.

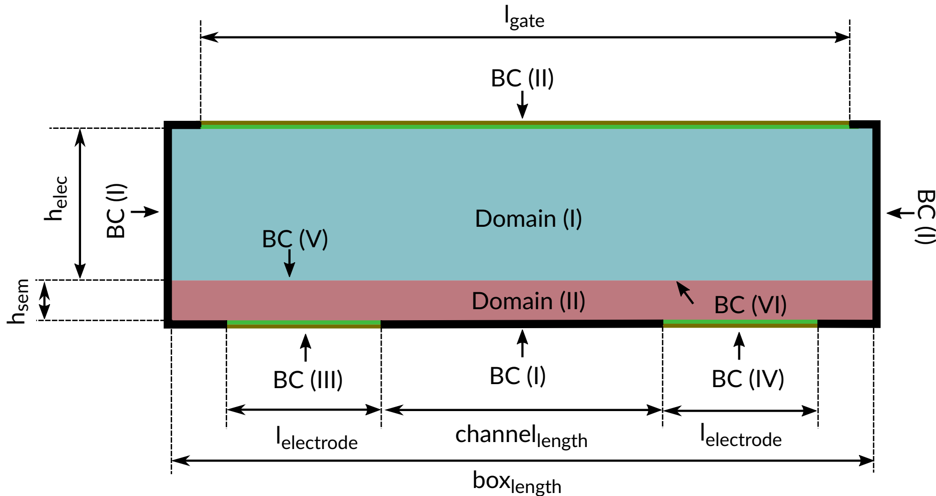

Figure 2.7: 2D FEM model transformation. Domain (I) describes the electrolyte, and domain (II) the semiconductor. The transition between the two domains is constrained by Boundary Conditions (BC) (V) and (VI). Further BCs include zero charged (I) sides and underneath the channel, the gate voltage via a distributed capacitance boundary condition (II), the source voltage via a distributed boundary condition (III), and the drain voltage via a distributed boundary condition (IV).

The electrostatics' boundary conditions (BC) include zero charged sides and underneath the channel, given by Equation (2.2). The distributed capacitance in BC (II, III, IV) considers the applied voltage at the electrode in Equation (2.4). As stated in the NPP framework, the coupling to the holes movement in the domain (II) is expressed by the space charge density coupling in Equations (1.14)-(1.15).

The ion's movement affected by the electric field of the domain (I) is described in the 'Multiphysics' tool with the 'Space Charge Density Coupling' and the 'Potential Coupling', once performed for the ions and the holes, corresponding to their domain. The holes and the ions dynamics are described in the 'Transport

of Diluted Species module'. The 'No Flux' BC condition is applied to BC (I), (II), (V), and (VI). The initial concentration of the ions is set at the start and is maintained due to the no flux boundary conditions around domain (I). In domain (II), we set the initial hole concentration at the same value as the constant concentration BC at the boundary (III) and (IV). The holes can therefore move in and out. Table 2.1 summarizes the BC inside the modules.

Table 2.1: Overview of domain and boundary conditions (BC) in their corresponding modules.

	Electrostatics Module	**Transport of Diluted Species Module**
Domain (I)	Potential Coupling Charge conservation	Space charge density coupling of ions
Domain (II)	Potential Coupling Charge conservation	Space charge density coupling of holes
BC (I)	Zero charge	No flux
BC (II)	Distributed capacitance with gate voltage	No flux
BC (III)	Distributed capacitance with source voltage	Constant concentration
BC (IV)	Distributed capacitance with drain voltage	Constant concentration
BC (V)	Continuous voltage	No flux
BC (VI)	Continuous voltage	No flux

The EGOFET was discretized with a rectangular mesh equivalent to the Helmholtz model. The electrolyte on the top and the bottom has a higher resolution to solve the EDLs. We achieved a resolution of $< 0.1\,\mathrm{nm}$ at the interfaces at $z = \{0\,\mathrm{nm}, h_{\mathrm{sem}}, h_{\mathrm{sem}} + h_{\mathrm{elec}}\}$.

2.3 Solver and Time-Step Adjustment

COMSOL Multiphysics 5.5 provides different solvers and time-stepping methods. Default settings are given in the COMSOL user guides. Here we want to highlight the adjusted settings. To better understand the methods and the given default settings, we refer to the COMSOL user guide [60].

All the models are solved with the backward differentiation formula (BDF) operators automatically adjusted the time step, which showed good stability. The models are solved with the parallel direct sparse solver (PARDISO) solver for memory-efficient, high-performance, and robust system solving [61]. Due to the highly non-linear character of the equations, PARDISO was found to be the most robust available solver in COMSOL Multiphysics 5.5 to reach convergence.

The one-dimensional NPP model is calculated with the time-dependent solver for 10 s for each V_{GS} with $V_{DS} = 0\,\mathrm{V}$. The last solution is taken as the stationary solution, as the EDL is fully envolved for $t \ll 10\,\mathrm{s}$ calculation time. In the two-dimensional NPP model, we observed numerical instabilities with this method, as in this model, a drain voltage is applied as well. Therefore, for each drain voltage, the gate voltage is time-dependent from positive to negative voltages, giving the EDL time to envolve in each case (see Figure 2.8). This gives us the possibility to calculate with no flux boundary conditions with a time-dependent solver in contrast to the model presented in [46]. The Helmholtz model is calculated with the same method.

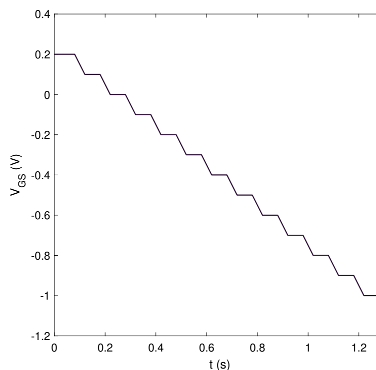

Figure 2.8: Time-dependent signal at the gate or drain electrode. The signal is changed for the voltage of interest and kept constant for several time steps to ensure a static condition for each voltage.

2.4 Model Validation and Verification

The computational Helmholtz and NPP models have been validated and verified. Validation evaluates the extent to which the model presents the reality, whereas verification identifies computational and numerical errors. In this section, we verify the models toward the analytical solutions we developed that are valid in some restricted conditions [56, 57, 62] and analyze the spatial discretization (mesh). The solution of the model must be independent of the mesh. However, if the mesh resolution is not high enough, the physics cannot be mimicked correctly. Moreover, the shape and distributions of the elements might influence the error. Below, we present simulations calculated on different meshes.

2.4.1 Verification of the 2D Helmholtz Model Implementation

In implementing the 2D Helmholtz model, we used a built-in implementation in COMSOL Multiphysics. This fact makes that much less effort must be devoted to verifying the model. Here, the main effort was devoted to finding the appropriate meshing conditions to obtain relatively fast results while maintaining accuracy.

We performed a mesh independency study on a mesh with 10 µm channel length (see Table 2.2). We evaluated the transfer curve as the criteria to determine mesh independency, as the macroscale current combines the nanoscale device physics. Between mesh 1 and 2 we observed a significant difference in the transfer curve. However, further spatial refinement did not give a significant difference in the voltage range of $V_{\text{GS}} = [0.1, -0.6]$ V. We found that refinement in the horizontal direction gives no significant difference, nor the absolute number.

Table 2.2: Spatial resolution for different meshes of the Helmholtz model.

Mesh	Elements	Max. mesh size interface	Max. element size
1	87	8	2.5 nm
2	87	100	2 nm
3	174	200	1 nm
4	87	1000	0.5 nm
5	348	16	2 nm

The most influence has the vertical resolution of the elements close to the interfaces, hence the ratio of the elements from the biggest to smallest in the vertical direction. With channel lengths $< 10\,\mu m$, there is no significant difference with higher ratios than 100 (see Figure 2.9). However, in longer channels, there is. The final selected mesh for the long channel has a resolution of 2.2 pm at the top and the bottom of the domain (87 elements with a ratio of 1000).

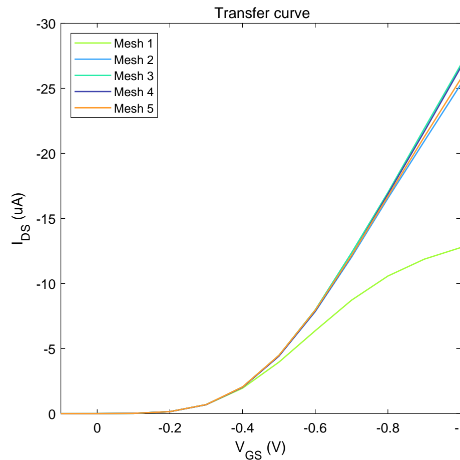

Figure 2.9: Helmholtz model, calculated with different spacial resolution. Parameters of the calculation: $p_s = 6 \times 10^{15}\,\mathrm{cm}^{-3}, \varepsilon_{r,sem} = 4, h_{sem} = 30\,\mathrm{nm}, c_G = 0.1\,\mathrm{F/m}^2, T = 293.15\,\mathrm{K}, L = 10\,\mu\mathrm{m}, W/L = 500, l_{electrode} = 1\,\mu\mathrm{m}, V_{DS} = -0.4\,\mathrm{V}$

To verify the results, we have considered a one-dimensional analytical solution to the model along the transversal direction [56] valid in the long channel limit for $V_{DS} = 0\,\mathrm{V}$ and a channel length of $60\,\mu m$ (see Figure 2.10).

The solid continuous lines correspond to the 1D transversal analytical solution derived in [62]. The predictions of the one-dimensional analytical model follow those of the two-dimensional model, thus validating the assumptions made in its derivation. The analytical solution is valid for the long channel limit, whereas the numerical is used later on for models with shorter channel lengths. For longer channels, it was found that the resolution at the interface has to be even finer than for shorter channels to not accumulate computational errors over the long channel.

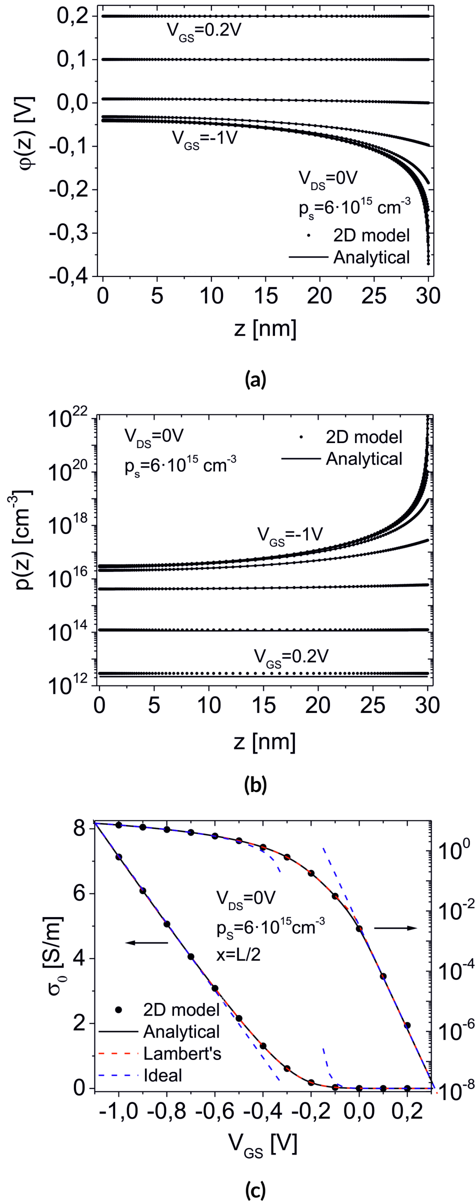

Figure 2.10: (a) Electric potential and (b) hole concentration distributions across the transversal direction of the semiconductor film in the mid point of the channel ($x = L/2$), for different values of the source-gate potential V_{GS} and zero source-drain voltage, $V_{DS} = 0\,\mathrm{V}$. The symbols correspond to the two-dimensional model numerically solved, while the solid lines to the one-dimensional model are analytically solved. (c) Sheet semiconductor conductivity for $V_{DS} = 0\,\mathrm{V}$, in the mid point of the channel ($x = L/2$) as a function of the source-gate voltage V_{GS}. A detailed description of the analytical solution is given in [62]. Parameters used in the calculations: $p = 6 \times 10^{15}\,\mathrm{cm}^{-3}, \varepsilon_{\mathrm{r,sem}} = 4, h_{\mathrm{sem}} = 30\,\mathrm{nm}, c_{\mathrm{H}} = 1\,\mu\mathrm{F/cm}^2, q_{\mathrm{fix}} = 0\,\mathrm{C/m}^2, L = 60\,\mu\mathrm{m}, L_S = L_D = 1\,\mu\mathrm{m}, T = 293.15\,\mathrm{K}$. Figures taken from Huetter et al. [62]

.

2.4.2 Verification of the 1D NPP Model Implementation

We created the one-dimensional NPP model with the built-in modules 'Electrostatics' and 'Transport of Diluted Species' of COMSOL Multiphysics and the coefficient form of the 'Mathematics' module. The coefficient form gives more freedom in applying the boundary conditions. However, the module-based form is the same setup as the one we used in the two-dimensional model implementation, allowing a direct comparison between them. We performed several studies to find a mesh resolution that is fine enough to provide a mesh-independent solution.

We performed a mesh independence study, where the interface's mesh size was gradually refined. We compared the module-based one-dimensional model to the two-dimensional model in the mesh independence study. The calculation time in the one-dimensional case is, on average equal to 10 minutes, without any significant deviations. We calculated the error of the potential distribution with respect to the one corresponding to the mesh with the highest resolution. We calculated the relative global error by

$$Error_{\mathrm{Mesh,x}} = \frac{\int (\phi_{\mathrm{Mesh,x}} - \phi_{\mathrm{Mesh,7}})\,\mathrm{d}z}{\int \phi_{\mathrm{Mesh,7}}\,\mathrm{d}z} \cdot 100\,, \tag{2.18}$$

The mesh was gradually refined at the interfaces. For a resolution where the element's thickness at the interface is $< 0.1\,\mathrm{nm}$, the error is under 3%.

In Figure 2.11, we compared the error of the solution for different mesh sizes. We gradually refined the mesh from 2 nm mesh size to 0.5 pm and calculated the error to the highest resolved mesh for different gate voltages. The error for positive voltages, where the device would be in off-state, is around zero, as the device response remains zero for all the meshes. When the device is in the on-state, the error between the meshes is higher when the voltage is higher. The same behavior is observed in the voltage drop at the interface to the gate at $z = 1030\,\mathrm{nm}$ (see Figure 2.12).

The error does not decrease significantly for an element size of less than 0.1 nm. However, the number of elements increases exponentially (see Figure 2.11, red line). Also, in the conductivity curves (see Figure 2.12), which we will analyze and explain later in detail, we can see that the curves overlay for a mesh size less than 0.1 nm. Therefore an element size of 0.1 nm at the interface was chosen.

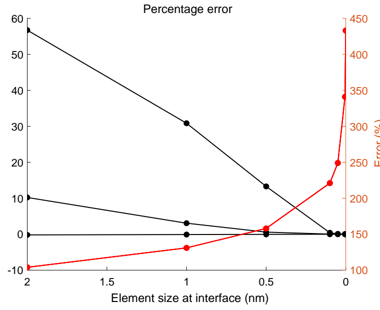

Figure 2.11: The error for different mesh resolutions for the one-dimensional model. The size of the first element at the interfaces was gradually reduced with values of 2 nm, 1 nm, 0.5 nm, 0.1 nm, 0.05 nm, 0.005 nm, and 0.0005 nm. For an element size smaller than 0.1 nm, the error was under 3%. Parameters used in the calculations: $n_\mathrm{h} = 6 \times 10^{15}\,\mathrm{cm}^{-3}, \varepsilon_{\mathrm{r,sem}} = 4, h_\mathrm{sem} = 30\,\mathrm{nm}, h_\mathrm{elec} = 170\,\mathrm{nm}, c_\mathrm{G} = 0.0243\,\mu\mathrm{F/cm}^2, c_\mathrm{S} = c_\mathrm{int} 1E4 \mu\mathrm{F/cm}^2, T = 293.15\,\mathrm{K}$. Figure taken from [62].

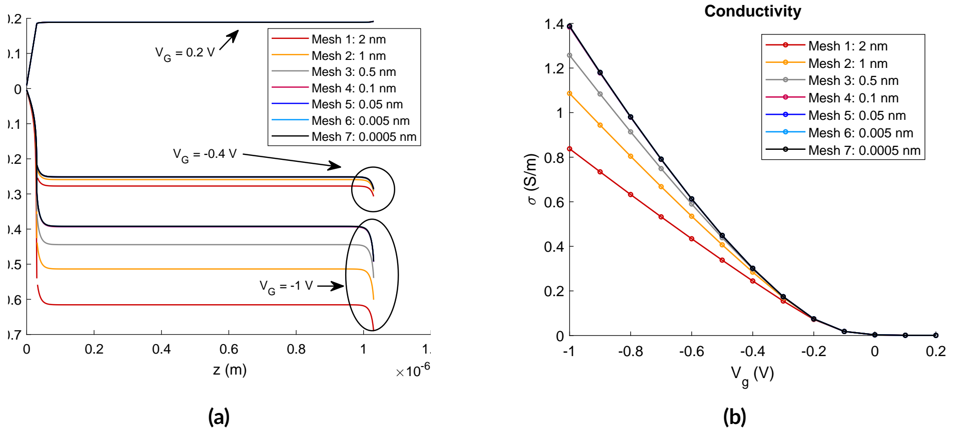

Figure 2.12: (a) Voltage distribution and (b) conductivity for 7 different mesh sizes at $V_\mathrm{G} = [0.2, -0.4, -1]$ V. The difference between the meshes increases with the voltage. Mesh 4, 5, 6, and 7 overlays in all the graphs. Parameters used in the calculations: $n_\mathrm{h} = 6 \times 10^{15}\,\mathrm{cm}^{-3}$, $\varepsilon_{\mathrm{r,sem}} = 4$, $h_\mathrm{sem} = 30\,\mathrm{nm}$, $h_\mathrm{elec} = 170\,\mathrm{nm}$, $c_\mathrm{G} = 0.0243\,\mu\mathrm{F/cm}^2$, $c_\mathrm{S} = c_\mathrm{int} = 1 \times 10^4\,\mu\mathrm{F/cm}^2$, $T = 293.15\,\mathrm{K}$.

In the course of the thesis, an exact analytical solution (up to a quadrature) of the 1D NPP model has been found [56]. We have used this solution to benchmark

the implementation of the one-dimensional model. We have implemented three one-dimensional numerical models for the cross-section (I) (see Figure 2.5):

(i) Module-based with the interfacial capacitance at the gate c_G and no interfacial capacitances at the source c_S and semiconductor interface c_{int}.

(ii) Module-based with an interfacial capacitances at the gate and source c_G and c_S at the source, but no interfacial capacitance at the semiconductor interface c_{int}.

(iii) Coefficient-based with all interfacial capacitances present, source c_S gate c_G and semiconductor interface c_{int}.

The validation has been performed with the more general model (iii), and then using it to validate the other two models, which are recovered by setting respectively, (i) c_S and $c_{int} \ll 1$, and (ii) $c_{int} \gg 1$. Here, $c \gg 1$ means for instance, $1 \times 10^4\,\mathrm{F/m^2}$, so the effects of this interfacial layer become negligible. The characteristics of the model (iii) for c_{int} or/and $c_S > 1 \times 10^4\,\mathrm{F/m^2}$ overlap the predictions of models (i) and (ii), thus validating them.

Figure 2.13 (a) and (c) show the electric potential and charge density distributions across the one-dimensional EGOFET in the source region. The blue, red, and green lines refer to semiconductors, electrolytes, and compact interfacial layers. The insets in Figure 2.13 (c) and (d) show the charge density distribution in the semiconductor film. The symbols represent the results of the finite element numerical calculations. The agreement with the analytical solution is perfect as it corresponds to an exact solution to the problem [57], thus validating the numerical implementation.

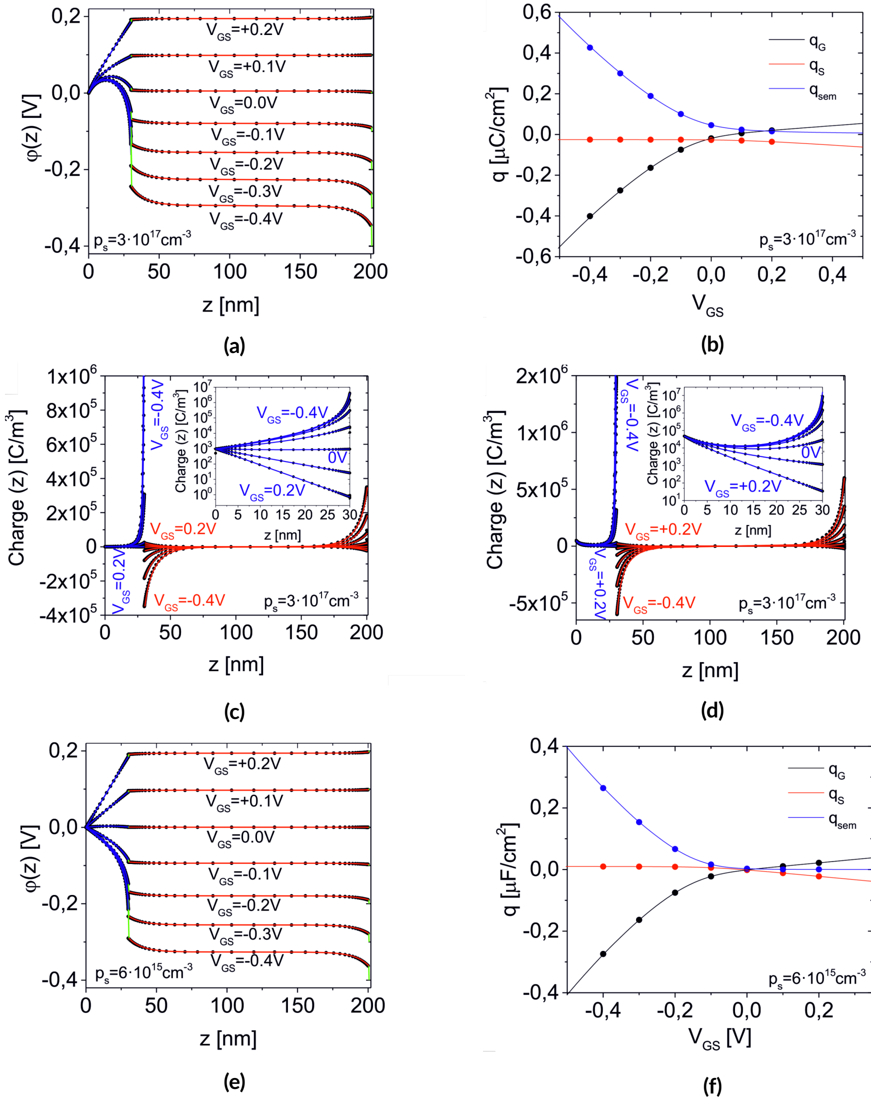

Figure 2.13: (a), (c) and (e) Electric potential, charge densities and accumulated charges in an OMES capacitor for $p_s = 6\times10^{17}\,\mathrm{cm^{-3}}$, $\varepsilon_{r,sem} = 4$, $\varepsilon_{r,elec} = 4$, $h_{sem} = 30\,\mathrm{nm}$, $h_{elec} = 170\,\mathrm{nm}$, $c_G = 7.3\,\mu\mathrm{F/cm^2}$, $c_{int} = 3.65\mu\mathrm{F/cm^2}$, $T = 293.15\,\mathrm{K}$, and $q_{int} = 0\,\mathrm{C/m^2}$ for different source gate voltages. The continuous lines correspond to the analytical solution [60]. The blue, green and red colors correspond to the semiconductor, interfacial dielectric layers and electrolyte regions, respectively. The symbols correspond to the numerical resolution of the model. Inset in (c): charge density in the semiconductor in a linear-log representation. (b), (e) and (f) same, but for $p_s = 6\times10^{15}\,\mathrm{cm^{-3}}$. For the parameters used in the calculations one has: $L_D = 9.6\,\mathrm{nm}$, $c_{sol} = 7.2\,\mu\mathrm{F/cm}$, $c_{int,eq} = 2.43\,\mu\mathrm{F/cm^2}$, $c_{stray} = 0.12\,\mu\mathrm{F/cm^2}$, $L_{Ds} = 3.0\,\mathrm{nm}$ and $c_{sem} = 1.15\,\mu\mathrm{F/cm^2}$ for $p_S = 3\times10^{17}\,\mathrm{cm^{-3}}$ ($L_{Ds} = 21.8\,\mathrm{nm}$, $c_{sem} = 0.16\,\mu\mathrm{F/cm^2}$ for $p_S = 6\times10^{15}\,\mathrm{cm^{-3}}$). Figures taken from Huetter et al. [57].

2.4.3 Verification of the 2D NPP Model Implementation

We performed different simulations with different meshes compromising rectangular or triangular elements. Table 2.3 gives an overview of the configurations. First, we conducted four simulations with triangular elements, where we gradually refined the mesh size at the interfaces. Mesh 4 is the direct refinement of mesh 2. A further refinement of the mesh calculation was not possible due to limited memory. The rectangular mesh has a higher resolution at the interfaces and gradually increases the thickness of the elements towards the middle of the bulk (z-direction). Mesh 5, 6, and 7 have the same distribution in the z-direction but are refined in the x-direction. Mesh 9 has the same distribution in the z-direction as the one-dimensional model for maximum element size at the interface of 0.1 nm. We have also tried to include rectangular boundary layers followed by triangular elements. This gives the possibility of a high-resolution mesh at the interface and a coarse mesh in the bulk of the electrolyte or semiconductor. However, with this configuration, the convergence of the solution was not achieved. Eventually, we compare the results obtained on triangular and quadratic meshes.

The minimum element quality is measured by the condition number, which is a commonly used number to evaluate the mesh quality. The calculation time of an Intel®Core™ i7-7700K CPU with 4.2 GHz bandwidth with four Cores, eight logical processors, and 64 GB memory is given. We, also, present the error towards the one-dimensional model, which was validated against the analytical solution before. This was the resolution where we observed mesh convergence with less than 3% error.

Mesh	Number elements	Max. mesh size int.	Form	Condition nb.	$t_{calculation}$	Error
1	671 078	1 nm	triangular	0.78	> 1 h	21 %
2	1 471 412	0.5 nm	triangular	0.74	> 7 h	9 %
3	2 018 203	0.38 nm	triangular	0.72	> 5 h	7 %
4	5 885 648	0.25 nm	triangular	0.74	> 25 h	4 %
5	108 288	0.214 x 8 nm	rectangular	1	> 30 min	14 %
6	216 000	0.429 x 4 nm	rectangular	1	> 2 h	14 %
7	432 000	0.429 x 2 nm	rectangular	1	> 4 h	13 %
8	552 000	0.095 x 2.5 nm	rectangular	1	> 6 h	6 %
9	739 200	0.103 x 2.5 nm	rectangular	1	> 9 h	3 %

Table 2.3: Comparison between different types of meshes, including maximum sizes, element type, and mesh quality. As result, the error of the potential distribution over the source electrode is calculated. Appendix A shows the corresponding meshes. The calculation time refers to calculating one transfer curve from $V_{GS} = [0.1, -1]$ V. Parameters of the calculation: $n_h = 6 \times 10^{15}\,cm^{-3}, \varepsilon_{r,sem} = 4, \varepsilon_{r,elec} = 4, h_{sem} = 30\,nm, h_{elec} = 1000\,nm, c_G = 0.0243\,uF/cm^2, c_S = c_{int} = 1 \times 10^4\,uF/cm^2, T = 293.15\,K$..

The simplified rectangular geometry of the EGOFET allows for using a straightforward rectangular mesh with perpendicular element walls. Triangular meshes are used when complex geometries must be discretized. Moreover, triangular meshes enable coarser elements to be in bulk without a high skewness of the elements, leading to poor mesh quality. The model was calculated with the time-dependent solver for 10 s at each voltage. The solution at $t = 10\,s$ was taken as the static solution.

As in the case of the 2D Helmholtz model, we use the fact that for long channel lengths, the one-dimensional solution of the NPP model along the transversal direction is also the solution of the two-dimensional NPP model for $V_{DS} = 0\,V$ to a good approximation (see Figure 2.14). The one-dimensional model has been found numerically and analytically [56].

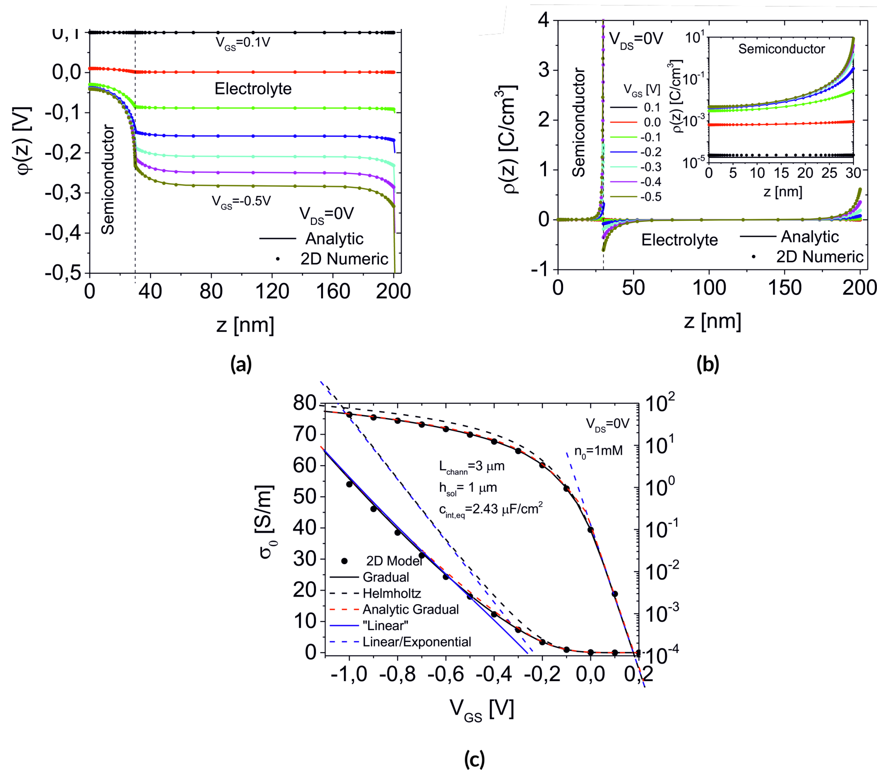

Figure 2.14: Electric potential and (b) charge carrier density distributions across the transversal direction of the EGOFET channel for $V_{\mathrm{DS}} = 0\,\mathrm{V}$ for different source gate voltages $-0.5\,\mathrm{V} < V_{\mathrm{GS}} < 0.1\,\mathrm{V}$. The symbols represent the results of the two-dimensional numerical model, and the continuous lines correspond to the analytical one-dimensional solution The sharp lines at the edge represents the voltage drop at the interfacial layer. Inset in (b): charge carrier density in the semiconductor in linear-log representation. (c) Sheet semiconductor conductivity σ for $V_{\mathrm{DS}} = 0\,\mathrm{V}$ as a function of V_{GS} as obtained from the two-dimensional NPP numerical model (symbol) and the analytical NPP gradual channel approximation model (continuous black lines). The black dashed lines correspond to the predictions of the Helmholtz approximation, which neglect ionic diffusive effects. The blue continuous and dashed lines correspond to the "linear" approximations for the NPP and Helmholtz models, respectively. Figure is taken from Huetter et al. [56].

We compared the zero voltage conductivity curves of the one-dimensional solution with those of the 2D solution. An error of less than 5% is observed for the finest triangular mesh, whereas the error was less than < 3% for the finest rectangular. The rectangular mesh is double as fast as the triangular mesh while providing better accuracy. Therefore, Mesh 9 was selected for the calculations in

the subsequent chapters. In Figure 2.15, we present the error concerning the 1D model calculations for different meshes against the applied potential at the gate. On average, for the finest triangular and rectangular meshes, we observe an error of less than 5% and 3% compared to the analytical solution. To shorten the simulation time and acquire good quantitative agreement with the analytical solution, we selected mesh 9 for our subsequent calculations in the next sections of this work for a channel length of $< 3\,\mu\text{m}$ in the interval of $V_{\text{GS}} = [0.2, -0.7]$ V. For longer channels or higher voltages, we selected the same number of elements. However, we increased the ratio of the elements to achieve a higher resolution at the interface. When we introduced an additional interfacial layer at the semiconductor/electrolyte interface, the resolution is required to be higher. Therefore, we calculated these models with 87 elements in the semiconductor with a ratio of 1000 from the smallest to biggest model. These mesh independency studies enabled finding the required resolution while keeping computational costs as low as possible.

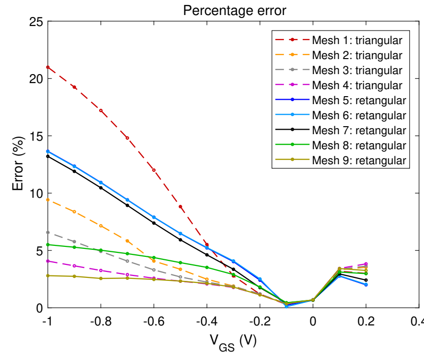

Figure 2.15: The error of the numerical solution of the conductivity at $V_{\text{DS}} = 0\,\text{V}$ of the 2D compared to the 1D model for 9 different meshes over the applied gate potential. Parameters used in the calculations: $n_{\text{h}} = 6 \times 10^{15}\,\text{cm}^{-3}, \varepsilon_{\text{r,sem}} = 4, h_{\text{sem}} = 30\,\text{nm}, h_{\text{elec}} = 170\,\text{nm}, c_{\text{G}} = 0.0243\,\mu\text{F/cm}^2, c_{\text{S}} = c_{\text{int}} = 10^4\,\mu\text{F/cm}^2, T = 293.15\,\text{K}$.

2.4.4 Stationary Condition

The calculations presented until here and throughout the thesis are done with a time-dependent solver, where the time-step is automatically adjusted with a Runge-Kutta algorithm. Further information can be found in the COMSOL user guide [60]. To investigate the time-response of the system, a voltage step of

-0.1 V was applied, and every internal time step was evaluated. In Figure 2.16, the measured current follows the input signal with a delay of 0.005 ms when applying a step signal. When the model reaches a non-continuous part of the input function, the output needs time to recover the solution. When applying a signal with no discontinuities, the current follows the input signal with no significant delay Figure 2.17.

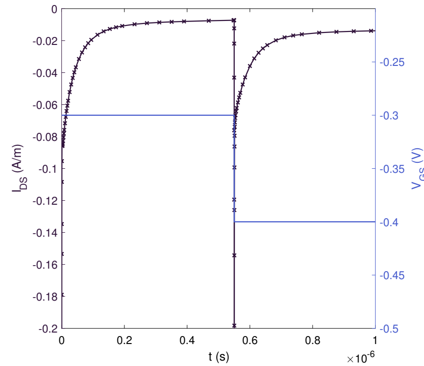

Figure 2.16: Step response of the model for a -0.1 V step. COMSOL Multiphysics is adjusting the time-step internally. Parameters used in the calculations: $n_{\mathrm{h}} = 6 \times 10^{15}\,\mathrm{cm}^{-3}, \varepsilon_{\mathrm{r,sem}} = 4, h_{\mathrm{sem}} = 30\,\mathrm{nm}, h_{\mathrm{elec}} = 170\,\mathrm{nm}, c_{\mathrm{G}} = 0.0243\,\mu\mathrm{F/cm}^2, c_{\mathrm{S}} = c_{\mathrm{int}} = 10^4\,\mu\mathrm{F/cm}^2, T = 293.15\,\mathrm{K}$.

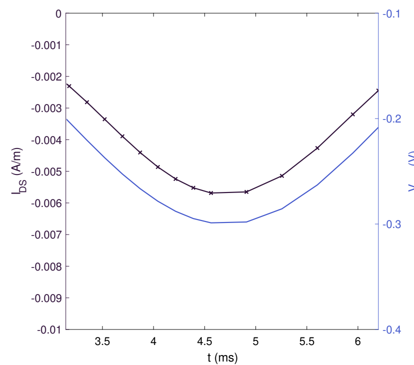

Figure 2.17: Time-dependent continuous input signal at the gate electrode (blue line) with the corresponding source-drain current (black line). Parameters used in the calculations: $n_{\mathrm{h}} = 6 \times 10^{15}\,\mathrm{cm}^{-3}, \varepsilon_{\mathrm{r,sem}} = 4, h_{\mathrm{sem}} = 30\,\mathrm{nm}, h_{\mathrm{elec}} = 170\,\mathrm{nm}, c_{\mathrm{G}} = 0.0243\,\mu\mathrm{F/cm}^2, c_{\mathrm{S}} = c_{\mathrm{int}} = 10^4\,\mu\mathrm{F/cm}^2, T = 293.15\,\mathrm{K}$.

Above we showed that a discontinuous voltage signal leads to numerical errors, which need a short time to recover towards convergency. To avoid this, the steps are smoothened to avoid undefined derivatives of the input signal. Figure 2.18 displays the input signal (blue line) with the corresponding source-drain current (black line). The voltage input at the gate is time-dependent, whereas the voltages after each step are kept constant for 0.1 s until the next voltage step of $\Delta V = -0.1$ V.

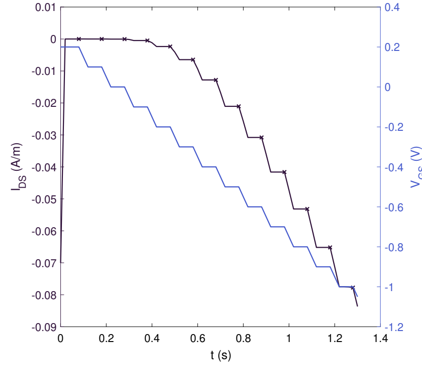

Figure 2.18: Time-dependent input signal at the gate electrode and device response of the source-drain current. The evaluation of the signal is done at the last time step of every voltage to ensure a static solution (marked with 'x'). Parameters used in the calculations: $n_\mathrm{h} = 6 \times 10^{15}\,\mathrm{cm}^{-3}, \varepsilon_{\mathrm{r,sem}} = 4, h_{\mathrm{sem}} = 30\,\mathrm{nm}, h_{\mathrm{elec}} = 170\,\mathrm{nm}, c_\mathrm{G} = 0.0243\,\mu\mathrm{F/cm}^2, c_\mathrm{S} = c_{\mathrm{int}} = 10^4\,\mu\mathrm{F/cm}^2, T = 293.15$ K.

In Figure 2.19, we present the voltage cutline over the middle of the channel for different voltages and time steps. The output is evaluated at the last time step of each voltage step, ensuring the static solution at the given time step. When we keep the voltage unchanged and alter the time-step, we observe an identical potential distribution. This indicates that we are in a quasi-static condition.

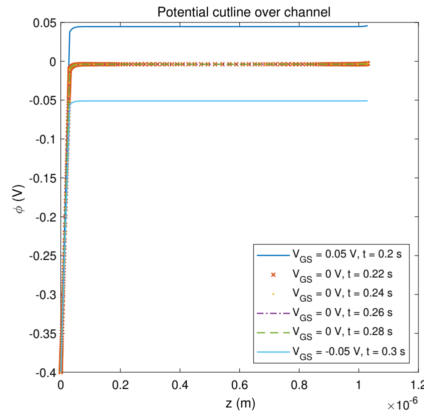

Figure 2.19: Voltage cutline over the middle of the channel for different voltages and time steps. Parameters used in the calculations: $n_\mathrm{h} = 6 \times 10^{15}\,\mathrm{cm}^{-3}, \varepsilon_\mathrm{r,sem} = 4, h_\mathrm{sem} = 30\,\mathrm{nm}, h_\mathrm{elec} = 170\,\mathrm{nm}, c_\mathrm{G} = 0.0243\,\mu\mathrm{F/cm}^2, c_\mathrm{S} = c_\mathrm{int} = 10^4\,\mu\mathrm{F/cm}^2, T = 293.15$ K.

Figure 2.20 shows the dependence of the drain-source current against the drain-source potential, namely the output curve of the EGOFET. The output characteristics are calculated in two cases; altering the gate voltage and altering the drain voltage. As evident from the graph, both studies' outcomes coincide, indicating that the output curve ends up in the same solution as a direct sweep over the drain voltage. More importantly, the output curves of the following chapters can be calculated from the transfer curves because the solution is the same for the given set of voltages.

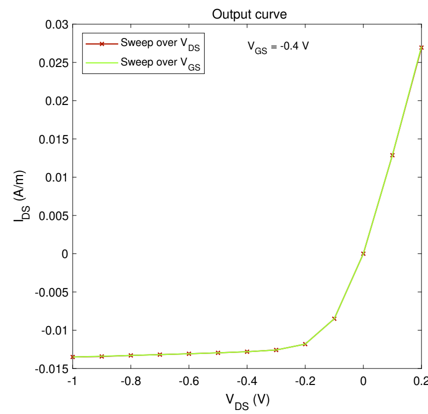

Figure 2.20: Output characteristics calculated from the sweep of the gate voltages, overlayed with the direct calculation of the output characteristics (sweep of the drain voltage). We give an example for $V_{\mathrm{GS}} = -0.4\,\mathrm{V}$. Parameters used in the calculations: $n_{\mathrm{h}} = 6 \times 10^{15}\,\mathrm{cm}^{-3}, \varepsilon_{\mathrm{r,sem}} = 4, h_{\mathrm{sem}} = 30\,\mathrm{nm}, h_{\mathrm{elec}} = 170\,\mathrm{nm}, c_{\mathrm{G}} = 0.0243\,\mu\mathrm{F/cm}^2, c_{\mathrm{S}} = c_{\mathrm{int}} = 10^4\,\mu\mathrm{F/cm}^2, T = 293.15\,\mathrm{K}$.

2.5 Summary

- The Helmholtz model is a simplified EGOFET model in two-dimensions, where the electrolyte is described as a distributed capacitance.
- The NPP framework provides the system of equations that are solved.
- The positive and negative ions in the solution are equally concentrated, defined by the initial concentration as on all boundaries there is a no flux BC
- Only the majority charge carriers (holes) have been modeled in the semiconductor domain.
- The holes are injected into the semiconductor at the source electrode.
- The EGOFET has been modeled in a finite-element system in one and two dimensions.
- The real three-dimensional device can be transformed into a two-dimensional system, as the third dimension is just the system's depth.
- The two-dimensional system can be described by two one-dimensional approaches: one at the electrode and one in the middle of the channel.
- The one-dimensional model delivers fast results but still models the charge and potential distribution in the EGOFET in some situations.
- We showed that in the one-dimensional case, mesh convergence is achieved with an element size of 0.1 nm at the interface where the electrical double layer is 0.5 nm.
- The module-based and coefficient-based numerical model match with less than 3% error with an analytical solution.
- We observed a higher accuracy in meshing with quads than with triangles.
- Using rectangular meshes with a similar distribution in z-direction as in the one-dimensional numerical model, the models match with an accuracy of 3% in the range of $V_{GS} = [0.2 - 1]$ V the exact analytical solution.

PART III

RESULTS

Chapter 3

EGOFET in the Helmholtz Approximation

As we have mentioned before, the physical modeling of EGOFET can be addressed at different levels of approximation, whereas the Helmholtz approximation is the simplest one. In the Helmholtz approximation, the electrolyte is considered a distributed boundary condition and not an explicit part of the model. This reduces the computational cost due to fewer variables and smaller domains. We implemented and validated the numerical resolution of the 2D Helmholtz model for EGOFETs in chapter 2 with the analytical solution derived for long channel lengths [62]. This chapter presents the results obtained with the numerical implemented model. In particular, we analyze the predicted current-voltage characteristics and the dependence on the channel length. This chapter aims to provide a baseline for the analysis of more complex models treated in the subsequent chapters.

3.1 Current-Voltage Characteristics

As we mentioned in the introduction, the current-voltage characteristics are typically measured in biosensing applications to characterize the device and give the source-drain current flowing through the device as a function of the source-gate voltage (transfer curves) or as a function of the source-drain voltage (output curves). Figure 3.1 (a) shows, respectively, the transfer and (b) output current-voltage characteristics corresponding to an EGOFET in the Helmholtz approximation simulated by the numerical method implemented in this thesis and described in chapter 2.

Figure 3.2 (a) shows the transfer current-voltage characteristics plotted in logarithmic-linear representation, while in 3.1 (b), we plot the square root of the current as a function of V_{GS}. The current-voltage characteristics show the typical behavior of a FET device, as expected since the model is equivalent to a thin film transistor (TFT) model. The device operates in the saturation regime for high drain voltages of $V_{DS} > V_{GS} + V_{th}$ and $V_{GS} < V_{th}$ (dashed line in Figure 3.1, b). In this regime, the channel pinches off, as shown below in the analysis of the conductivity profiles. The current scales with the square of V_{GS} in the saturation regime (see Figure 3.1, b), as usual in FET devices. The device has a linear dependency on the drain voltage for low voltages ($V_{DS} \ll V_{GS} + V_{th}$), followed by a transition regime. Finally, for $V_{GS} > V_{th}$, the device enters the sub-threshold regime, where the I-V curve shows an exponential dependence on V_{GS} (Figure 3.1, a). In the subthreshold regime, the transfer curves are indifferent at negative drain voltages (see Figure 3.1, a). In this Chapter, unless otherwise stated, the parameters of the model are those reported in Table 3.1.

Table 3.1: Parameters of the Helmholtz model.

Parameter	Value
Carrier concentration n_h	$6 \times 10^{21}\,1/m^3$
Carrier mobility μ_{sem}	$3.4 \times 10^{-6}\,m^2/(Vs)$
Semiconductor thickness h_{sem}	$30\,nm$
Electrode length $l_{electrode}$	$1\,\mu m$
Relative permittivity semiconductor $\varepsilon_{r,sem}$	4
Channel length $l_{channel}$	$10\,\mu m$
Electrolyte's distributed capacitance c_H	$0.01\,F/m^2$

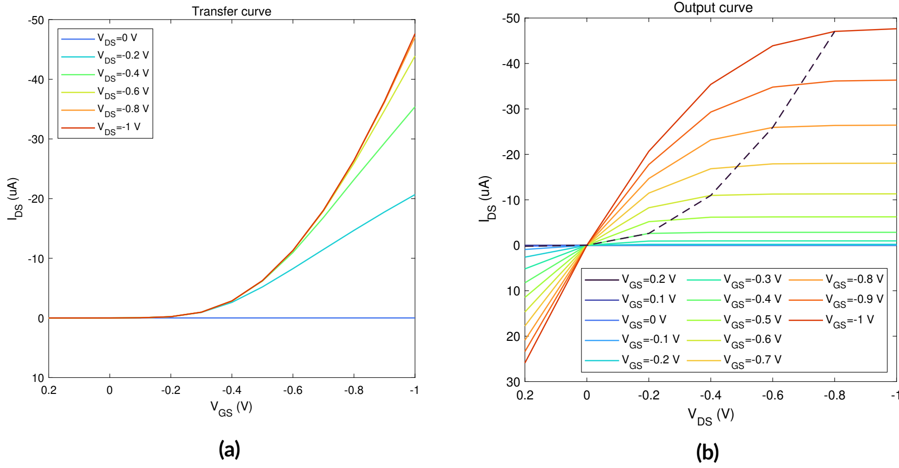

Figure 3.1: (a) Transfer characteristics in linear scale. For voltages below the threshold, the device is in off-state. For low drain voltages, the device operates in the linear regime. For high drain voltages, the current saturates. (b) Output characteristics of the EGOFET in the Helmholtz approximation. The electrolyte is not explicitly described. However, the typical output characteristics are observed. The linear and saturation regime with a broad transition in-between is apparent. Parameters are given in Table 3.1.

The threshold voltage can be estimated from the transfer current-voltage characteristics by either considering a V_{DS} in the linear regime (as explained in chapter 1) or by considering a V_{DS} in the saturation regime and plotting $||IDS||^{0.5}$ vs. V_{GS} (as in Figure 3.1 , b). In both cases, the threshold voltage is $V_{\mathrm{th}} \approx -0.22$ V. Later, when considering diffusive effects in the NPP model, the definition of V_{th} is more complex.

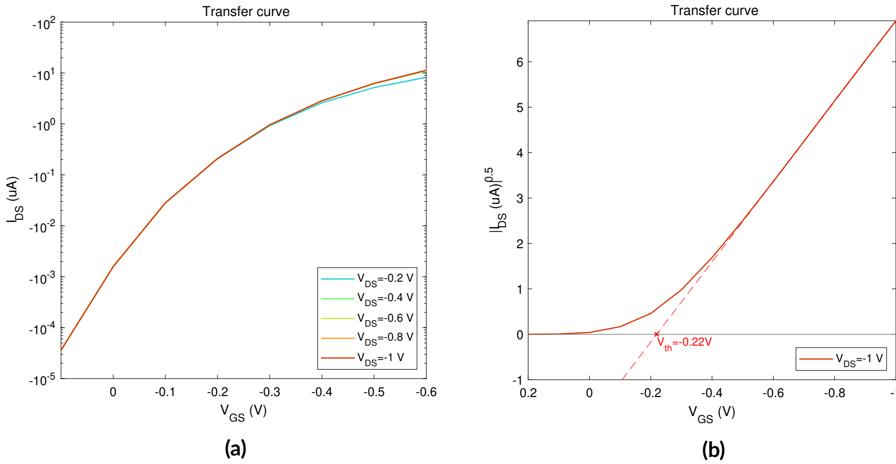

Figure 3.2: (a) Transfer curve in log scale and (b) the root of the transfer curve in saturation with $V_{DS} = -1$ V to obtain the threshold voltage V_{th}. Parameters are given in Table 3.1.

For further analysis purposes, it is worth defining the "macroscopic" (or global) conductivity of the device that can be obtained in experimental setups from the conductance of the current-voltage characteristics as

$$\sigma_{macro}(V_{GS}, V_{DS}) = \frac{L}{W h_{sem}} \frac{\partial I(V_{GS}, V_{DS})}{\partial V_{DS}}. \tag{3.1}$$

Figure 3.3 (a) shows the macroscopic conductivity for the current-voltage output curve in Figure 3.1 (b) as a function of V_{GS} for the different V_{DS}. The interesting property of the data is that when plotted against $V_{GS} - V_{DS}$, the curve collapse for $V_{GS} < V_{DS}$ to the conductivity characteristics at $V_{DS} = 0$ V. This fact is an indication that the device can be well described by means of the so-called gradual channel and space charge transport approximations, which is at the basis of the derivation of an analytical solution for the I-V characteristics in the Helmholtz approximation (see [62] for further details).

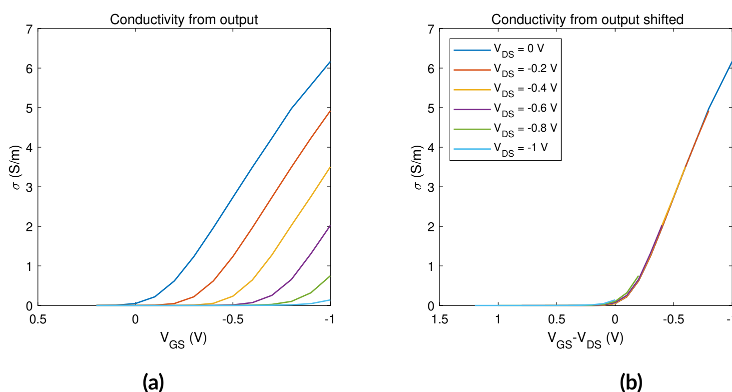

Figure 3.3: (a) Conductivity calculated from the output curve corresponding to Equation (3.1). (b) Conductivity curves shifted with respect to the applied drain voltage. Parameters: those in Table 3.1.

Besides the current-voltage characteristics, which can be measured in experimental setups, the numerical simulations offer the possibility to analyze the spatial distribution of the different physical magnitudes like the voltage, free carrier density, or sheet conductivity. Numerical models allow mapping these changes and correlating them with the macroscale output. We analyze them in the following subsection.

3.2 Semiconductor Conductivity Distribution and Voltage Dependence

In an EGOFET, the local conductivity $\sigma(x,z) = e\mu_\mathrm{p} p(x,z)$ depends on the longitudinal and transversal directions. Figure 3.4 shows an example of a local conductivity distribution inside the semiconductor film for $V_\mathrm{GS} = -0.6\,\mathrm{V}$ and different source-drain voltages. It demonstrates how the charges are strongly accumulated towards the top surface of the semiconductor, below the gate. The accumulation of free charge carriers is responsible for making the semiconductor conductive. For low V_DS, the conductivity is nearly uniform along the device. At around $V_\mathrm{DS} = -0.4$ V, the charge accumulation above the drain electrode starts to be lower until, for lower voltages, they practically do not accumulate there, forming the so-called pinch-off.

Therefore, the numerical simulations allow observing the formation of the conduction channel with the accumulation of a high density of holes at the surface of the semiconductor and how the pinch-off is formed close to the drain region as the drain voltage is high enough (negative) such that $V_\mathrm{GS} < V_\mathrm{DS} + V_\mathrm{th}$ is satisfied. In this range, the conductivity values at drain electrodes remain at the intrinsic level.

Rather than analyzing the local conductivity, one usually analyses the local sheet conductivity to eliminate the vertical dependencies since the variations along it are much faster. The local sheet conductivity along the semiconductor channel is defined by integrating the local conductivity along the vertical direction

$$\sigma(x) = \frac{\mu_\mathrm{p}}{h_\mathrm{sem}} e \int_0^{h_\mathrm{sem}} p(x,z)\,\mathrm{d}z. \tag{3.2}$$

where h_sem is the thickness of the semiconductor film, μp is the hole mobility, e is the elementary charge, and p is the local concentration of holes. The conductivity along the semiconductor is directly correlated to the sheet accumulated charge. The sheet conductivity for $V_\mathrm{GS} = -0.6\,\mathrm{V}$ is displayed in Figure 3.5 for different V_DS. For $V_\mathrm{DS} = 0\,\mathrm{V}$ and low (negative) V_DS, the sheet conductivity is almost uniform throughout the entire device. When V_DS becomes more negative, the sheet conductivity tends to decrease towards the drain. The lowered conductivity results in the pinch-off effect at the drain electrode for $V_\mathrm{DS} = -0.4\,\mathrm{V}$ and nearly zero conductivity for more negative voltages.

Figure 3.6 gives the electric field distribution to show its relevance to the pinch-off point [46]. For the pinch-off voltage, the electric field over the drain voltage becomes nearly zero.

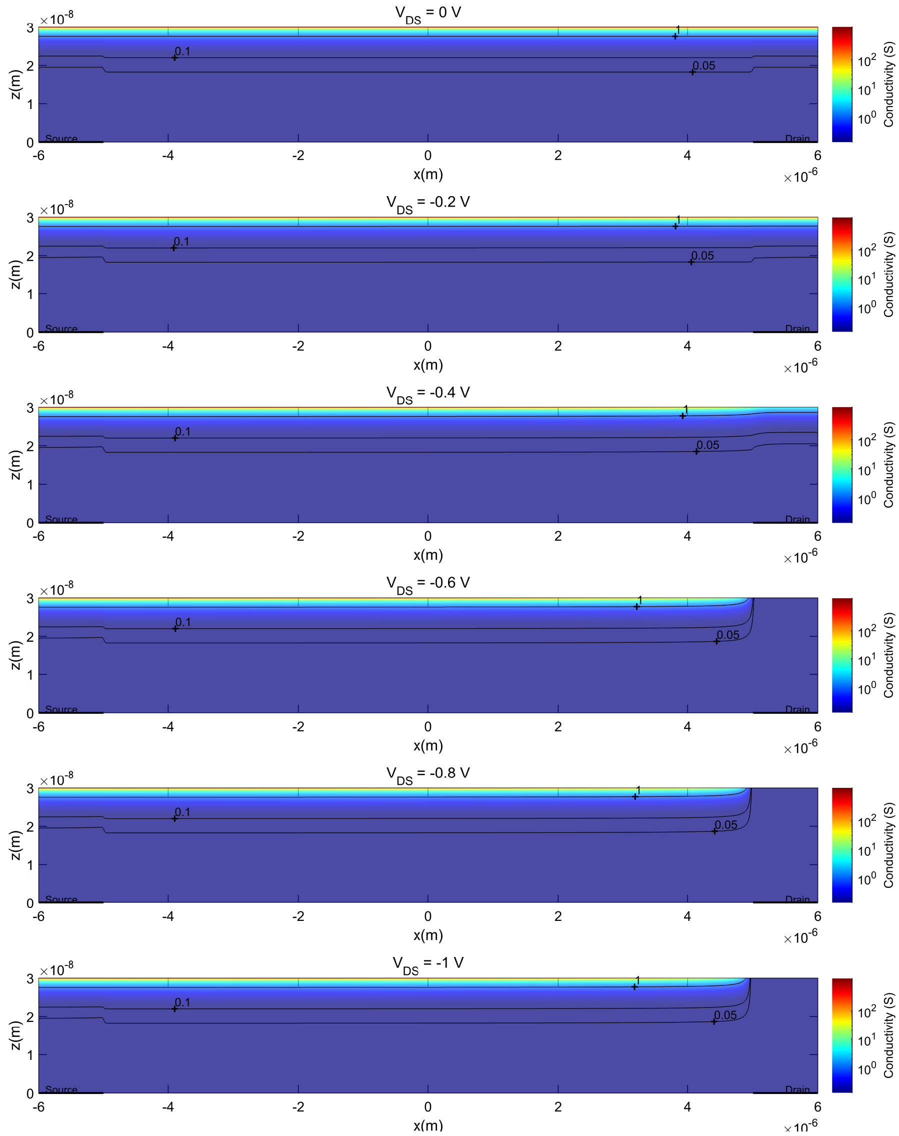

Figure 3.4: (a) Conductivity map for $V_{GS} = -0.6$ V and different V_{DS} values. For $V_{DS} = -0.6$ V, the holes do not accumulate anymore over the drain electrode (pinch-off). Parameters are given in Table 3.1.

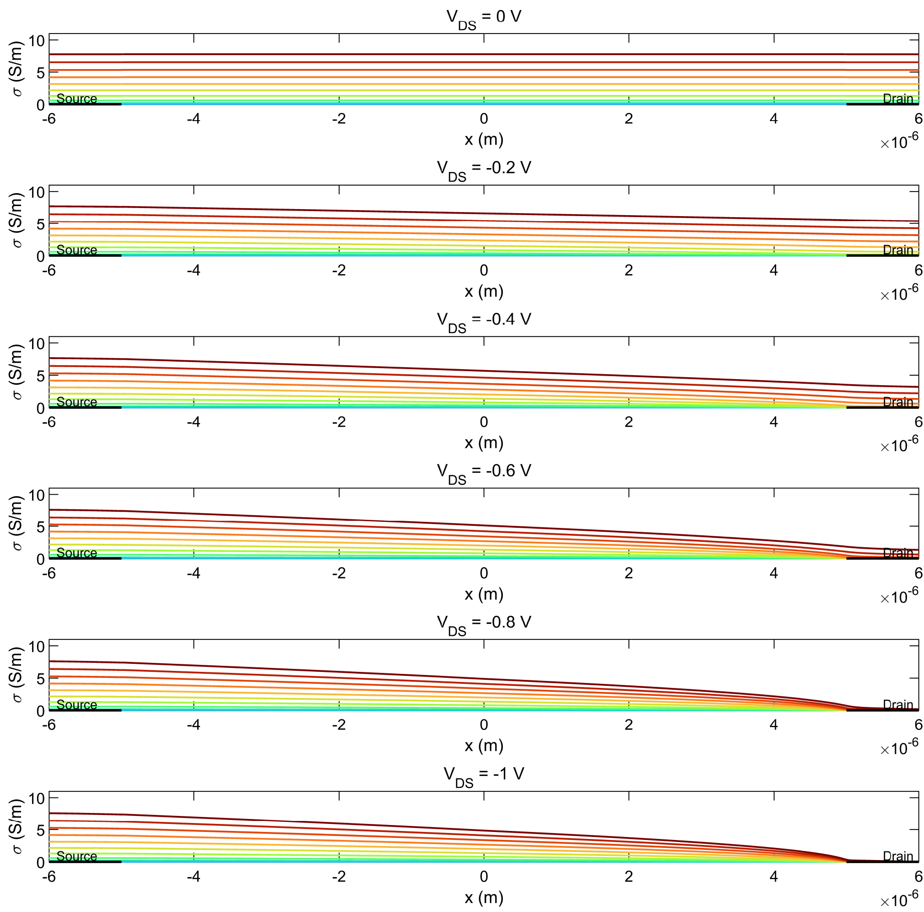

Figure 3.5: Sheet conductivity along the channel and above the source and drain electrode. For drain voltages in the saturation regime, the conductivity above the drain becomes close to zero after the pinch-off point. Most free charge carriers close to the drain go over to the drain electrode outside the system. Parameters are given in Table 3.1.

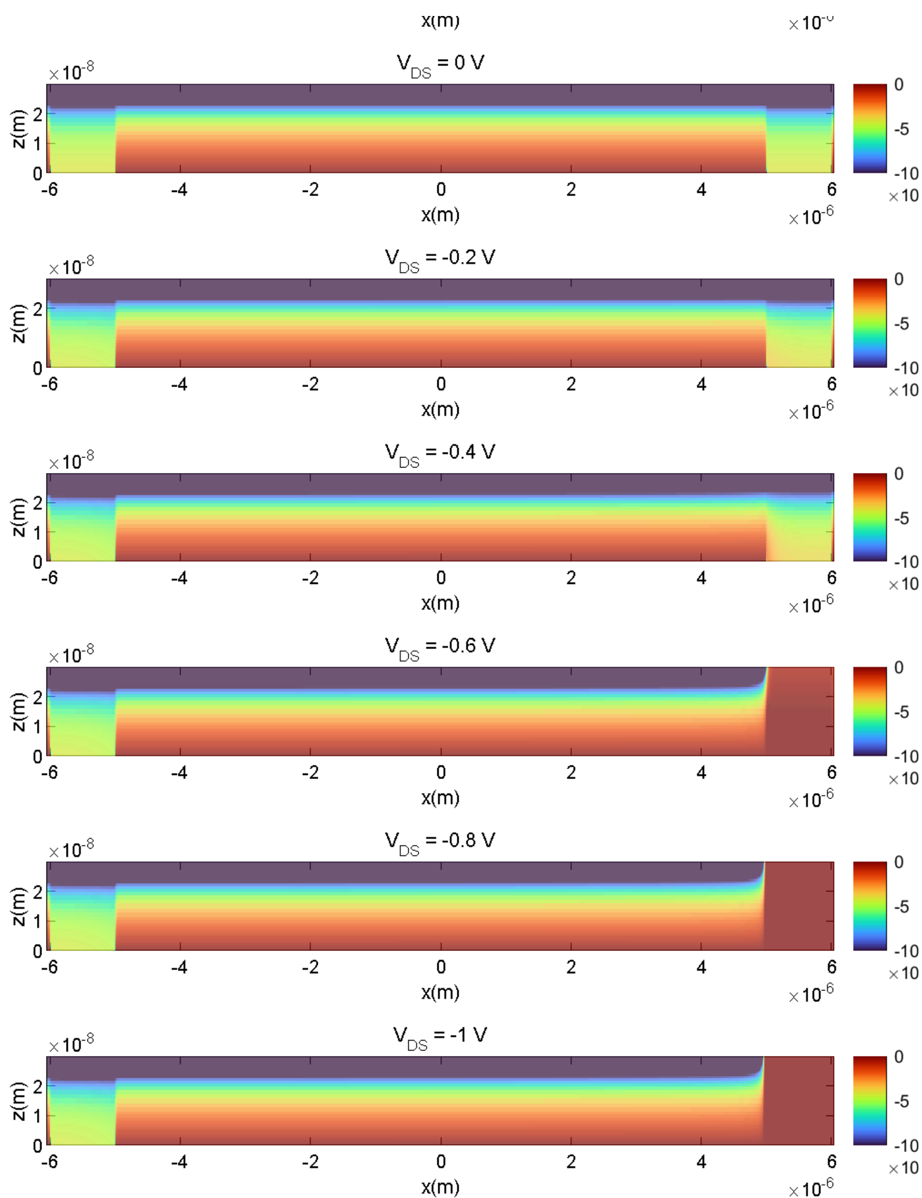

Figure 3.6: Electric field in the semiconductor for $V_{GS} = -0.6\,\mathrm{V}$.Parameters are given in Table 3.1.

The variations of the sheet semiconductor conductivity with the applied voltages can be better visualized by plotting their variations in selected transistor positions. Figure shows the sheet semiconductor conductivity in the middle of the channel ($x = L/2$) against the gate voltage in linear and logarithmic scales for different drain voltages.

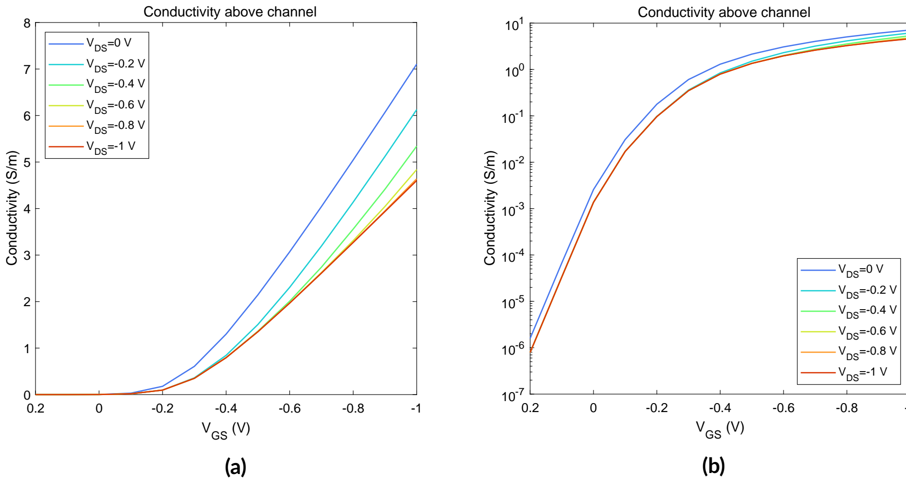

Figure 3.7: (a) Sheet conductivity for different drain voltages in the middle of the channel in linear and (b) log scale. Parameters are given in Table 3.1.

Figure 3.7 shows the sheet conductivity above in the middle of the source electrode. It can be seen that it nearly does not vary with the drain voltage since the source is always grounded. The conductivity is also linear for $V_{GS} - V_{DS} > V_{th}$, but it deviates from the pure exponential behavior conductivity at the source electrode deviates from the pure exponential dependence for $V_{GS} - V_{DS} > V_{th}$, showing an inverse voltage dependence ultimately, as explained theoretically in [62].

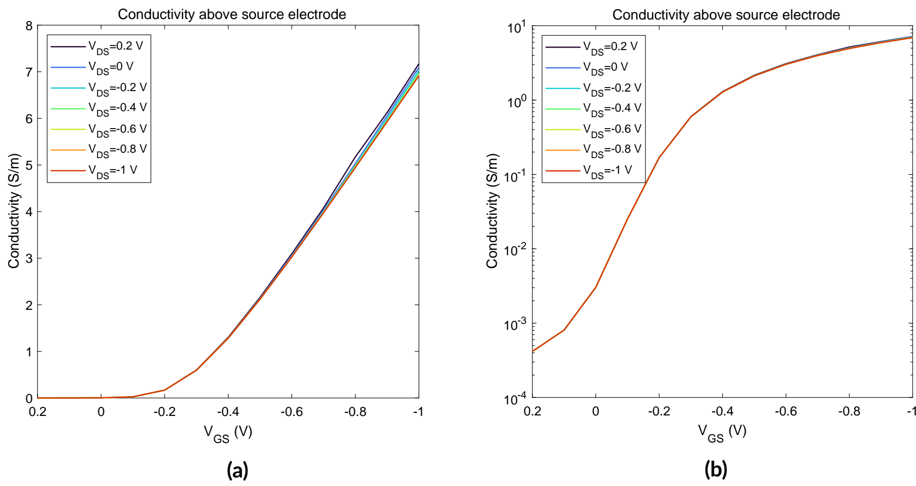

Figure 3.8: (a) Sheet conductivity for different drain voltages above the electrode in linear and (b) log scale. Parameters are given in Table 3.1.

Finally, over the drain electrode, the dependence as a function of V_{GS} is qualitatively similar to that of the source but with the values shifted by V_{DS} (see Figure 3.9).

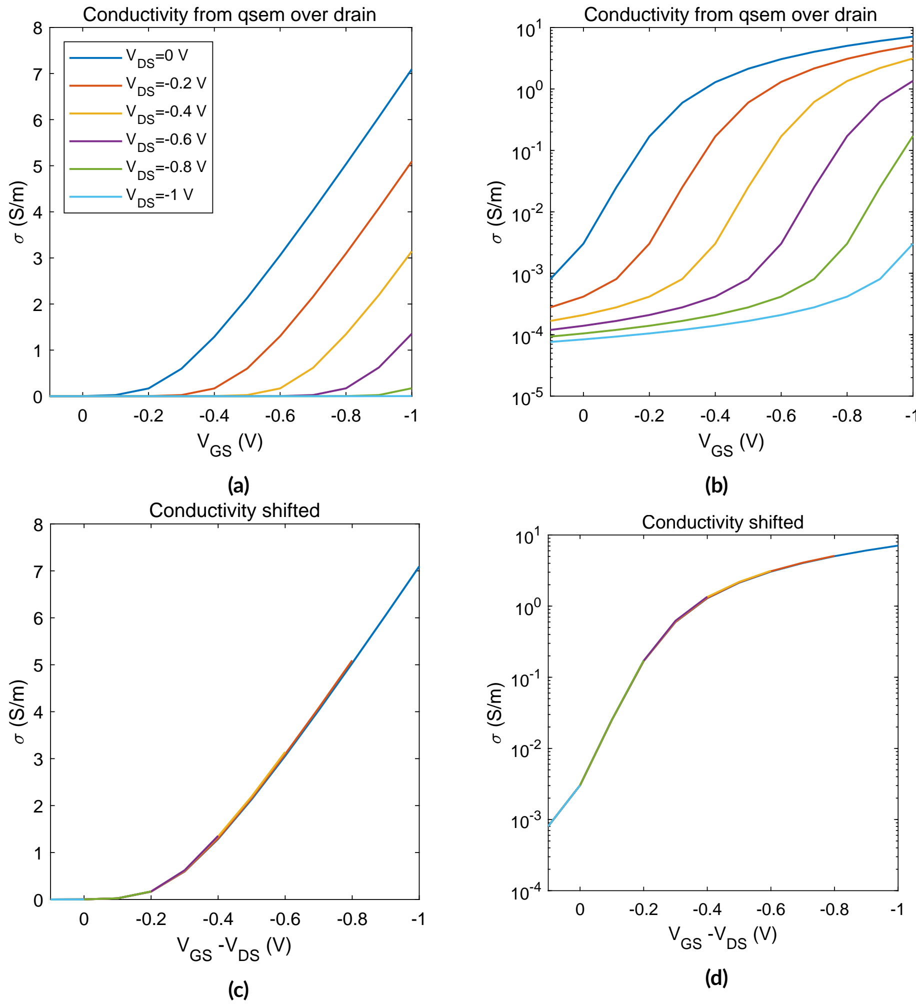

Figure 3.9: Conductivity for different drain voltages above the drain electrode in (a) linear and (b) logarithmic scale. (c+d) The corresponding V_{DS} shifts the conductivity curves. Parameters are given in Table 3.1.

The conductivity curves for $V_{DS} = 0\,\text{V}$ are identical in the three positions since the conductivity profiles are flat and constant throughout the device (see Figure 3.5). The dependence on V_{GS} of the curves for $V_{DS} = 0\,\text{V}$ can be theoretically understood by considering one-dimensional metal/insulator/semiconductor/metal and metal/insulator/semiconductor/insulator models, as was done in [57].

The dependence on V_{DS} is correlated to the potential drops along the channel due to the current. Therefore, the local gate voltage at each position is the actual gate voltage minus the voltage drop along the channel. For $V_{\mathrm{DS}} < V_{\mathrm{GS}} - V_{\mathrm{th}}$, the local potential is nearly zero around the drain, thus making the carrier density very low (pinch-off regime). The pinch-off point is defined for each gate voltage as the point where the source-drain current is no longer dependent on the drain voltage. Then the device operates in a saturation regime. The corresponding voltage is given by the correlation of

$$V_{\mathrm{DS}} = V_{\mathrm{GS}} - V_{\mathrm{th}}\,, \tag{3.3}$$

where V_{th} is the threshold voltage, marked in Figure 3.1 (intercept of dotted line). Finally, the relationship between the macroscopic conductivity calculated above and the sheet conductivity discussed is worth mentioning. In the transistor, the magnitudes along the transversal direction of the semiconductor channel vary more rapidly than along the longitudinal direction. Under these conditions, one can apply the gradual channel and space charge limited approximations in which diffusive effects can be neglected along the horizontal direction and transversal variations integrated out. Under these approximations, the source-drain current I_{DS} can be calculated as

$$I_{\mathrm{DS}}\left(V_{\mathrm{DS}}, V_{\mathrm{GS}}\right) = -\frac{W h_{\mathrm{sem}}}{L} \int_{0}^{L} \sigma_{\mathrm{sheet}}\left(x\right) \frac{\partial V\left(x\right)}{\partial x}\,\mathrm{d}x, \tag{3.4}$$

where W and L are the width and length of the semiconductor channel, and the local sheet semiconductor conductivity is obtained by integrating the accumulated charge along the transversal semiconductor direction. The spatial variation of the conductivity along the semiconductor channel for a given applied source-drain voltage V_{DS} is approximated by the conductivity at $V_{DS} = 0\,\mathrm{V}$ evaluated at the corresponding local "gate" voltage by

$$\sigma\left(x\right) = \sigma_{\mathrm{sheet},0}\left(V_{\mathrm{GS}} - V\left(x\right)\right), \tag{3.5}$$

where $V(x)$ is the electric potential drop along the channel and $\sigma_0(V_{\mathrm{GS}})$ the zero source-drain voltage sheet semiconductor conductivity. By substituting Equation (3.4) into Equation (3.5) and making a change of variables, one obtains

$$I_{\mathrm{DS}}\left(V_{\mathrm{DS}},V_{\mathrm{GS}}\right) = -\frac{W h_{\mathrm{sem}}}{L} \int_{V_{\mathrm{GS}}}^{V_{\mathrm{GS}}-V_{\mathrm{DS}}} \sigma_{\mathrm{sheet},0}\left(V\right)\ \mathrm{d}V\,. \tag{3.6}$$

Accordingly, the relation between both conductivities should be

$$\sigma_{\mathrm{macro}}\left(V_{\mathrm{GS}},V_{\mathrm{DS}}\right) \approx \sigma_{\mathrm{sheet},0}\left(V_{\mathrm{GS}}-V_{\mathrm{DS}}\right). \tag{3.7}$$

This result explains why the macroscopic conductivity data shifted and collapsed in a single curve. The single curve is the local conductivity at $V_{\mathrm{DS}} = 0\,\mathrm{V}$, which is uniform. Figure 3.10 compares the two types of conductivities for the device analyzed. We observe that for $V_{\mathrm{DS}} = 0\,\mathrm{V}$, the two conductivities agree, as shown above. However, when V_{DS} is different from 0 V there is some discrepancy between both of them. This discrepancy is due to access series resistance effects, which are still relevant in a device with $L = 10\,\mu\mathrm{m}$, as shown below.

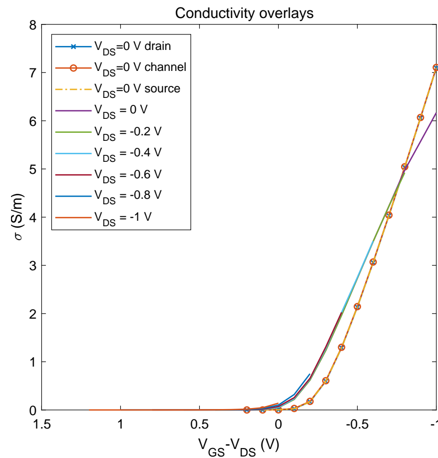

Figure 3.10: Comparison of the macroscale conductivity σ_{macro} with the local conductivity $\sigma local, 0$. The conductivity $\sigma_{\mathrm{local},0}$ over source, drain and gate is indifferent. Parameters are given in Table 3.1.

As we mentioned, access series resistance effects can play a relevant role in staggered EGOFETs. We have conducted numerical calculations for different channel lengths to demonstrate it. Figure 3.11 (symbols) shows output ($V_{\mathrm{GS}} = -0.6\,\mathrm{V}$) and transfer ($V_{\mathrm{DS}} = -0.8\,\mathrm{V}$) current-voltage characteristics calculated numerically with the 2D Helmholtz model for an EGOFET with different channel

lengths and the same W/L ratio. The continuous black line corresponds to the long channel limit, which only depends on the W/L ratio, hence, it is the same in all cases since the ratio W/L is kept constant. The source-drain current markedly deviates (reduced) from the prediction of the long channel limit for $L < 30\,\mu\text{m}$. We have shown that the deviation is due to the presence of series access resistance effects, i.e. the series resistance associated with the path of the carriers from the injecting electrode at the bottom of the semiconductor film to the conducting channel at its top surface [62]. The access resistance becomes relevant for small channel lengths since the channel resistance becomes comparable to the access resistance and a significant part of the applied voltages drop at it. For long channel lengths (e.g. $L > 60\,\mu\text{m}$), the series resistance effects become negligible, and the current only depends on the W/L ratio.

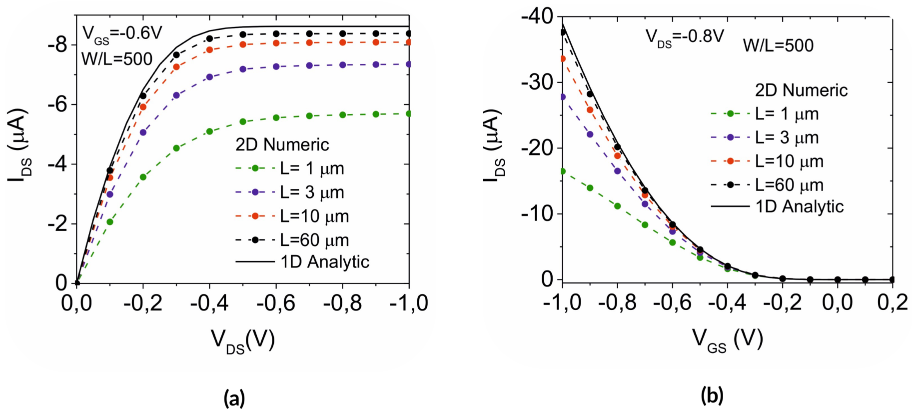

Figure 3.11: (a) Output ($V_{GS} = -0.6\,\text{V}$) and (b) transfer ($V_{DS} = -0.8\,\text{V}$) I-V characteristics for EGOFETs with different channel lengths, L, and same W/L ratio numerically calculated by solving the 2D Helmholtz model (symbols). The continuous lines correspond to the analytical solution valid in the long channel limit.

3.3 Summary

- This chapter showed that the Helmholtz model can be used as a simplified EGOFET model. It can properly mimic the EGOFET's current-voltage characteristics. This model is suitable for investigations where the gate electrode's ionic strength and geometries (e.g. surface and distance) do not play a role.
- We correlated the output characteristics with the saturation regime and the pinch-off points in the conductivity across the channel.
- We showed the variability of the conductivity behavior over the channel, source and drain electrode.
- We analyzed the role of the channel length in relation to the series access resistance.

Chapter 4

MES Capacitor in the NPP Framework

In the previous chapter, we showed the simulation of an EGOFET, where the electrolyte was considered a Helmholtz capacitance. While this saves computational costs, it does not mimic the effects related to electrolyte coupling. To overcome these limitations, one needs to include the transport physics of the electrolyte, which can be done by considering the NPP framework, as discussed in chapter 2. Before addressing the two-dimensional modeling of EGOFET in this framework, we will consider first the one-dimensional metal/semiconductor/electrolyte (MES) capacitor structure, which includes a lot of the physics required to model complete EGOFET devices. As explained in chapter 2, one-dimensional MES structures represent transversal cut-lines of the EGOFET transistor, which describe the physics for $V_{\mathrm{DS}} = 0\,\mathrm{V}$ and long channels. In addition, they can also represent stand-alone capacitive devices for testing purposes. The one-dimensional model can be solved analytically [57], thus offering a perfect situation to benchmark the implemented numerical calculations. Finally, since the model can be run in a few minutes, it is well suited for systematic parametric studies. In this chapter, we investigate several device parameters and elaborate on the dependency of the different phenomenological parameters on them. This allows comparing the changes in capacitance and threshold voltage in the classical biosensing applications, where biorecognition layers are added. The details of the model implementation have been given in Chapter 2, and here we present the results.

4.1 Potential and Charge Distribution

In Chapter 2, the three different implementations, which give identical results, are described. Here, we use the one based on the equation-based modeling with the PDE interface, which is the one that offered the largest versatility. Throughout this chapter, unless otherwise stated, we will consider the parameters in Table 4.1 in the calculations. All parameters in the Table are characteristic of EGOFET except the electrolyte thickness, which is much larger. Here we used this small value to evidence the space charge layers but also considered more significant and more physically relevant values to analyze the macroscopic magnitudes (e.g. device capacitance or conductivity). It should be noted that the device properties become independent from the electrolyte thickness for thickness above a few micrometers.

Table 4.1: Parameters used in the calculations of the one-dimensional NPP model, if not otherwise stated.

Parameter	**Value**
Carrier concentration n_h	$6 \times 10^{21}\,\mathrm{m}^{-3}$
Carrier mobility μ_h	$3.4 \times 10^{-6}\,\mathrm{m}^2/(\mathrm{Vs})$
Ion concentration n_0	1 mM
Ion mobility μ_{elec}	$3.9 \times 10^{-8}\,\mathrm{m}^2/(\mathrm{Vs})$
Semiconductor thickness h_{sem}	30 nm
Electrolyte thickness h_{elec}	1000 nm
Relative permittivity semiconductor $\varepsilon_{r,sem}$	4
Relative permittivity electrolyte $\varepsilon_{r,elec}$	78
Gate distributed capacitance c_G	$0.0243\,\mathrm{F/m}^2$
Interfacial distributed capacitance c_{int}	$1 \times 10^4\,\mathrm{F/m}^2$
Source distributed capacitance c_S	$1 \times 10^4\,\mathrm{F/m}^2$

The ions move under the influence of the electrical field inside the electrolyte. Likewise, the free charge carriers (holes) migrate in the semiconductor film, contributing to the electric potential distribution. For the parameters reported in Table 4.1, the potential and charge carrier distributions are displayed in Figure 4.1. Figure 4.1 (a + b) gives the distributions across the MES structure above the channel, whereas (c + d) displays the voltage and charge distribution above the MES structure above the source electrode. We remind that the difference between them is the bottom layer below the semiconductor, in one case an insulator, and

the other metal. Since the one-dimensional model is only valid for $V_{DS} = 0\,\text{V}$, the distribution over the source and drain electrode is the same.

The distributions over the semiconductor correspond to $0\,\text{nm} < z < 30\,\text{nm}$ and for the electrolyte to $30\,\text{nm} < z < 200\,\text{nm}$ (for this calculation, we used $h_{elec} = 170\,\text{nm}$ to better evidence all the space charge layers). At $z = 200\,\text{nm}$, the linear voltage drop is caused by the interfacial layers' distributed capacitance (Stern layer), plotted by the black line. However, this layer is only implicitly constrained by a boundary condition in the simulation. Interfacial layers consist of the capacitance between the electrolyte and the semiconductor c_{int}, the capacitance at the gate electrode c_G, and the capacitance at the source electrode c_S. In the simulations shown in Figure 4.1, the capacitance of c_{int} and c_S are set to a very high value ($> 1 \times 10^4\,\text{F/m}^2$), so they do not influence the system. The capacitance of c_G is set to the Stern layer capacitance. The holes form a space charge layer for higher negative gate voltages, expressing the presence of the transistor's conductive channel. At the same time, the electrolyte absorbed a part of the potential forming diffusive ionic space charge layers (see Figure 4.1 a + b). The electric potential and the hole density form an almost uniform distribution over the device for positive voltages. The ionic diffusive space charge layers are not significantly developed for these voltages, and nearly no voltage drops at the electrolyte interfaces.

The semiconductors' voltage distribution above the electrode and the channel show significant differences due to the electrode's fixed voltage and hole concentration. Above the channel, this boundary is defined by the voltages outside the system. In Figure 4.1, the voltage at $z = 0\,\text{nm}$ shows fewer changes for higher negative gate voltages. The simulations over the channel are given for $V_{GS} = \{0.1, 0, -0.1, -0.2\}$ V; convergence was not achieved for higher negative gate voltages. In the following chapter, we will discuss this behavior also for higher voltages in the two-dimensional simulation.

In the charge distribution (see Figure 4.1, c + d), the strong amplification character of EGOFET devices can be observed. A small change in the gate voltage induces a substantial change in the charge accumulated at the semiconductor surface, leading to a high increase in its conductivity and hence current between source and drain. Figure 4.1 (e + f), the charge accumulation in the semiconductor on a logarithmic scale is displayed to visualize the behavior in small gate voltages. For $V_{GS} = 0\,\text{V}$, there is no charge accumulation at the interface.

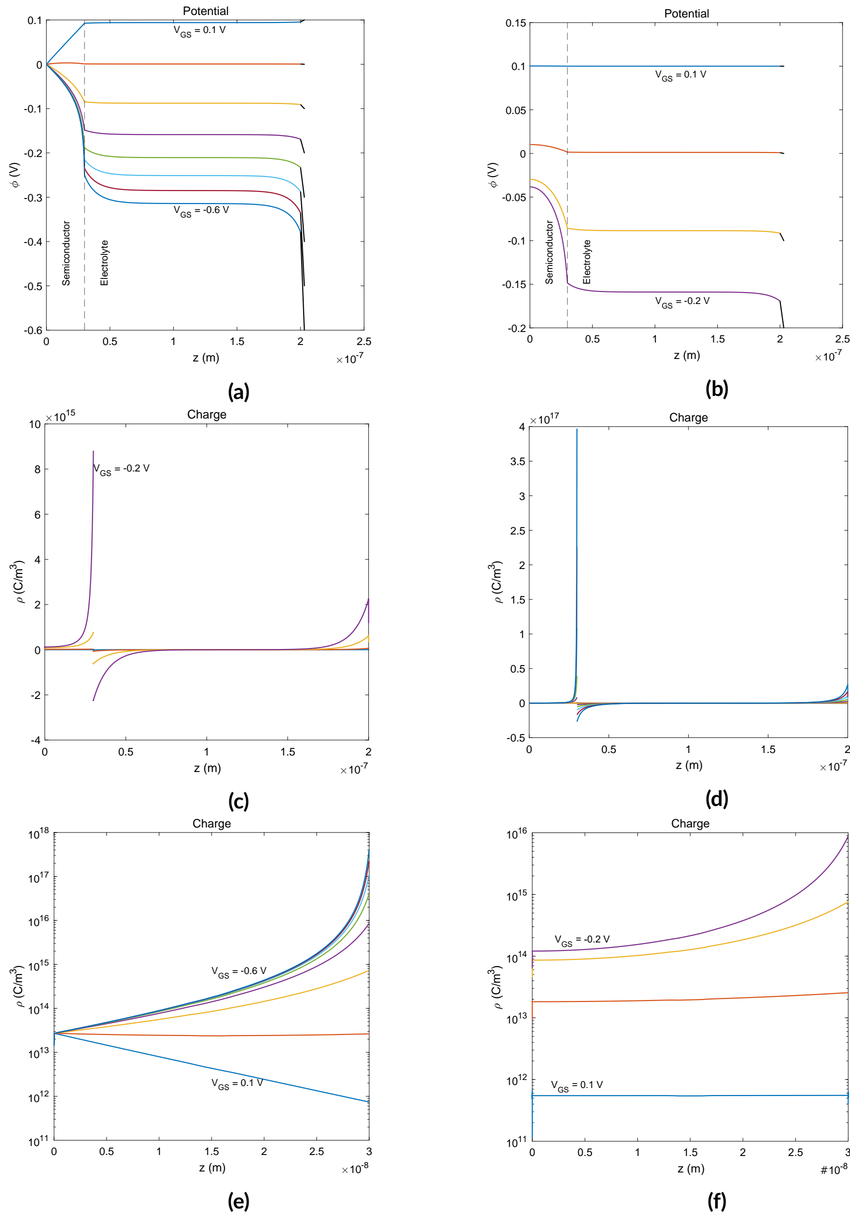

Figure 4.1: (a - b) Electrical potential and (c - d) charge carrier density above the electrode. The distribution in the semiconductor is displayed for $0\,\text{nm} < z < 30\,\text{nm}$ and for the electrolyte for $30\,\text{nm} < z < 200\,\text{nm}$. The black lines at $z = 200\,\text{nm}$ visualize the linear voltage drop caused by the distributed capacitance of the Stern layer. The charge carrier distribution demonstrates the strong amplification character of an EGOFET. (e - f) show the charge accumulated in the semiconductor on a logarithmic scale. Here, the absence of accumulated charges for $V_{GS} > 0\,\text{V}$ is seen. Parameters of the calculation in Table 4.1, with the change of $h_{\text{elec}} = 170\,\text{nm}$.

4.2 Ionic Diffusive Effects on the Sheet Semiconductor Conductivity

We have seen in Chapter 3 that the sheet semiconductor conductivity at zero source-drain voltages $\sigma_{\text{sheet},0}$ contains valuable information for understanding the physics of EGOFETs. Here, we have analyzed this magnitude with the one-dimensional model for both the electrodes (MES structure with a bottom metal) and the channel (MES structure with a bottom insulator). Figure 4.2 (continuous lines) displays the conductivity of the semiconductor film over the channel for $V_{\text{DS}} = 0\,\text{V}$ as a function of the source gate voltage V_{GS} for both one-dimensional models. The sheet conductivity obtained with the 2D Helmholtz model for $V_{\text{DS}} = 0\,\text{V}$ and 10 μm length is displayed, where the presence of diffusive effects is neglected. The prediction in the NPP shows a lower conductivity, resulting from the ionic diffusive effects. The three regimes of the output characteristics (see Chapter 1) are reflected in the conductivity, namely weak, moderate and strong accumulation regimes. The weak accumulation is due to the depletion of holes in the semiconductor film, where the conductivity shows an exponential dependence on the gate voltage. The transition from weak to the moderate regime is marked by a critical voltage V_{c}. The conductivity depends almost linearly on the source-gate voltage in the strong accumulation regime. However, a true linear dependency is not attained in the NPP model in the usual operational range of voltages (up to $-1\,\text{V}$), as discussed in the following subsection. The sub-threshold regime, instead, is the same in the NPP and Helmholtz models, confirming that ionic diffusive effects do not play any role in this regime.

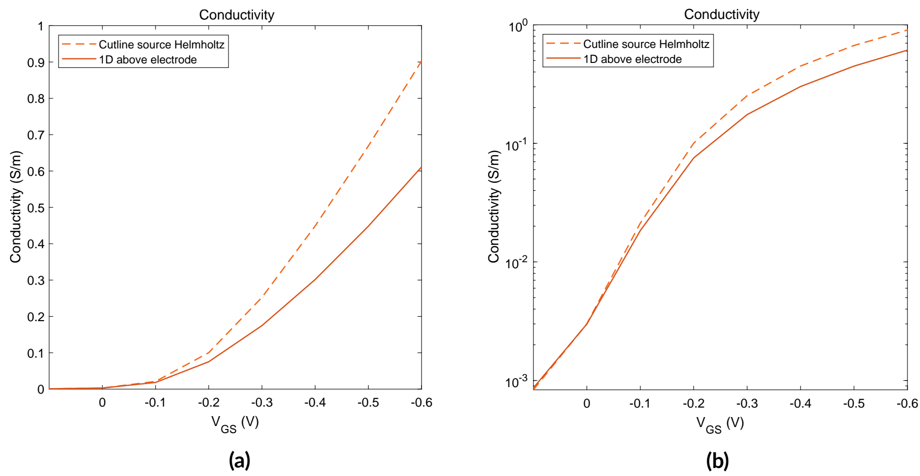

Figure 4.2: The conductivity in the NPP framework for an ion concentration of $1mM$ as a function of the gate voltage shows a lower conductivity than the one predicted by the Helmholtz model in (a) linear and (b) logarithmic scale. The conductivity curves match the analytical solution [57]. Parameters of the calculation are in Table 4.1 and 3.1 for the 1D NPP and the 2D Helmholtz models, respectively.

4.3 Threshold Voltage Dependency on the Source-Gate Voltage

To evaluate the linearity of the capacitance versus source-gate voltage curve, we analyzed the tangent line to this function, where the slope of the tangent reflects the phenomenological capacitance c_{EDL} and its intercept reflects the threshold voltage, V_{th}. Usually, the phenomenological capacitance c_{EDL} is calculated from the tangents of the conductivity at $V_{\mathrm{DS}} = 0\,\mathrm{V}$ and the tangent's intercept at the threshold voltage V_{th} (see Chapter 1.2.3). However, this is based on the assumption that the transfer curve, and therefore the conductivity curve, assumes a linear behavior for high enough negative gate voltages. As we show in this chapter, this is only an assumption that does not reflect the actual EGOFET behavior when the diffusive effects are considered. Figure 4.3 gives the tangent lines to the conductivity predicted by (a) the Helmholtz and (b) the NPP model at different gate voltages. The red crosses correspond to the intercepts.

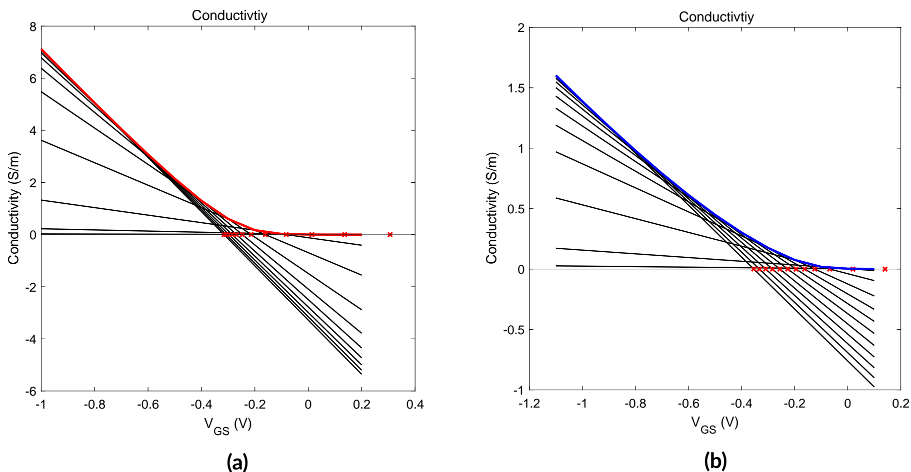

Figure 4.3: Sheet semiconductor conductivity predicted by the 1D MES model with the tangent and the intercept as the threshold voltage of the EGOFET in the (a) Helmholtz model and the (b) one-dimensional NPP model.

Figure 4.4 shows the dependency of c_{EDL} (slope) and V_{th} (intercept) on the source-gate voltage. An accurate linear behavior only exists when both become

independent from the applied gate voltage. In the case of the Helmholtz model (red lines) for moderately negative gate voltages (roughly below ≈ -0.5 V here), the capacitance and threshold voltage vs. gate-voltage approach asymptotically to approximately constant values $c^{\mathrm{H}}_{\mathrm{EDL}}$ and $V^{\mathrm{H}}_{\mathrm{th}}$, which allow defining a linear dependency of the form

$$\sigma^{\mathrm{H}} \approx c^{\mathrm{H}}_{\mathrm{DL}}(-V_{\mathrm{GS}} + V^{\mathrm{H}}_{\mathrm{th}}t), \tag{4.1}$$

characteristic for FET devices. In Huetter et al. [57] analytical expressions for these asymptotic values were given, plotted as horizontal dashed lines in Figure 4.4.

However, we cannot find this asymptotic behavior for the NPP model inside the common operational voltages of EGOFETs. Therefore, a true linear behavior is not reached, reflecting the corresponding current-voltage characteristics (see following chapters). This result shows that the interpretation of the characteristics of EGOFET devices utilizing ideal models may fail when ionic diffusive effects play a significant role (low ionic concentrations or high interfacial capacitances) [63].

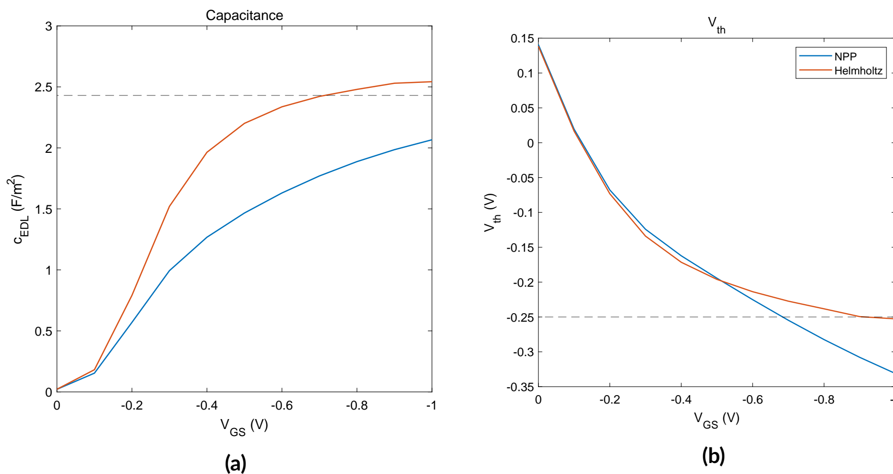

Figure 4.4: (a) Capacitance and (b) threshold voltage dependency on the applied gate voltage. The dashed horizontal lines represent the asymptotic Helmholtz values.

4.4 Effect of the Interfacial Layers on the Semiconductor Conductivity

In the previous chapters, we discussed how the sheet conductivity provides the main information about the phenomenological device parameters. This section will show how the conductivity of an EGOFET gets influenced, primarily when used as a biosensor. EGOFETs are used as biosensors to transform biological signals into electrical signals. One example of an application is detecting multiple sclerosis [64]. The presence of the disease is detected by biomarkers, most often specific proteins such as antigens, peptides, and enzymes [65–70]. Antigens bind to their specific antibodies once they are in close contact. Due to its architecture and strong capacitive coupling [25], an EGOFET provides high sensitivity to these small capacity changes at the biorecognition event.

In a biosensor, the antibodies are attached to the electrode's surface, the so-called functionalization of the gate (see Figure 4.5). When the electrolyte contains the specific antigens, the antigens bind to the antibodies. The additional molecule attached to the surface modifies the interfacial layer. As discussed in Chapter 1.2.2, the equivalent capacitance describing the interfacial layer changes is reflected in the measured source-drain current Id. The modeling of the physics of antibody/antigen layers can be complex since they can extend several nanometers and can include the presence of moving ions (conductivity) and bulk and surface charges [15]. For simplicity, we will consider a simpler model system based on self-assembled monolayers, whose description can be made employing the simple interfacial layers considered in this thesis work.

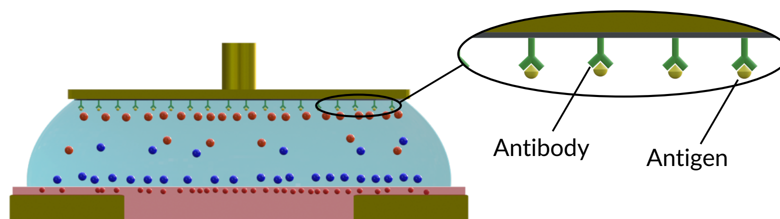

Figure 4.5: EGOFET as a biosensor. The gate electrode (gold) is functionalized by attaching antibodies to the interface. When antigens are present in the electrolyte/analyte, they bind to the specific antibodies.

4.4.1 Self-Assembled Monolayer Interfacial Layers

Usually, when EGOFETs are functionalized with self-assembled-monolayers (SAMs) [32], the functionalization can be made on the gate electrode to take advantage of the chemistry of metallic materials, usually gold. The SAM molecules can react with the electrode material (e.g., gold) by using thiol-ended groups. This way, one forms a layer that consists of one-molecular thickness, the so-called self-assembled monolayer. The SAMs form an interfacial layer at the gate electrode, influencing the conductivity. In Figure 4.6(a), molecules with different carbon lengths and corresponding capacitance illustrate different possible configurations. The parallel plate expression can approximate the specific capacitance of the SAM layer as

$$c_{\text{SAM}} = \frac{\varepsilon_0 \varepsilon_{\text{SAM}}}{d_{\text{SAM}}} \tag{4.2}$$

where the dielectric constant is typically $\varepsilon_{\text{SAM}} = 2$ and the thickness d_{SAM}, obtained with the CULGI Simcenter software for molecular modeling. Figure 4.6 shows the interfacial capacitance values predicted by Equation (4.2). In this section, we discuss the influence of SAMs of different lengths on the EGOFETs conductivity by using the one-dimensional model.

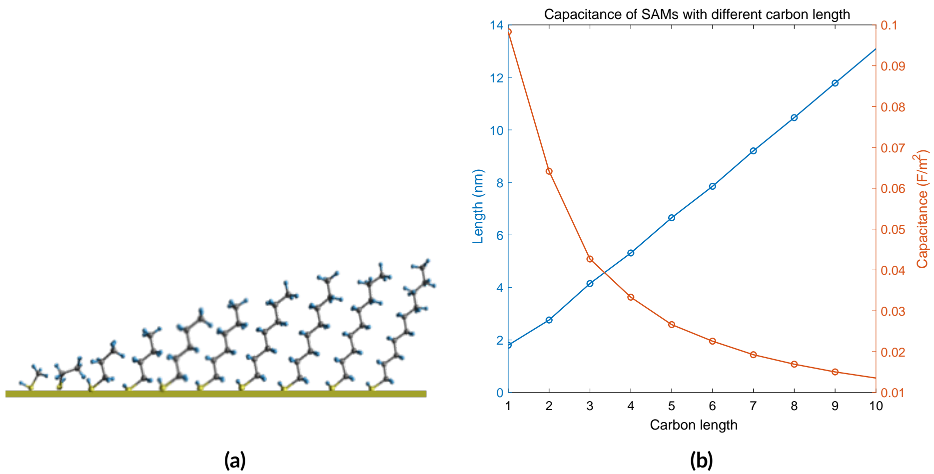

Figure 4.6: (a) Molecules with an increasing number of carbons. Attached to the gold electrode, they form a self-assembled monolayer. When treated as a compact layer, the capacitance can be calculated with a parallel plate capacitor formula. (b) The capacitance corresponds to the different carbon lengths.

Figure 4.7 portrays the changes in the sheet semiconductor conductivity predicted by the one-dimensional NPP model on the source of the channel. When having different SAMs of one, three, seven, and ten carbon lengths attached to the gate electrode (as shown in Figure 4.6 (b), the interfacial layer becomes thicker, so the lower the distributed capacitance. The SAMs are calculated as capacitors in series at the gate electrode. The data are plotted in linear and logarithmic scales (see Figure 4.7). The conductivity in Figure 4.7 (b) shows that all curves overlap in the low accumulation regime. Hence, adding a capacitive layer absorbs small voltage in this voltage range. Figure 4.8 (a) shows that instead, in the strong accumulation regime (negative voltages) significant variations occur, with thicker interfacial layers, implying lower conductivities and smaller slopes (phenomenological capacitance). Figure 4.8 (a) shows the capacitance calculated as

$$c_{\text{elec}} = \frac{\partial q_{\text{elec}}}{\partial V_{\text{GS}}} \quad \text{with} \quad q_{\text{elec}} = \varepsilon_0 \varepsilon_{\text{r,elec}} \frac{\partial \phi_{\text{elec}}}{\partial y}. \tag{4.3}$$

It is observed that for high interfacial capacitance values, an asymptotic constant value is not reached. However, for the low interfacial capacitances, it does, meaning that in those cases, a linear dependency can be defined and that the

Helmholtz approximation is a good approximation. The low capacitance value depends on the geometric capacitance of the semiconductor and the interfacial capacitance. It does not involve the contribution of any space charge layer, which is not present in this voltage range [57].

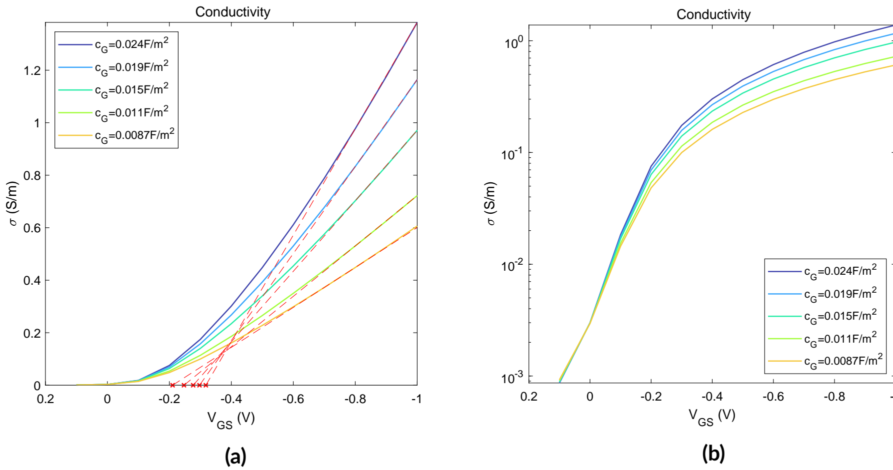

Figure 4.7: Conductivity changes on (a) linear and (b) logarithmic scales for different carbon lengths of the self-assembled monolayers. The tangent to the conductivity lines at high negative voltage gives the capacitance and intercepts the threshold voltage (red crosses).

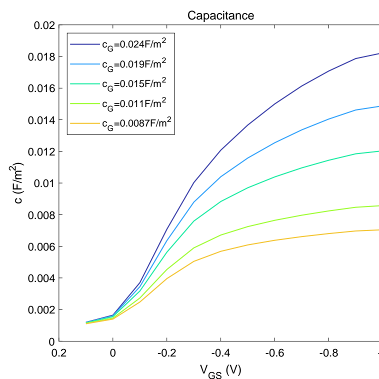

Figure 4.8: Electrolyte capacitance for different thicknesses of interfacial layers referring to a SAM layer of 1,3,7 and 10 carbon length. The interfacial capacitance $c_G = 0.0243\,\mathrm{F/m^2}$ refers to the Stern layer.

We can also analyze the effect of modifying the interfacial capacitance in the voltage distribution. As expected, the voltage drop at the interfacial layer becomes significant (see Figure 4.9 black lines) with lower interfacial capacitances.

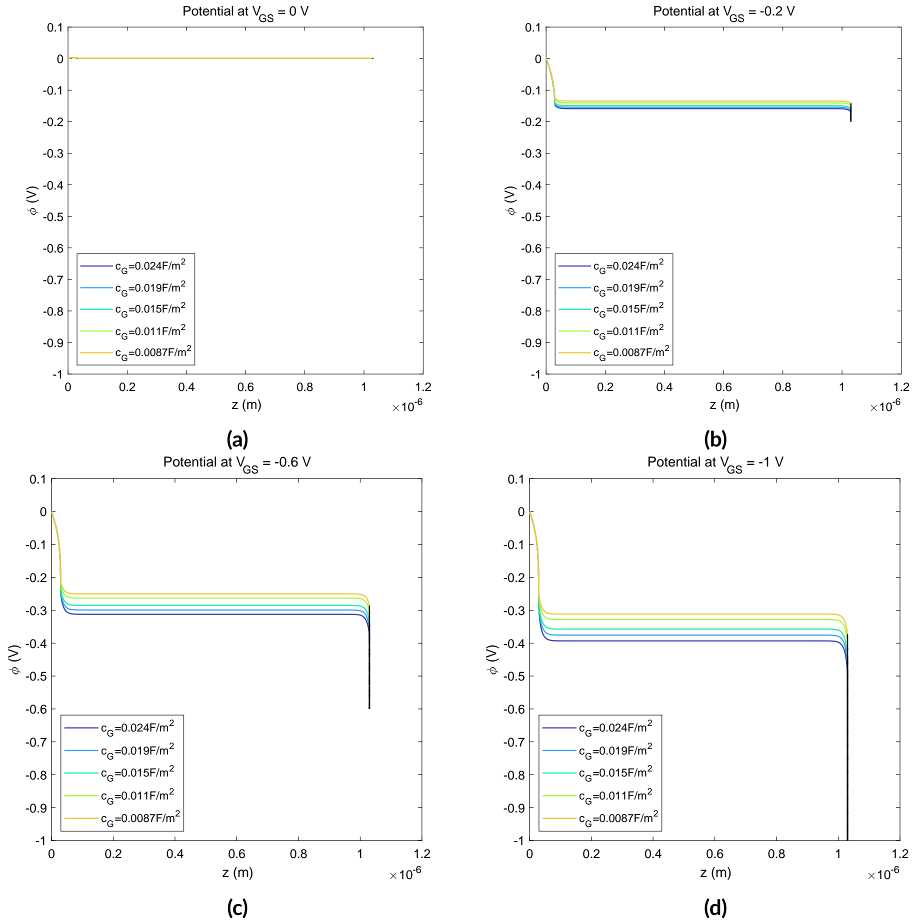

Figure 4.9: Potential along the one-dimensional EGOFET cutline above the source electrode. Between $z = 0$ nm and $z = 30$ nm, it shows the potential of the semiconductor. Between $z = 30$ nm and $z = 1030$ nm, the potential in the electrolyte is seen with the long flat potential in the bulk electrolyte. The voltage distributions are given for (a) $V_{GS} = 0$ V, (b) $V_{GS} = -0.2$ V, (c) $V_{GS} = -0.6$ V, and (d) $V_{GS} = -1$ V. Parameters are given in Table 4.1.

4.4.2 Localization of the Distributed Interfacial Capacitances

The biorecognition layer can be placed at the gate electrode and/or on the semiconductor. To analyze the effects of the different locations, we reproduced the experiments of the last section with the capacitances of the SAM and an additional capacitance at the electrolyte/semiconductor film. In a second study, we changed the location of the different SAMs to the semiconductor/electrolyte interface. The voltage drop caused by the interfacial capacitance is given by Equation (1.3), whereas the location between the functionalization of the gate and the semiconductor is indifferent to the conductivity behavior (see Appendix C). However, the bulk potential is influenced because the significant voltage drop is either at the gate electrode (see Figure 4.10, black line) or at the interface to the semiconductor (red line). It can be advantageous to functionalize one or the other in an actual biosensor, depending on the surface properties and the possible reactions of molecules and electrode/semiconductor materials. Although the potential distribution in the semiconductor is the same in both cases for $V_{DS} = 0\,\mathrm{V}$, in a non-uniform regime, there might be a difference. This needs to be analyzed with a two-dimensional model, as the one-dimensional structures are only valid for $V_{DS} = 0\,\mathrm{V}$.

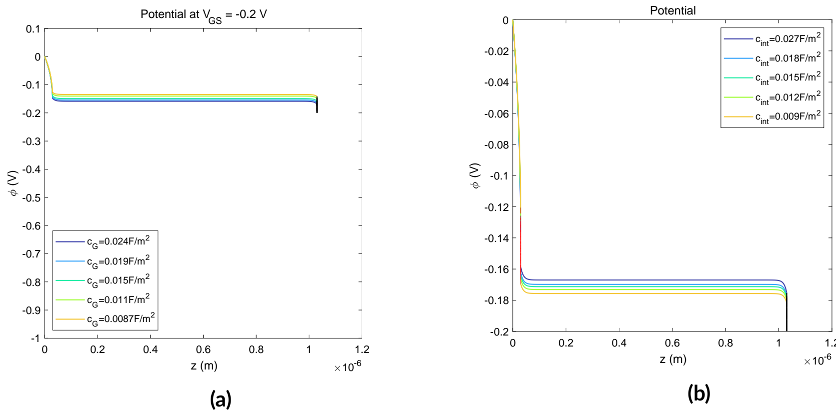

Figure 4.10: (a) Potential above the electrode for first case when the interfacial capacitance $c_{\mathrm{int}} = 0.243\,\mathrm{F/m2}$ and (b) the SAMs are on the gate electrode and for second case when the SAMs are placed on the semiconductor, and the interfacial capacitance on the gate is held constant at $c_G = 0.243\,\mathrm{F/m^2}$.

4.4.3 Influence of Fixed Charges at the Gate Electrode Functionalization Layer

When EGOFET biosensors detect biomarkers, specific antigens are attached to the gate electrode functionalization layer. These biomarkers have a certain thickness and charge. In the previous section, we investigated the influence of the thickness, which corresponds to different gate distributed capacitances c_G, without any fixed charges. This section investigates the influence of fixed charges at the gate electrode q_G. In Figure 4.11, the conductivity over the gate voltage is plotted with the tangent at $V_{GS} = -0.8$ V. The conductivity curves are shifted over the voltage ΔV_{GS} by following the relation

$$\Delta \mathrm{V_G} = \frac{q_G}{c_G} \tag{4.4}$$

as it is apparent from the boundary condition in . The fixed charges at the gate electrode then act like an applied gate voltage shift, through which the conductivity curves are shifted accordingly (and hence also the threshold voltage is shifted, red dashed line Figure 4.11 (a). Here, the red dashed lines are the tangents at the transfer curve at $V_{GS} = -0.8$ V.

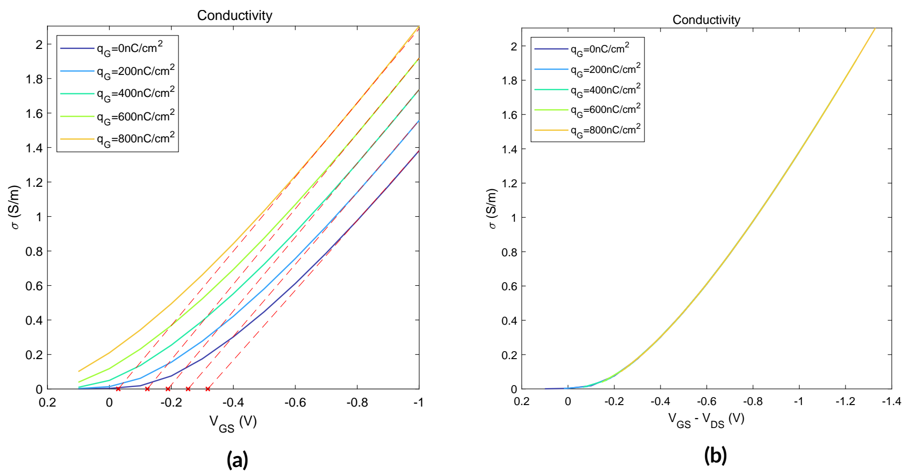

Figure 4.11: (a) Conductivity over gate voltage for different fixed charges q_G. (b) The conductivity curves are shifted according to Equation (4.4).

The capacitances are accordingly shifted as the conductivity curves (see Figure 4.12). The endpoints at $V_{GS} = 0.1\,\mathrm{V}$ and $V_{GS} = -1\,\mathrm{V}$ seem to not follow exactly this trend. However, this might be due to the numerical differential method, which becomes less exact at the borders.

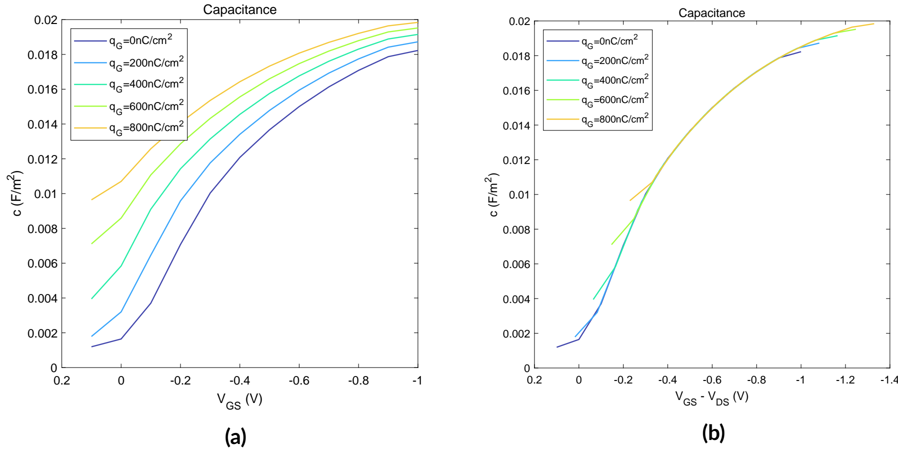

Figure 4.12: (a) Electrolyte capacitance for different fixed charges q_G. (b) The capacitance is mainly shifted according to Equation (4.4). Parameters are given in Table 4.1.

In the voltage distribution (see Figure 4.13), the shift of the bulk potential is seen for (a) $V_{GS} = 0\,\mathrm{V}$, (b) $V_{GS} = -0.2\,\mathrm{V}$, (c) $V_{GS} = -0.6\,\mathrm{V}$, and (d) $V_{GS} = -1\,\mathrm{V}$. The influence of the fixed charges on the bulk potential is higher for lower V_{GS}. For higher V_{GS}, the voltage drop at the interfacial layer becomes large, whereas the influence of the fixed charges has less impact.

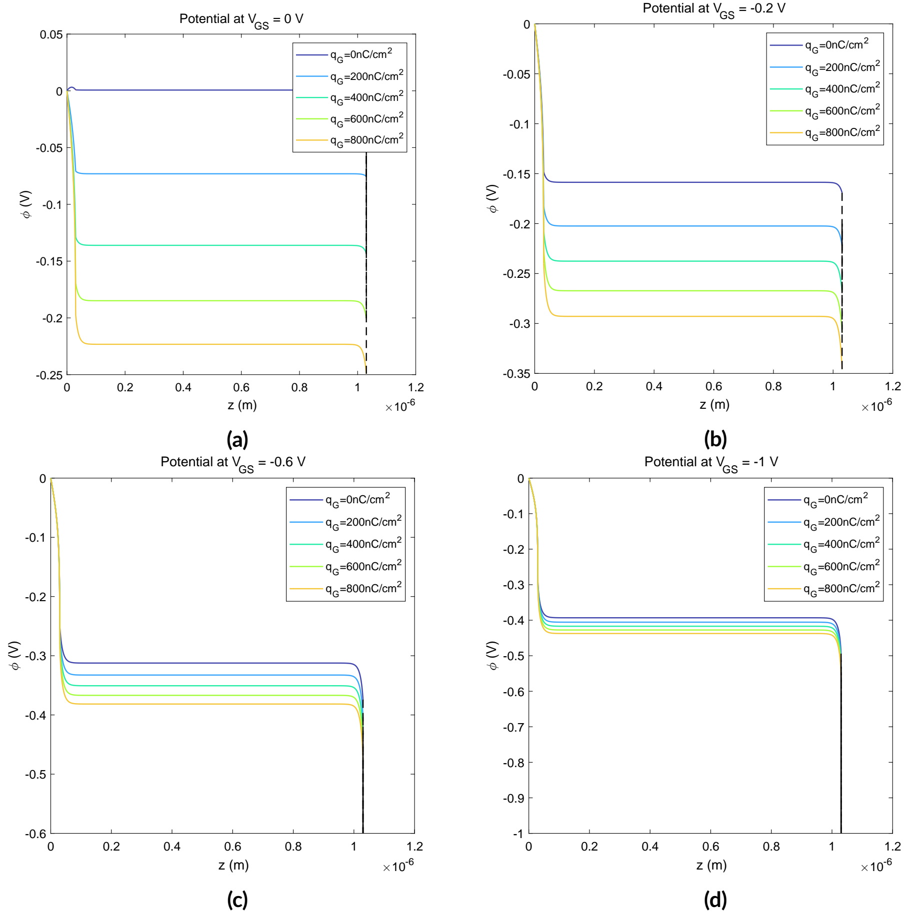

Figure 4.13: Potential distribution above the source electrode for (a) $V_{GS} = 0\,$V, (b) $V_{GS} = -0.2\,$V, (c) $V_{GS} = -0.6\,$V, and (d) $V_{GS} = -1\,$V. The potential in the semiconductor is plotted between $z = [0, 30]$ nm and in the electrolyte for $z = [30, 1030]$ nm. The black line at $z = 1030\,$nm mimics the voltage drop at the interfacial layer. Parameters are given in Table 4.1.

4.5 Influence of the Ionic Strength of the Electrolyte

In EGOFETs, the electrolyte's ionic strength is an important parameter to analyze since the application type can broadly vary. For sensing applications with a biorecognition layer, the ionic strength can be bound to a specific pH-value or a particular distribution of ions, e.g., when a sweat sensor is used [71]. The ionic strength influences the EGOFETs characteristic and reaches a maximum for high ionic concentrations [47]. Figure 4.14 shows the conductivity over the gate voltage for different ionic strengths. The one-dimensional model becomes numerically unstable for high ionic strength, whereas not the entire voltage range is given for each concentration. For high ionic strength, the conductivity curve approaches the characteristics of the Helmholtz model, in which the ionic diffusive effects become negligible due to the extremely high ionic diffusive capacitances.

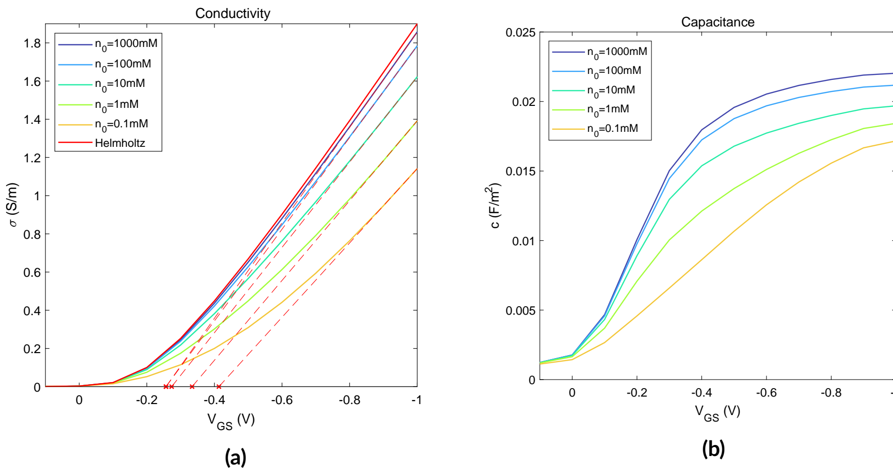

Figure 4.14: Conductivity and capacitance changes for different ion concentrations predicted by the 1D NPP model. Parameters are given in Table 4.1, with the change of lengt $h_{\mathrm{elec}} = 10000\,\mathrm{nm}$, to calculate with very low concentrations.

Figure 4.15 shows the potential distribution for different ionic strengths at $V_{\mathrm{GS}} = [0, -0.2, -0.6]$ V. The voltage drop in the electrolyte is higher for lower ion concentrations. In very high concentrations, the voltage drop on the electrolyte is

negligible. The NPP framework approaches the Helmholtz model, if we treat the electrolyte as a distributed capacitance.

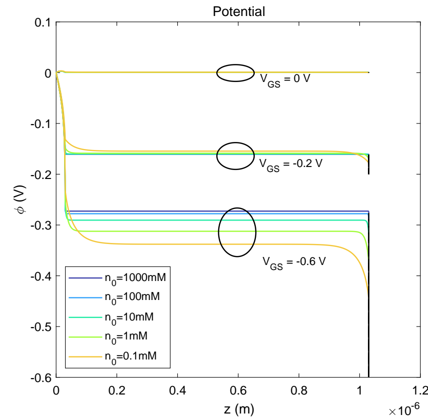

Figure 4.15: Potential distribution for different ionic strengths. The voltage drop in the electrolyte is higher for lower ion concentrations, which shifts the electrolyte's bulk potential. Parameters are given in Table 4.1.

4.6 Summary

- In this Chapter, we analyzed one-dimensional metal/semiconductor/electrolyte one-dimensional structures in the NPP framework to gain insight into the physics of EGOFETs.
- We discuss how the ionic diffusive effects limit the conductivity by comparing the Nernst-Planck-Poisson model with the Helmholtz model.
- We reveal the dependency of the threshold voltage on the source-gate voltage. For high negative voltages, the Helmholtz model tends to exhibit linear behavior. When including ionic diffusive effects, the actual behavior in the typical operational voltage window of EGOFET devices is not linear.
- We examine the role of interfacial layers in the conductivity and capacitance changes for different self-assembled monolayers.
- We show the threshold voltage shift induced by fixed charges at the gate electrode.
- We investigate the effects of the ionic strength, which converges to the Helmholtz model for high ionic strength. The high ionic strength diffusive effects become negligible due to the extremely high ionic diffusive capacitances.

Chapter 5

EGOFET two-dimensional model in the NPP framework

In Chapter 3, we analyzed the physics and current-voltage characteristics of EGOFETs in the two-dimensional Helmholtz model. In Chapter 4, we incorporated the diffusive effects of the electrolyte in one-dimensional models using the Nernst-Planck-Poisson (NPP) framework. In this chapter, we present the two-dimensional NPP model for an EGOFET, including the presence of interfacial layers and fixed charges. We will demonstrate the nanoscale's voltage and charge carrier distributions in the devices and explain how the macroscale current-voltage characteristics match the real-life EGOFET behavior.

We compare potential profiles over the source, channel, and drain obtained with the two-dimensional model and compare them with those predicted by the one-dimensional model for $V_{DS} = 0$ V. The previous chapter showed the influence of ion concentrations, distributed capacitances, and fixed charges. Some parameters, like the gate and channel length, require a two-dimensional model for their analysis, as these are not reflected in the one-dimensional model. In Section 5.6, we address the influence of these geometric parameters.

5.1 Current-voltage characteristics

As mentioned in Chapter 1, EGOFETs are experimentally characterized through the measurement of their transfer and output current-voltage (I-V) characteristics and, in the case of a biosensor, they are evaluated for changes associated with the biosensing process. In the present subsection, we present the predictions for the I-V characteristics of an EGOFET in the 2D NPP theoretical framework. If not otherwise stated, the parameters in Table 5.1 have been used.

Table 5.1: Parameters used in the 2D EGOFET simulations in the NPP framework used in this chapter if not otherwise stated.

Parameter	**Value**
Carrier concentration n_h	$6 \times 10^{21}\,1/\mathrm{m}^3$
Carrier mobility μ_{sem}	$1.3 \times 10^{-4}\,\mathrm{m}^2/(\mathrm{Vs})$
Ion concentration n_0	$1\,\mathrm{mM}$
Ion mobility μ_{elec}	$1.5 \times 10^{-6}\,\mathrm{m}^2/(\mathrm{Vs})$
Semiconductor thickness h_{sem}	$30\,\mathrm{nm}$
Electrolyte thickness h_{elec}	$1\,\mu\mathrm{m}$
Electrode length $l_{electrode}$	$1\,\mu\mathrm{m}$
Relative permittivity semiconductor $\varepsilon_{r,sem}$	4
Relative permittivity electrolyte $\varepsilon_{r,elec}$	78
Channel length $l_{channel}$	$3\,\mu\mathrm{m}$
Width to length W/L ratio	167
Gate distributed capacitance c_G	$0.0243\,\mathrm{F}/\mathrm{m}^2$

Figure 5.1 shows the (a) output and (b) transfer current-voltage characteristics of an EGOFET predicted by the two-dimensional NPP model for the parameters listed in Table 5.1. Figure 5.1 (a) shows the transfer curves in log-linear scale, while Figure 5.1 (b) shows the square root of the source-drain current as a function of the source gate voltage for $V_{DS} = -0.7\,\mathrm{V}$ (saturation regime). The NPP model predicts current-voltage characteristics for EGOFET typical of FET devices (see Chapter 1), with sub-threshold (exponential), "linear", and saturation regimes. Even though neither the linear regime is fully linear nor the saturation does appear saturated, we can obtain approximate phenomenological parameters from the current-voltage characteristics by using the ideal FET model given in Equation (1.7). For instance, from the sub-threshold regime, we can obtain the sub-threshold slope

voltage V_{SS} and the subthreshold capacitance c_0, assuming μ_{sem} is known and equal to the simulation parameter, giving $V_{SS} = 0.028\,\mathrm{V}$ and $c_0 = 0.19\,\mu\mathrm{F/cm^2}$.

Moreover, by plotting the current's square root in the saturation regime (see Figure 5.2, b), we can obtain the threshold voltage $V_{th} = -0.053\,\mathrm{V}$. Finally, we can obtain the device capacitance $c_{DL} = 1.1\,\mu\mathrm{F/cm^2}$ from the slope of the transfer curve in the saturation regime (see Figure 5.2, b). However, these parameters can vary depending on the exact position from where they are extracted.

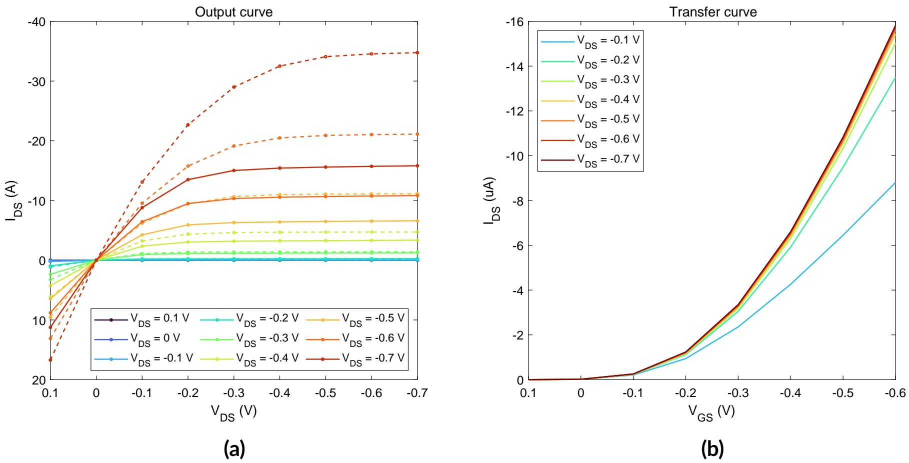

Figure 5.1: Current-voltage characteristics of an EGOFET with the parameters given in Table 5.1. The current is calculated with a $W/L = 167$. As the simulation has two dimensions, the system's depth is just a factor applied to the end result of the simulated two-dimensional sheet.

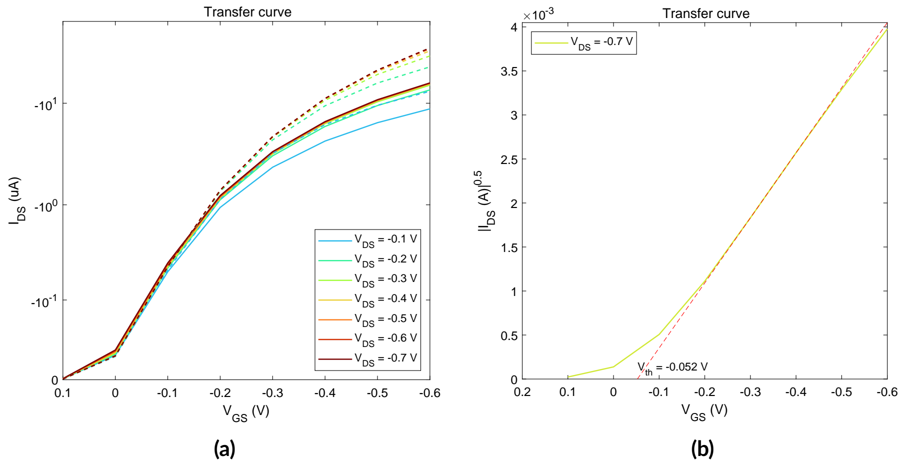

Figure 5.2: (a) Transfer curve in log-scale and (b) the transfer curve in saturation plotted in the square root to visualize the linear behavior at higher voltages. (c) From the transfer curve in the linear regime, the double layer capacity C_{DL} can be extracted.

For comparison, in Figure 5.1 and 5.2 (a), we have also plotted the predictions of the Helmholtz model for this device (dashed lines) to evaluate the effects of the ionic diffusive effects in the current-voltage characteristics. The presence of ionic diffusive effects is seen to reduce the current levels considerably, in agreement with the results obtained with the 1D NPP model, where it was observed that the sheet semiconductor conductivity was smaller in the NPP model as compared to the Helmholtz model due to the voltage drops in the ionic diffusive layers. Here, the current level reduction looks even more relevant, which could indicate an additional reduction effect associated with the non-uniform ionic distribution along the channel surface when there is a source-drain current flowing in the device. Further research is necessary to clarify this aspect.

5.2 Electric Potential Distribution

Figure 5.3 (a) and (b) show the electric potential distribution along the transversal cutline in the center of the source electrode and channel for $V_{\mathrm{DS}} = 0\,\mathrm{V}$ (red continuous lines). For $V_{\mathrm{DS}} = 0\,\mathrm{V}$, the voltage distribution above the drain is the same as on the source. The position of the cutlines is shown in the potential distribution in Figure 5.3 (b). The electric potential distributions followed the predictions of the 1D model analyzed and discussed in Section 4.1 (small symbols), further validating the two-dimensional model implementation. We refer to that subsection for a discussion on the main features of these transversal profiles.

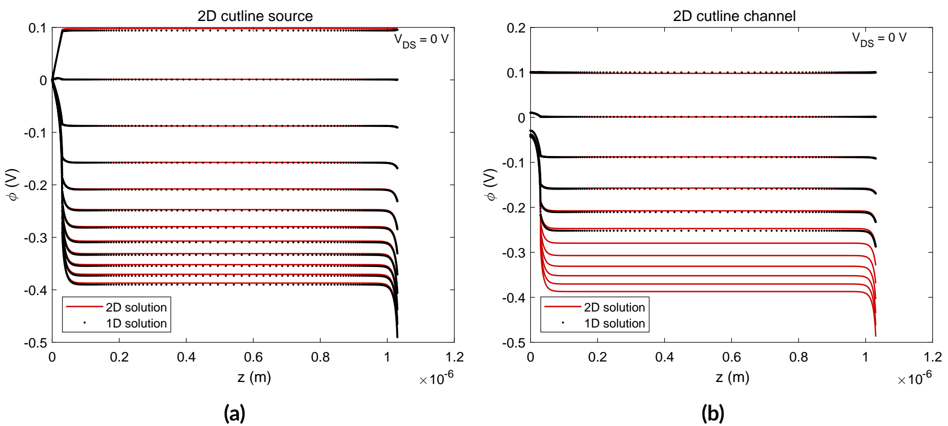

Figure 5.3: Potential distribution for $V_{\mathrm{DS}} = 0\,\mathrm{V}$ and $V_{\mathrm{GS}} = [0.1, -1]\,\mathrm{V}$ with a step size of $\Delta V = -0.1\,\mathrm{V}$ on (a) the source electrode and (b) the middle of the channel. The continuous lines refer to the two-dimensional and the symbols one-dimensional NPP models. The two-dimensional model matches the one-dimensional model over the source electrode and the channel. Parameters are given in Table 5.1.

The two-dimensional potential distribution in the whole device (semiconductor and electrolyte) is visualized for $V_{\mathrm{DS}} = [0, -0.2, -0.6]\,\mathrm{V}$ and $V_{\mathrm{GS}} = -0.2\,\mathrm{V}$ in Figure 5.4. The voltage drop in the transversal direction in the semiconductor is high, whereas in the electrolyte is relatively small, having a long, constant potential with the formation of the EDL at the interfaces to the gate electrode and the semiconductor, as already seen in Figure 5.3.

The color map (a) shows the potential distribution in the semiconductor cross-section with cutlines at $z = [1, 14, 29]$ nm. The two-dimensional electric potential distribution in the semiconductor film is shown in Figure 5.4 (c), while (c) shows the potential profiles along the horizontal direction taken at the bottom (green), middle (red), and the surface (blue) of the semiconductor film. Close to the electrodes ($z = 1$ nm), the potential distribution is non-uniform due to the before-mentioned contact with the electrodes. Close to the electrolyte interface ($z = 29$ nm), the potential is uniform in a horizontal direction. The potential on top of the electrodes and the channel is nearly constant. However, the values differ except close to the electrolyte/semiconductor interface. The potential drop along the vertical direction is different on the electrodes and the channel since the semiconductor is in contact with the electrode metal and the channel with an insulating substrate. This fact can also be seen from the transversal profiles in Figure 5.4. For $V_{DS} = 0$ V, the horizontal potential distribution is symmetrical.

As soon as a drain voltage is applied, the voltage distribution is no longer uniform and symmetric along the channel, and a current between source and drain starts flowing. The potential drop along the semiconductor from source to drain is non-linear, meaning that the electric field is not uniform along the semiconductor channel (space charge limited transport). The transversal voltage drop on the source, channel, and drain are now different.

We note that close to the semiconductor surface ($z = 29$ nm) at the interface with the electrolyte, the potential distribution appears non-uniform. In the bulk electrolyte, the potential distributions appear relatively uniform in the longitudinal direction and with the formation of space charge diffusive layers at the gate and semiconductor interfaces.

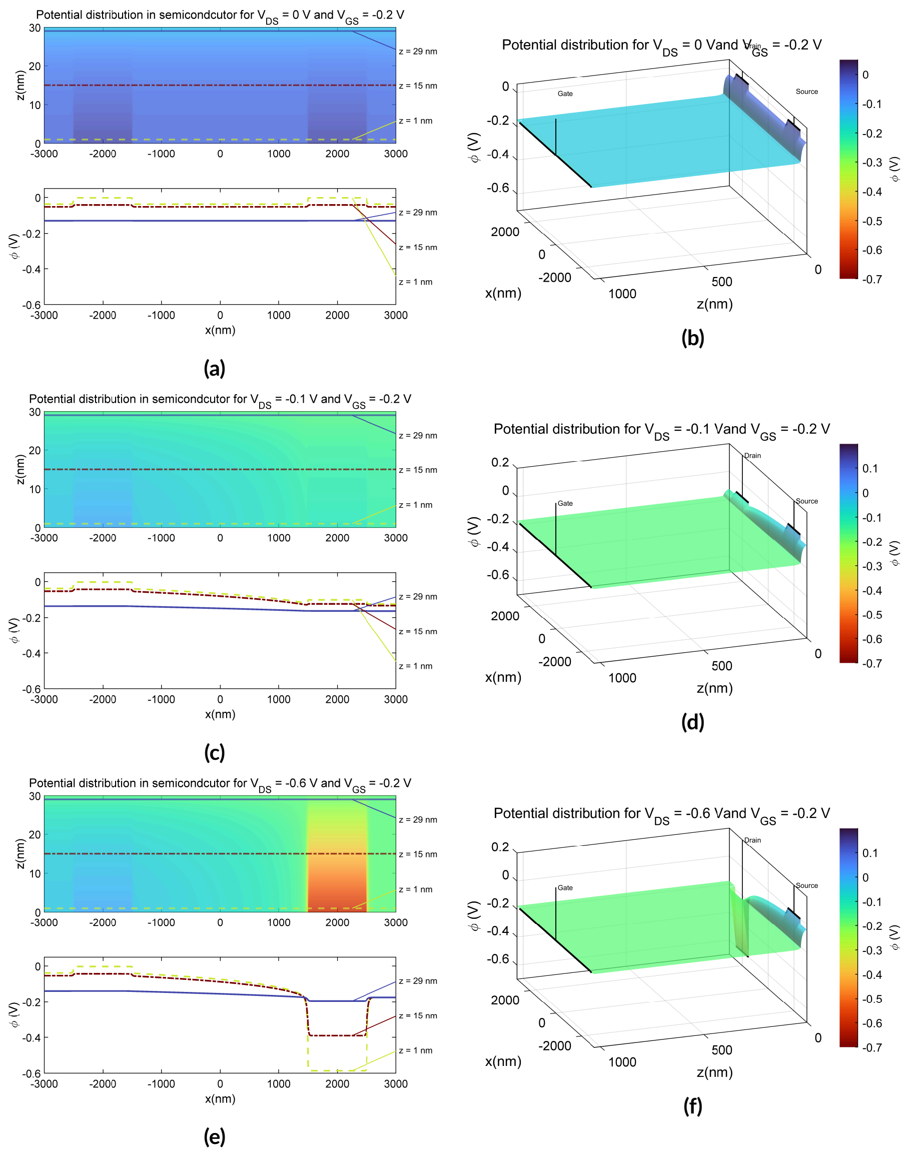

Figure 5.4: Potential distribution of the 2D model for $V_{GS} = -0.2$ V and (a-b) $V_{DS} = 0$ V, (c-d) $V_{DS} = -0.1$ V and (e-f) $V_{DS} = -0.6$ V. (a,c,e) visualize the potential distribution in the semicondcutor. The cutlines at $z = [1, 15, 29]$ nm are plotted. (b, d, f) show the potential ϕ over the semiconductor $z = [0, 30]$ nm and the electrolyte $z = [30, 1030]$ nm. Parameters are given in Table 5.1.

5.3 Free Carriers Concentration Distribution

When a gate voltage is applied, the semiconductor's free charge carriers (holes) get attracted to the interface with the electrolyte. Figure 5.5 shows the charge accumulation for the cutline above the drain (a) and in the middle of the channel (b) for $V_{\mathrm{DS}} = 0\,\mathrm{V}$. The 2D simulation matches the one-dimensional simulation again. For low (and positive) gate voltages, where no holes accumulate at the interface, the semiconductor behaves like an insulator or dielectric since the hole density becomes very small inside the semiconductor film (see insets in Figure 5.5).

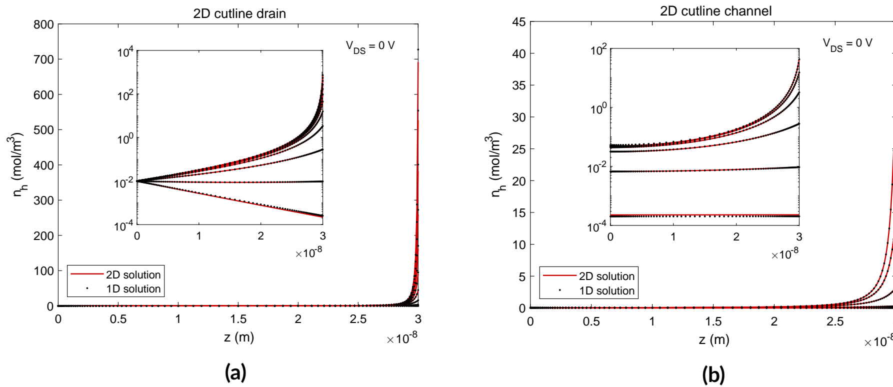

Figure 5.5: Hole concentration distribution in the semiconductor for $V_{\mathrm{DS}} = 0\,\mathrm{V}$ and $V_{\mathrm{GS}} = [0.1 to - 1]\,\mathrm{V}$ at the electrode and $V_{\mathrm{DS}} = 0\,\mathrm{V}$ and $V_{\mathrm{GS}} = [0.1 to - 0.4]\,\mathrm{V}$ at the channel. Parameters are given in Table 5.1.

The ions in the electrolyte migrate due to the presence of an electric field, like the holes in the semiconductor, with the difference that they cannot leave or enter the electrolyte. For negative gate voltages, the positive ions get attracted to the negative gate electrode at $z = 1030\,\mathrm{nm}$ (see Figure 5.6,a + b), and therefore, the negative ions accumulate at the interface with the semiconductor at $z = 30\,\mathrm{nm}$ (see Figure 5.6, c + d). The higher the gate potential gets, the stronger the accumulation of ions. The distribution over the source electrode and the channel is different. The agreement with the one-dimensional solution is excellent (black points).

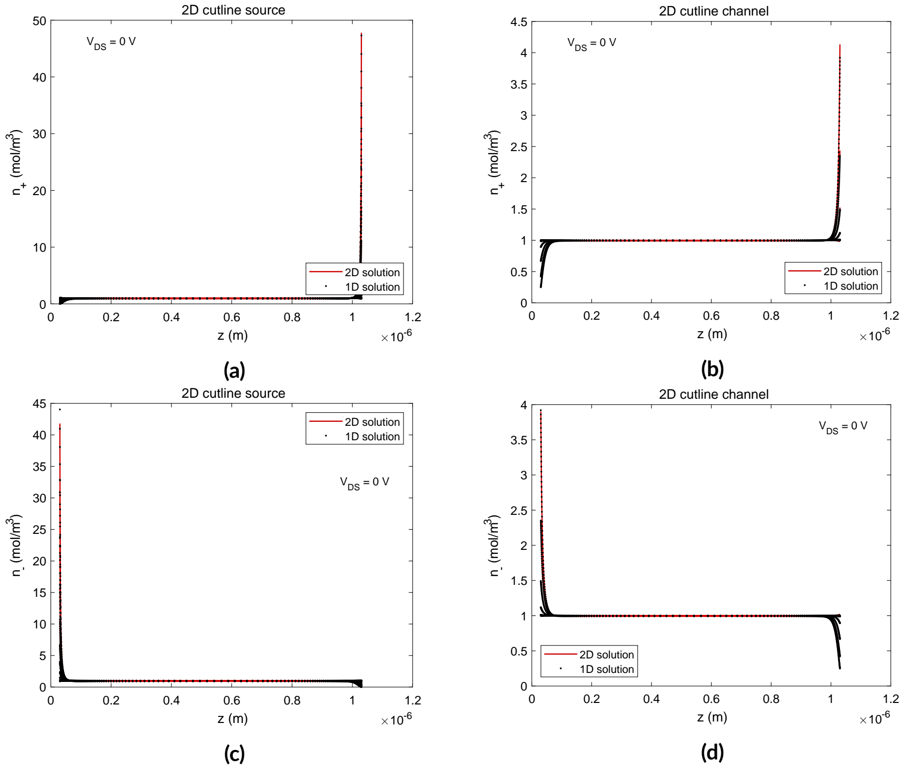

Figure 5.6: Distribution of the positive ions at the cutlines above the electrodes (a) and the channel (b) for $V_{\mathrm{DS}} = 0\,\mathrm{V}$ and likewise for the negative ions (c+d). Parameters are given in Table 5.1.

When a V_{DS} potential different from zero is applied, the free carrier charges in the semiconductor and the electrolyte show non-uniform distributions in response to the previous non-linear voltage distributions. In the following subsection, we discuss these non-uniform distributions by resorting to the sheet accumulated charges (or to the sheet conductivity, which is proportional to it). In Figure 5.7, we show the sheet net charge accumulated in the electrolyte along the longitudinal direction of the device for different V_{DS} and V_{GS}. As mentioned before, for V_{DS}=0V, the distribution is uniform, but when V_{DS} is different from zero, it is highly non-uniform. Moreover, the net sheet charge is non-zero, being negative close to the source and positive close to the drain. This means that due to V_{DS}, there is a charge transfer from the source to the drain region in the electrolyte. The overall (total)

ionic charge is, however, still zero as should be since no ionic exchange is allowed (and initially, the net total ionic charge was null).

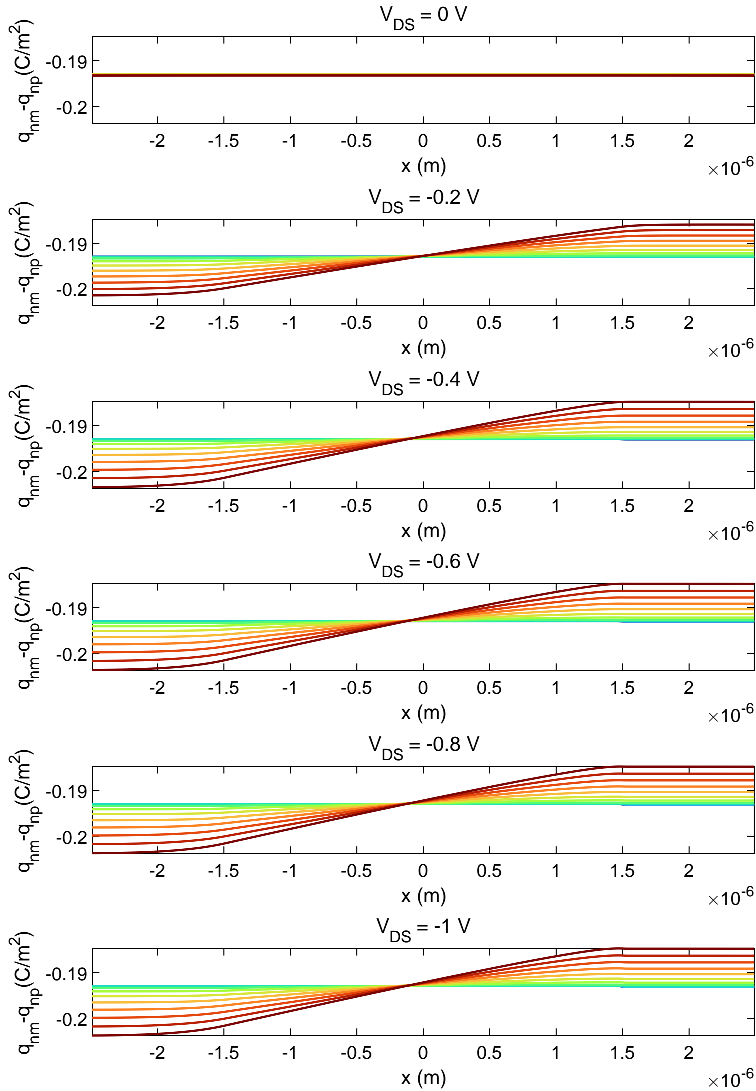

Figure 5.7: Charges distributed by the sum of ions integrated in vertical direction over the electrolyte. Parameters are given in Table 5.1.

5.4 Local Sheet Semiconductor Conductivity Distributions

The distribution of free carriers in the semiconductor film for V_{DS} different from zero is qualitatively similar to the ones described in the case of the Helmholtz model (see Figure 3.5). Therefore, the behavior of the sheet semiconductor conductivity defined in Equation (3.5) is expected to be also similar. Figure 5.8 shows the data obtained for the parameters in Table 5.1 for different V_{DS} and V_{GS}.

The conductivity increases with the concentration of free charge carriers, increasing when the gate voltage gets negative enough. With no gate voltage applied (or below the threshold), the semiconductor behaves like an insulator, and with the rise of the gate potential, the semiconductor becomes a conductor. Especially at the interface with the electrolyte, the substantial accumulation of holes leads to the highly conductive channel, which ultimately allows the drain-source current to flow. The characteristic conductivity drop along the channel when V_{DS} increases until the pinch-off is formed on the drain, with a minimum conductivity. Compared to the Helmholtz model, the formation of the pinch-off appears earlier than expected, probably due to the self-consistent interaction between the electrolyte and the semiconductor. Further work is necessary to understand this effect.

Figure 5.9 shows the sheet conductivity in the middle of the channel as a function of gate voltage V_{GS} for different V_{DS}. Qualitatively the behavior is like the one described when analyzing the Helmholtz model (dashed lines in Figure 5.9) (see Chapter 3), but there are quantitative differences between them. When the drain voltage increases, it shifts more, up to a limit, when the saturation regime is reached. For negative gate voltages, the conductivity in the subthreshold regime has few differences (see Figure 5.9, b).

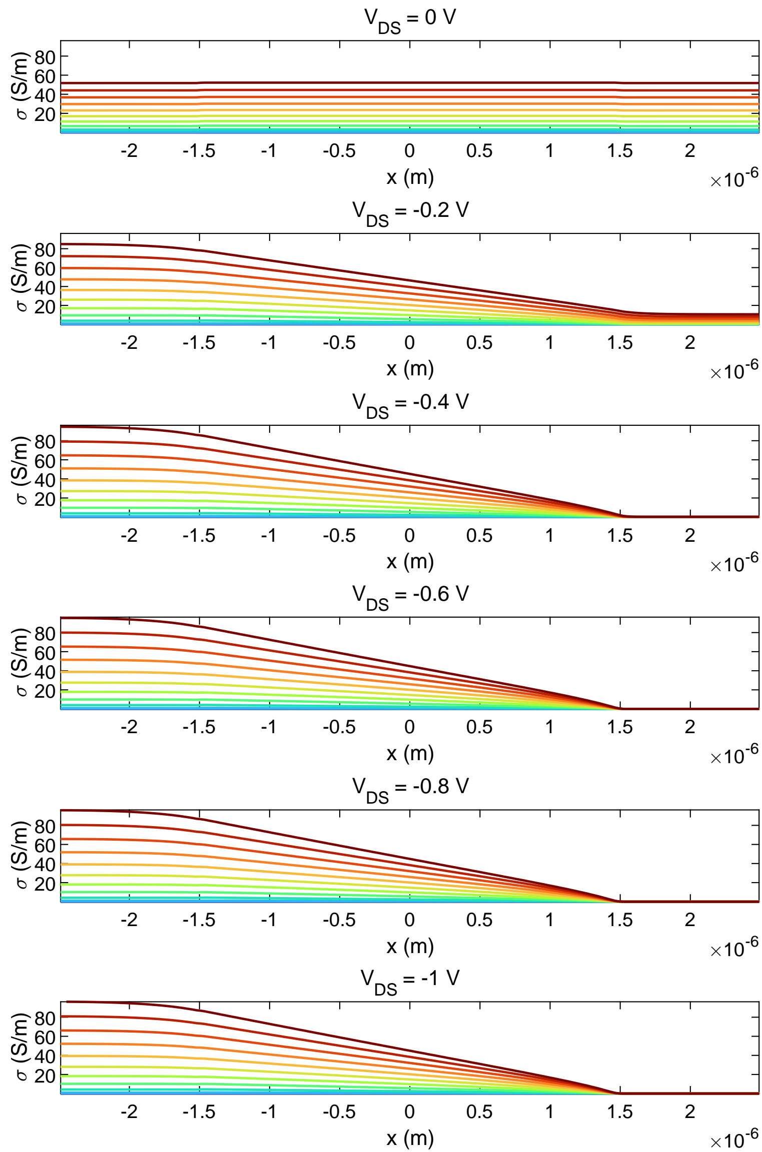

Figure 5.8: Sheet semiconductor conductivity along the channel in an EGOFET modeled with the 2D NPP model. Parameters are given in Table 5.1.

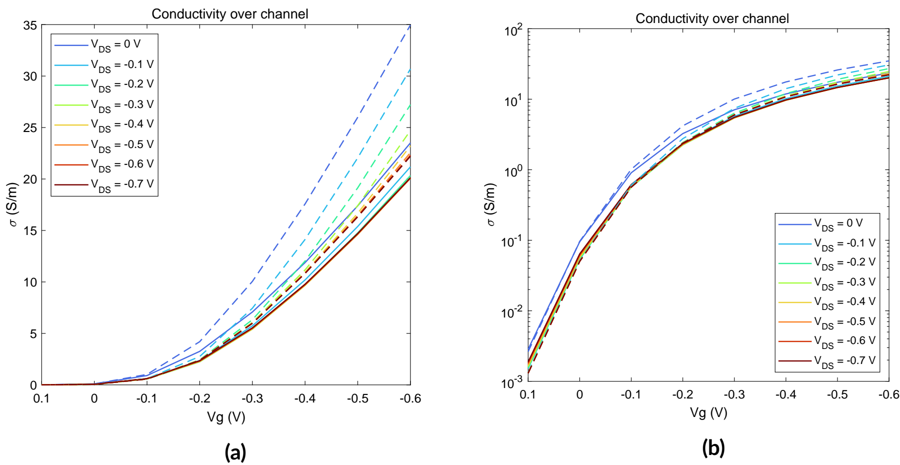

Figure 5.9: Sheet semiconductor conductivity in the middle of the channel as a function of the source gate voltage for different source-drain voltages in linear scale (a) and log scale (b). The dashed lines correspond to the predictions of the Helmholtz model. Parameters are given in Table 5.1.

Figure 5.10, shows the sheet semiconductor conductivity in the middle of the source electrode. The main interesting result is that, contrary to what happens in the Helmholtz approximation (dashed lines), in the NPP approximation, the source sheet semiconductor conductivity depends on the source-drain voltage, although the source is kept at the ground all the time. The effect is produced indirectly through the distribution of the ions in the electrolyte. The non-uniform distribution of holes along the channel produces a non-uniform distribution of ions in the electrolyte, implying the "transfer" of negative ions from the drain region to the source region. These additional negative ions attract further positive charges in the semiconductor in this region, resulting in a higher conductivity dependent on V_{DS}, as seen in Figure 5.10. The sheet conductivity in the source can reach even higher values than the ones predicted by the Helmholtz approximation. This effect may be magnified by the relatively short length of the simulation domain and the strict charge conservation conditions imposed on the electrolyte.

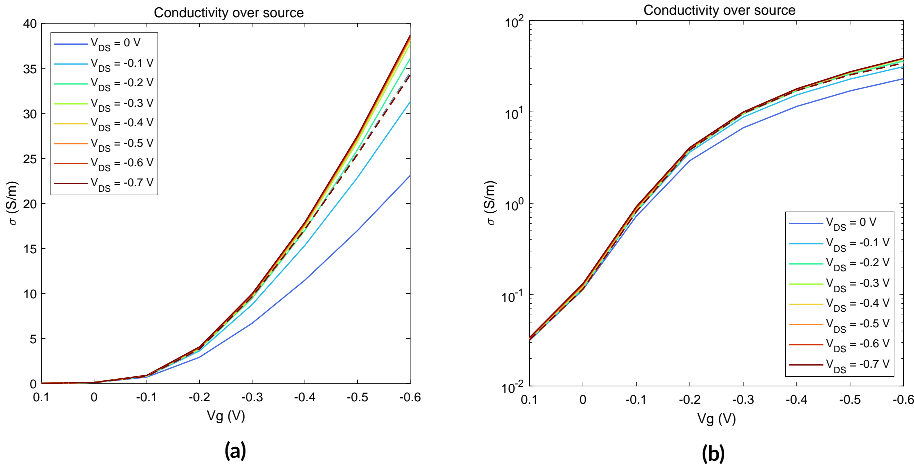

Figure 5.10: Conductivity over the source electrode in linear scale (a) and log scale (b). The dashed lines represent the predictions of the Helmholtz model (in this model, the sheet conductivity on the source is independent of V_{DS}). Parameters are given in Table 5.1.

Figure 5.11 provides the sheet semiconductor conductivity above the drain electrode. By increasing the drain voltage, the electric field over the drain electrode decreases, and fewer charge carriers accumulate, leading to the pinch-off (see Chapter 3). The sheet conductivity curves appear to shift when V_{DS} is varied, but the shift is not as simple as in the case of the Helmholtz model, probably due to the complex self-consistent interaction between the electrolyte and the semiconductor mentioned above.

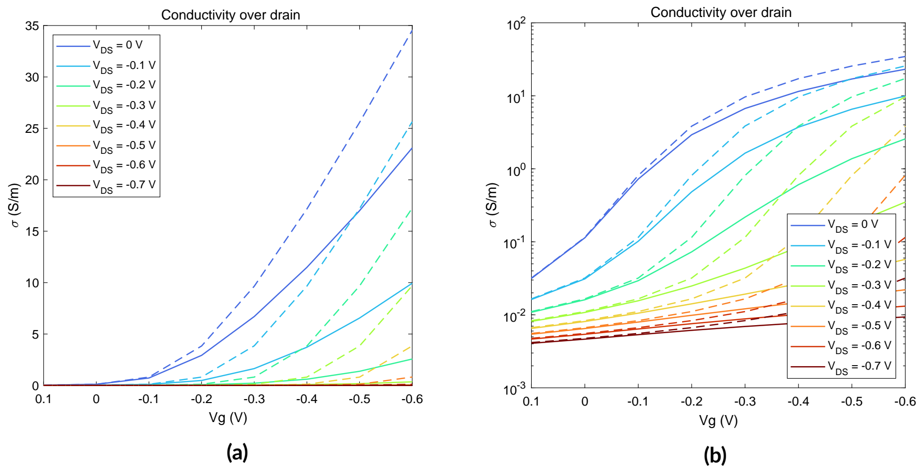

Figure 5.11: Conductivity over the drain electrode in linear scale (a) and log scale (b). The dashed lines represent the predictions of the Helmholtz model (in this model the sheet conductivity on the drain just shiftes with V_{DS}). Parameters are given in Table 5.1.

5.5 Influence of Material Parameters

The previous section showed the characteristics of an EGOFET in operation as predicted by the NPP model. We indicated how the transfer curves are correlated to the conductivity maps. In the Chapter 4, we used the 1D model to investigate the influence of interfacial layers and ion concentration. Here, we investigate the effects of some additional device parameters (hole mobility and injected hole density).

5.5.1 Hole Mobility of the Semiconductor

The free charge carrier mobility is a material parameter of the semiconductor, which depends on its electronic structure. The conductivity is proportional to the mobility. Given the structure of the drift-diffusion model and for constant mobilities, the current is expected to scale up with the mobility and the sheet accumulated charges, for instance, to be independent of it. Figure 5.13 gives the sheet semiconductor charge q_{sem} at $V_{\text{DS}} = -0.2$ V for different mobilities, showing its independency from mobility, as long as the mobility is field independent. However, even with the same charge distribution, the current-voltage characteristic depends on mobility (see Figure 5.12) since the conductivity is proportional to the accumulated charge and mobility. The upward shift of the conductivity curves in Figure 5.12 (b) shows this direct proportionality.

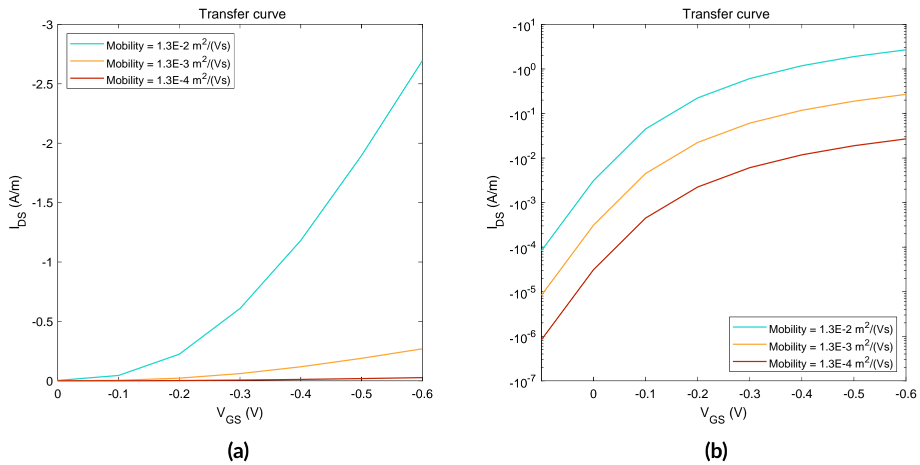

Figure 5.12: Transfer curve in both linear and logarithmic scale at V_{DS} = -0.4 V for the hole mobility $_{sem} = \{3.4 \times 10^{-4}\,\mathrm{m}^2/(\mathrm{Vs}), 3.4 \times 10^{-5}\,\mathrm{m}^2/(\mathrm{Vs}), 3.4d - 6m^2/(Vs)\}$. Parameters are given in Table 5.1.

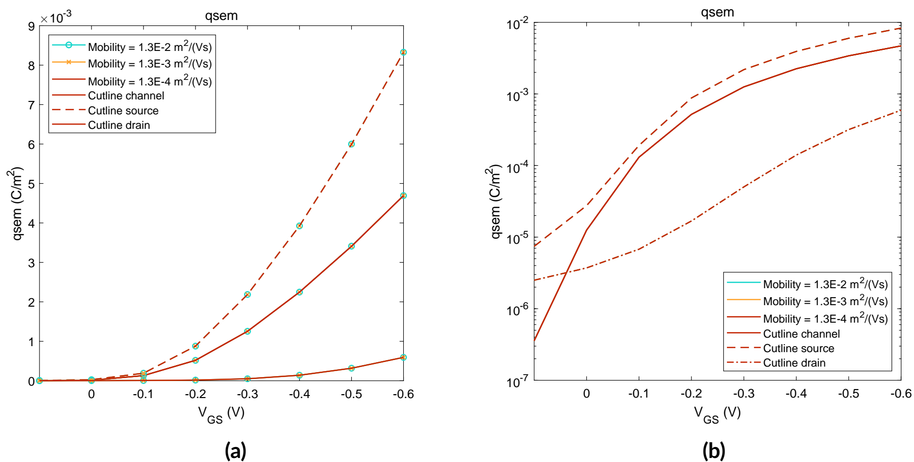

Figure 5.13: Accumulated charges in the semiconductor of the EGOFET sheet above the channel, source and drain electrode as a function of the gate voltage for $V_{DS} = -0.2\,\mathrm{V}$. Parameters are given in Table 5.1.

5.5.2 Injected Hole Concentration in the Semiconductor

The injected hole concentration is defined as the initial value and as the Dirichlet BC at the source and the drain electrodes (fixed hole concentration corresponding to an ideal diffusive injecting contact). We remember that this hole concentration is related to the injection energy barrier. Figure 5.14 shows the transfer curve for $V_{\mathrm{DS}} = -0.4\,\mathrm{V}$ for different hole injected densities n_{h}. The current increases with increasing hole concentration, as expected. We observed that for the hole concentrations $n_{\mathrm{h}} = \{6 \times 10^{13}, 6 \times 10^{15}, 6 \times 10^{17}\}\,1/\mathrm{m}^3$ the current increase is directly proportional to the hole concentration in the whole range of V_{GS} voltages. The calculated current at $V_{\mathrm{GS}} = 0.1$ V for $n_{\mathrm{h}} = 6 \times 10^{15}\,1/\mathrm{m}^3$ might be a numerical artefact. For the hole concentrations of $n_{\mathrm{h}} = \{6 \times 10^{19}, 6 \times 10^{21}\}\,1/\mathrm{m}^3$, the proportionality is kept in the subthreshold regime, but there is a tendency in the on-state to become independent from n_{h}. In this regime, the effect of n_{h} can be interpreted as a shift in the threshold voltage, in agreement with the predictions made by the analytical expression derived from the Helmholtz model [56].

In Figure 5.15, the bulk potential shift of the electrolyte depending on the injected hole concentration for $V_{\mathrm{DS}} = -0.4\,\mathrm{V}$ is visualized. The increase in the hole concentration leads to a higher potential in the semiconductor in the channel at the semiconductor/electrolyte interface above the source electrode. This leads to an increase in the electrolytes' bulk potential. For low concentrations, the potential above the channel is nearly flat (see Figure 5.15, right), which is also reflected in the accumulated charges.

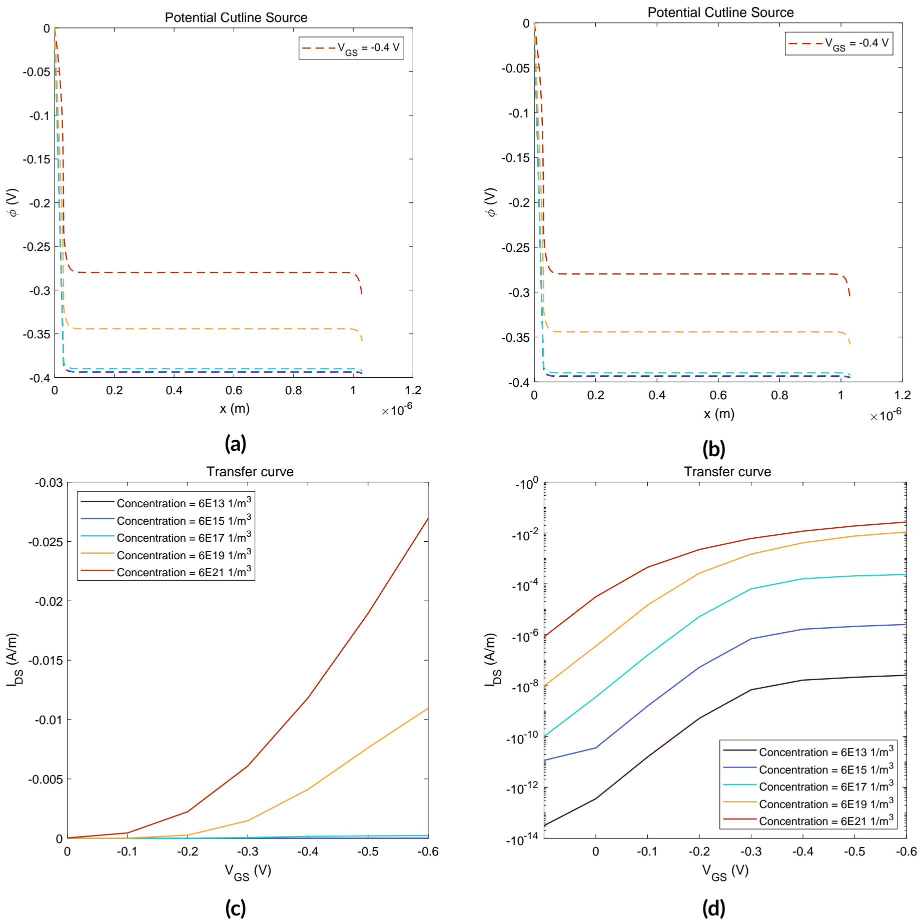

Figure 5.14: Transfer curve in both linear and logarithmic scale at $V_{\mathrm{DS}} = -0.4\,\mathrm{V}$ for the hole concentrations of $n_{\mathrm{h}} = 6 \times 10^{13}\,1/\mathrm{m}^3$, $6 \times 10^{15}\,1/\mathrm{m}^3$,$6 \times 10^{17}\,1/\mathrm{m}^3$, $6 \times 10^{19}\,1/\mathrm{m}^3$, $6 \times 10^{21}\,1/\mathrm{m}^3$. Parameters are given in Table 5.1.

There is no conductive channel formation at the interface for the semiconductor's lowest injected hole densities (see Figure 5.16, black line). For higher concentrations with $n_{\mathrm{h}} > 6 \times 10^{19}\,1/\mathrm{m}^3$, a strong accumulation of charge carriers at the interface is seen, which is responsible for the amplification character of the EGOFET device.

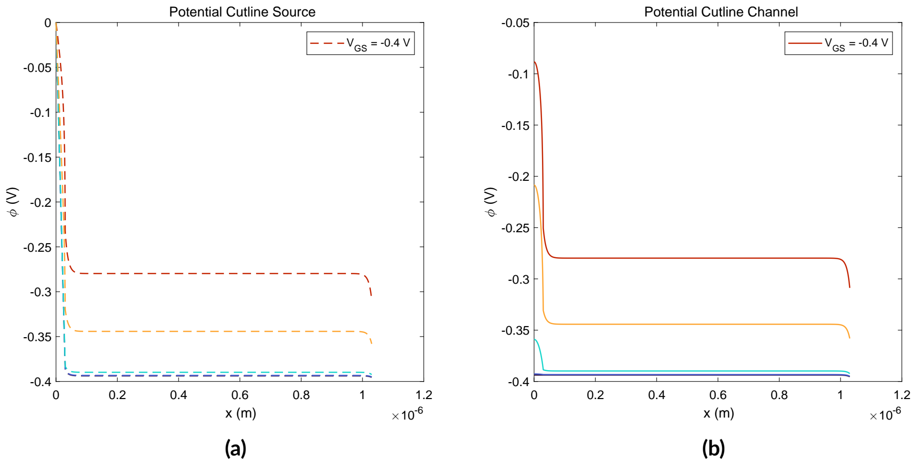

Figure 5.15: Potential cutlines over the source electrode and over the channel at $V_{GS} = -0.4\,\text{V}$ for the hole concentrations of $n_h = 6 \times 10^{13}\,1/\text{m}^3$, $6 \times 10^{15}\,1/\text{m}^3$, $6 \times 10^{17}\,1/\text{m}^3$, $6 \times 10^{19}\,1/\text{m}^3$, $6 \times 10^{21}\,1/\text{m}^3$. Colors referring to the same concentration as in Figure.

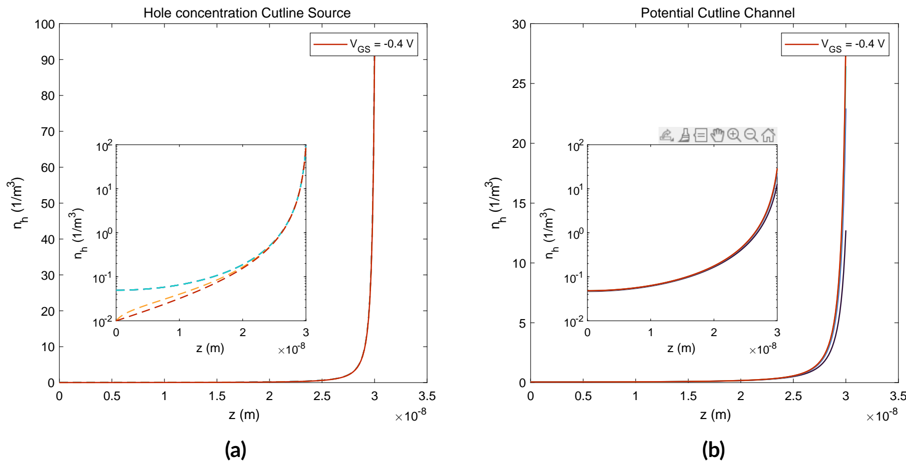

Figure 5.16: Hole concentration distribution in the cross-section above the source electrode and the channel at $V_{DS} = -0.4\,\text{V}$ for the hole carrier concentrations $n_h = 6 \times 10^{13}\,1/\text{m}^3$, $6 \times 10^{15}\,1/\text{m}^3$, $6 \times 10^{17}\,1/\text{m}^3$, $6 \times 10^{19}\,1/\text{m}^3$, $6 \times 10^{21}\,1/\text{m}^3$. Parameters are given in Table 5.1. Colors referring to the same concentration as in Figure.

5.6 Influence of Device Geometry

EGOFETs can be produced in many different geometries, including different channel and gate lengths. Often these geometries are constrained by the sensing system into which the EGOFET is to be integrated. In this section, we will investigate the influences of the channel length and gate lengths. The study of the geometric parameters requires intrinsically of a 2D device model like the one implemented in this thesis.

5.6.1 Influence of the Channel Length

The channel length influences the source-drain current, as we have already seen in the case of the Helmholtz model. In the ideal case, for a given width, one expects a $1/L$ dependence (see Equation 1.7). The lower the distance between source and drain, the higher the current will be. Figure 5.17 shows the transfer curves (normalized by the width W) for $V_{DS} = -0.4\,\mathrm{V}$ for different channel lengths, plotted in linear and logarithmic forms. It is observed how indeed, the current seems to scale with $1/L$ for $L > 1\,\mu\mathrm{m}$. To better evaluate this dependency, we have plotted in Figure 5.17, (c) and (d), the current values by keeping the W/L ratio constant (i.e. changing W the same amount as L, that is, we plot $I_{DS}(A/m) \times W/L \times L(m)$. In this case, one would expect that the variation of the channel length L (and the width accordingly) will be independent of the actual value of L and only be dependent on the ratio W/L, which is kept constant. We observe that the curves depend on L for $L < 2\,\mu\mathrm{m}$, meaning there are short channel effects in this range of values. Figure 5.18 shows the source-drain current over the channel length for different V_{GS} and $V_{DS} = -0.2\,\mathrm{V}$, confirming what was said before, although with some dependency on the actual value of V_{GS}. As discussed in the case of the Helmholtz model, these effects are probably related to the relevance of access series resistance effects. We note that in the NPP model, the transition to the long channel limit seems to be reached for a lower channel length value.

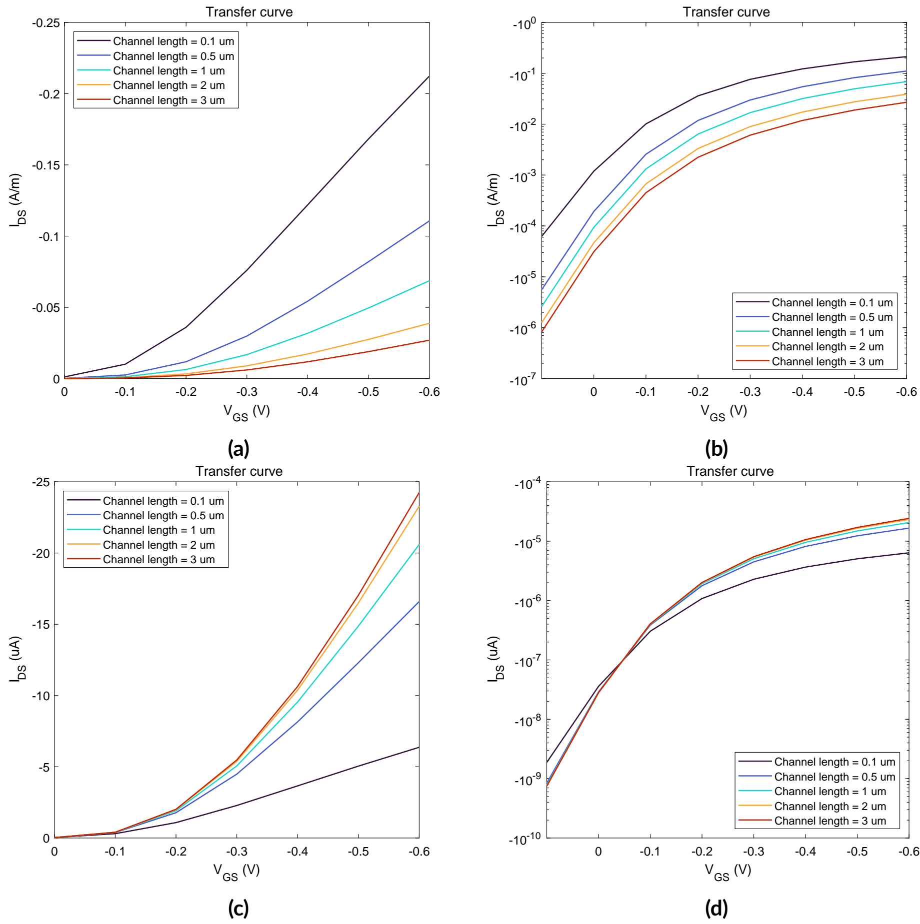

Figure 5.17: (a) and (b) Transfer curves in both linear and logarithmic scale at $V_{DS} = -0.4\,\text{V}$ for the channel lengths $l_{\text{channel}} = \{0.1\,\mu\text{m}, 0.5\,\mu\text{m}, 1\,\mu\text{m}, 2\,\mu\text{m}, 3\,\mu\text{m}\}$. (c) and (d) Same data but keeping the W/L ratio constant and equal to 167. Parameters are given in Table 5.1.

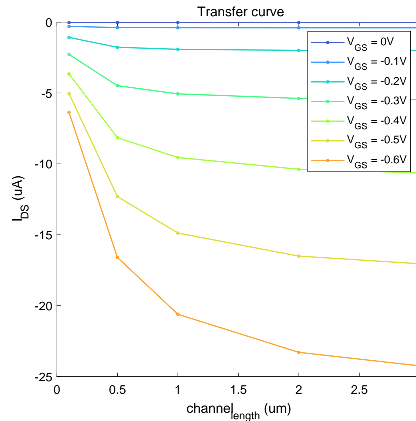

Figure 5.18: Source-drain current for $V_{DS} = -0.2\,\mathrm{V}$ as a function of the channel length for different V_{GS}. Parameters are given in Table 5.1.

5.6.2 Influence of the Gate Length

In an EGOFET, the gate size will be tailored depending on the device integration. Figure 5.19 (a) shows the transfer curve at $V_{DS} = -0.4\,\mathrm{V}$ corresponding to three different gate sizes, namely, $l_{gate} = \{5.8\,\mu\mathrm{m}, 4.35\,\mu\mathrm{m}, 2.9\,\mu\mathrm{m}\}$, while keeping the channel and electrodes lengths constant at $l_{channel} = 3\,\mu\mathrm{m}$, $l_S = l_D = 1\,\mu\mathrm{m}$. As expected, the larger the gate surface, the larger the source drain-source current since the coupling is more effective (of course when the overlap with the electrodes exceeds the electrode lengths, a further increase does not improve the current anymore. The effect of the lower coupling can be evidenced by plotting the charges accumulated above the channel and source and drain electrodes (see Figure 5.19 (b)). A small gate does not induce a strong enough electrical field to attract enough charge carriers to form a conductive channel, hence no significant current flow [49].

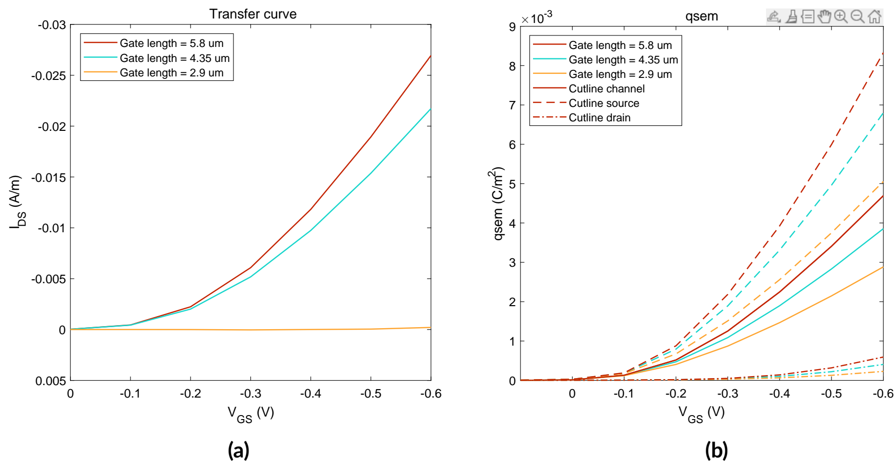

Figure 5.19: Transfer curves and accumulated charges at $V_{\mathrm{DS}} = -0.4\,\mathrm{V}$ for the gate length $l_{\mathrm{gate}} = \{5.8\,\mu\mathrm{m}, 4.35\,\mu\mathrm{m}, 2.9\,\mu\mathrm{m}\}$. Parameters are given in Table 5.1.

5.7 Summary

- In this chapter, we revealed the importance of ionic diffusive effects when modeling EGOFETs with the two-dimensional model. The current-voltage characteristics are significantly lowered with the NPP model compared to the Helmholtz model.
- We overlayed the potential distribution with the one-dimensional model, which is in excellent agreement.
- The two-dimensional NPP model allows the comparison of the potential distribution along the channel. We compared the potential distributions for linear, transition, and saturation regimes for different heights in the semiconductor film. For $V_{DS} = 0\,\mathrm{V}$, we could see a uniform distribution which transforms to a non-uniform distribution, even directly at the interface with the electrolyte.
- The ion distribution shows the expected formation of the electrical double layer which is also in perfect agreement with the one-dimensional solution. We exhibit the electrolyte's net charge distribution in a longitudinal direction. A two-dimensional model which includes the electrolytes-free carriers is necessary to obtain these results.
- The pinch-off effect could be seen in the sheet semiconductor conductivity along the channel. This correlated with the electric field maps.
- We compared the conductivity behavior in the vertical direction with the results obtained by the Helmholtz simplification. As expected from the results of the voltage-current characteristics, the conductivity was lowered. However, a dependency on VDS was observed for the conductivity over the source electrode, which must be studied further.
- The advantage of such a model is the easy access to parametric study to reveal material parameters and geometry dependencies. This will help to explain and plan experimental outcomes to save valuable time and costs. We give examples of such parametric studies to reveal the dependency on the hole mobility, injected hole concentration, channel, and gate length.

PART IV

FINAL REMARKS

Chapter 6

Discussion

This thesis presented EGOFET physical models in the Helmholtz and the NPP frameworks and implemented its numerical resolution.

Our modeling approach to the Helmholtz model is similar to the one reported in Melzer et al. [47], where the electrolyte is modeled as the Helmholtz capacitance c_{H}. In contrast to their model, we assumed a planar source and drain electrodes on the bottom of the device, a typical configuration in fabricated EGOFETs. This allows us to investigate the conductivity changes over the source and drain for the three operation regimes and correlate them with the output curves (see Figure 3.8). We analyzed the transfer and conductivity behavior in detail, allowing us to compare it later with the more detailed NPP model. Although we cannot mimic the ionic diffusive effects in the electrolyte in this simplification, the model accurately reproduces the current-voltage characteristics of an actual EGOFET device. The subthreshold, linear, and saturation regimes are identified in the output characteristics, and it provides a more accurate description than the usual ideal FET model, which fails in accurately describing the cross-over from subthreshold to the linear regimes.

The implementation of the EGOFET NPP model has been realized with the same domain equations as in Delavari et al. [46]. They reported convergence issues with the time-dependent solver and the electrolyte's 'no flux' boundary conditions, representing a contained electrolyte with a fixed ion concentration. Their approach was to first apply a boundary condition with a fixed concentration at a boundary and calculate the time-dependent behavior, which reflects the more physically accurate device outputs, as they reported. In contrast to their model, we used a continuous bias voltage defined as an additional function to calculate the

transfer and output curves (see Section 2.3). This keeps the ion concentration at the amount of the initial concentration, which reflects the actual device properties under static operation.

Moreover, we could show that a very high mesh resolution at the interface is required $\approx 0.1\,\mathrm{nm}$ to achieve mesh independency. The conductivity becomes values were lower for a coarser mesh at the interface, which leads to unphysical phenomenological device parameters.

Additionally, we modeled EGOFETs properties using 1D models, reflecting the behavior above the electrolyte and the channel. We demonstrated that many applications could already be modeled with this simplified approach, which gives results in minutes. This is crucial for fitting experimental data and running parameter studies with many variations, as many simulations are needed.

Further, we added the Stern layer as a distributed capacitance in the NPP model, which was not present in previous implementations. Without this additional layer, the hole concentration at the interface increases unphysically, leading to wrong device parameters while overlaying with experimental data. In Figure 4.1, the voltage drop at the gate interface responsible for this restraint is visualized.

When an EGOFET is used as a biosensor, the current-voltage characteristics change. When the biomarker binds to the biorecognition layer, the interfacial capacitance changes due to the thickness of the molecule. Moreover, these molecules are usually charged, adding fixed charges to the gate voltage. As in experimental setups, these sources of changes are combined; having a model gives the advantage of studying these effects separately.

With the one-dimensional model in the NPP framework, we showed that these fixed charges shift the device response by $\Delta V = \sigma_G / c_G$. For practical data analysis, this means that by measuring the voltage shift, one can estimate the fixed charges of a molecule and vice versa. This shift is usually correlated with the threshold voltage V_{th}, the intercept of the tangent of the linear part of the transfer curve. However, we show that true linearity in the operational window is not reached, whereas V_{th} strongly depends on the gate voltage. In contrast, the Helmholtz model shows an asymptotic approach toward this linear behavior when this classical definition of a threshold voltage becomes a better approximation.

We also simulated the changes due to the thickness of the interfacial layer by assuming the presence of SAMs with molecules of different carbon lengths. For lower distributed capacitances at the gate interface, the capacitance approaches a maximum gate-source capacitance asymptotically. As the system capacitance is

correlated with the derivative of the conductivity over voltage, one can say that when the capacitance becomes constant, the conductivity has a linear part. Also, then, the voltage threshold definition is valid again.

To sum up, we can say that the threshold voltage definition is a valid approximation in some specific cases. The definition was initially adapted from the ideal FET model, where the different regimes are well defined, whereas EGOFETs show broader transition regimes or are even prevented from having an actual linear part in the transfer characteristics.

In Section 4.5, we showed the dependency on the ionic strength in the conductivity changes of the semiconductor using the 1D NPP model. We showed that there is a dependency on the ion concentration inside the electrolyte for low concentration, whereas it reaches an upper limit for higher concentrations. This upper limit is equivalent to having the electrolyte modeled in the Helmholtz framework. The Helmholtz framework states that there is no voltage drop over the electrolyte, whereas it can be modeled as the Helmholtz capacitance c_H. In Figure 4.11, it can be seen that for ion concentrations $> 100\,\mathrm{mM}$, the voltage drop over the whole electrolyte (including the diffusive ionic layers) is neglectable, and the Helmholtz approximation is valid. Then the approximation of the V_th becomes valid. The results derived in the present work contribute to a more quantitative and reliable interpretation of EGOFET biosensor data.

Although the one-dimensional models are helpful for many applications, they have limitations due to numerical stability, device geometry, and carrier mobility. For this reason, we introduced our most complex model, the two-dimensional model in the NPP framework. We confirmed the dependency of the transistor current on the gate area as reported in Delavari et al. [46, 49]. They report how a small gate electrode acts like a point source, where the electric field is not built up to the strength that charges in the semiconductor are attracted to the interface. We add to the report of the channel length influence (see Figure 5.17) the visualization of the shifting of the electrolyte's bulk potential, hence the limited charge accumulation at the interface.

Overall, we give a deeper understanding of the nanoscale dependencies while reflecting the current-voltage characteristics' macroscale behavior. We optimized the underlying numerical model to directly calculate the characteristics without intermediate steps in a resolution lower than a micrometer. We integrated the Stern layer into the framework, giving more reliable solutions. The limitations of the classical models with the threshold voltage dependency on the gate voltage

were disclosed. Finally, we gave some examples of parameter studies for device optimization, which will help to save valuable experimental time and costs. We showed the separated influences of the biorecognition layers in a sensing unit. This thesis gives another step towards detailed and relevant physical modeling for developing a fast, cheap, and reliable EGOFET biosensor.

Chapter 7

Conclusion and Perspectives

Numerical models help us to better understand physical behavior with less effort, time, and cost. However, there is no such thing as a universal model. Each model is tailored to a particular purpose by making assumptions and simplifications, mainly to keep the computational cost within reasonable limits. Before actual use, every model must be validated and verified against the intended purpose to ensure quantitative agreement with experiments.

In this thesis, we presented several models to study the behavior of EGOFETs. First, we showed the EGOFET in the Helmholtz simplification. Here, the electrolyte is not modeled explicitly. Instead, it is given by an equivalent capacitance introduced as a distributed capacitance at the gate electrode. This assumption reduces the computational cost drastically, while still supplying potential and charge carrier maps in two dimensions. For experiments with a high ionic strength, where the impact of the electrolyte's ionic diffusive effects is neglectable, this model provides sufficient detail. Second, we present an EGOFET model in the Nernst-Planck-Poisson (NPP) framework, where charge carriers (holes) in the semiconductor and ions in the electrolyte are described explicitly. This model offers the possibility to study geometrical effects such as the influence of the gate size, including the effect of the electrolyte. One simplification of the computational expensive NPP model are the one-dimensional models: These represent the cross-section above the electrode (source or drain) and the second the cross-section above the channel. The models include explicit descriptions of holes and ions. Although the one-dimensional models are only valid for $V_{\mathrm{DS}} = 0\,\mathrm{V}$, we show that the main features are already given at this voltage. We showed how the conductivity curves calculated within this model represent the macroscale

behavior and correlate the results with the two-dimensional model. Therefore, this simplification is suitable for providing results within significantly shortened computational time for different experimental configurations.

Finally, with the two-dimensional NPP model, we were able to provide information on the influence of the device's geometry and material parameters while calculating current-voltage characteristics directly. To our knowledge, no other existing model has been able to include both ionic diffusive effects as well as the Stern layers. Two models [47, 48] made use of the Helmholtz simplification. Delavari et al. [49] used the NPP framework, but did not include the Stern layer. We showed that this interfacial layer limits the charge accumulation in the semiconductor interface, implying a voltage drop directly at the electrolyte's interfaces. To limit computational costs, we made the assumptions of the absence of traps and constant mobility. Voltage-dependent mobility could be introduced by taking the voltage at each point coupled with an additional PDE in the 'Definitions' section of COMSOL Multiphysics 5.5 or by coupling the equations to a Matlab input. In future research, this could improve the consistency with experimental data. The simulations shown in this thesis are made in one- and two-dimensional settings. To include the exact device setup and study the influence of interdigitated geometries, a three-dimensional model might be required, depending on the setup. Due to the multiscale nature of the work, this would introduce a high number of degrees of freedom.

The diffusion effects can be modeled using the NPP framework with its explicit description of ions. This is relevant when interfacing with cells in setups with brain connections for epilepsy [72] or the recording of cardiac cells [2]. When recording cardiac cells, the cleft between the cell and the semiconductor plays a role in the amplitude of the signal. The distributed capacitance influences the conductivity at the electrolyte/semiconductor interface. When ions stream outside of the cells, they modify the interface locally. The bigger the cleft is, the more room is left for ionic diffusion into the bulk electrolyte, which lowers the measurable signal. The presented framework can be extended to model a cell inside the electrolyte by coupling the cell surface with models of the action potential raised in a cardiac cell and its distribution of ions into the electrolyte. With a parameter study of different distances, the measurable signal can be calculated as a function of the cell's distance to the surface (see Figure 7.1).

Another possible extension of the developed framework would be to model the penetration of ions into the semiconductor film. This could mimic the behavior of

organic electrochemical transistors (OECT), which are currently gaining interest among researchers. Although they have a lower switching time, they offer a high on-off ratio with high absolute currents.

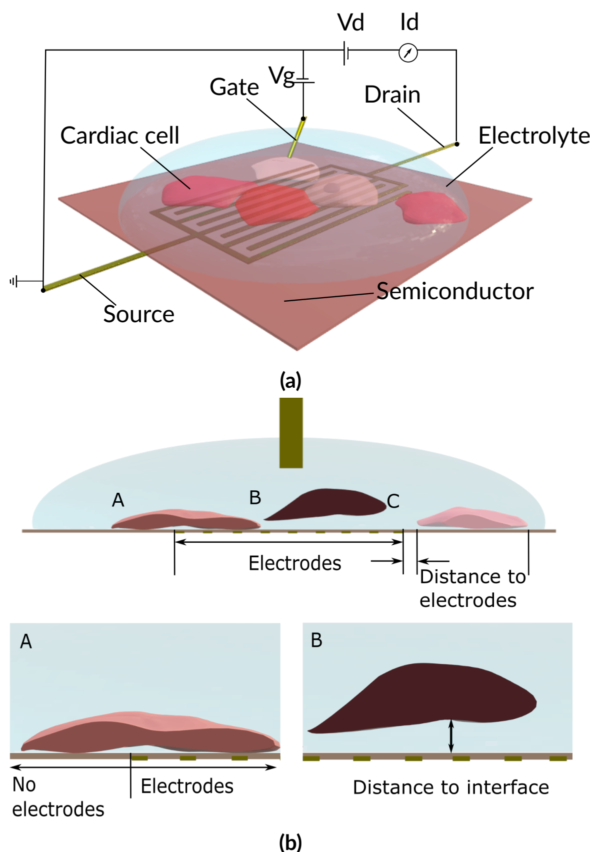

Figure 7.1: (a) Scheme of cardiac cells on an EGOFET for cell recording. (b) Illustration of the problem of the cleft distance (B to A) in horizontal direction and (C to A) in vertical direction, when the cells are not on top of the electrode.

In this thesis, we overcome some limitations of understanding EGOFET biosensors, which are promising elements for healthcare devices that detect diseases quickly, easily and cheaply. We provide tools for supporting research in this field to eventually bring these devices into daily clinical practice and home testing devices.

Appendix A

Appendix 1

The three model option mentioned in Section 2.2.2 overlay of the distributed capacitance is higher than $1 \times 10^4\,\mathrm{F/m}$. The overlay is in perfect agreement (see Figure A.1).

We performed a mesh independency study for the one-dimensional and two-dimensional models in the Nernst-Planck-Poisson framework. Following, we present the meshes we investigated. We kept a high resolution at the interfaces of interest in all the meshes: gate/electrolyte, electrolyte/semiconductor, semiconductor/source, and semiconductor/drain. We first meshed with triangular elements,

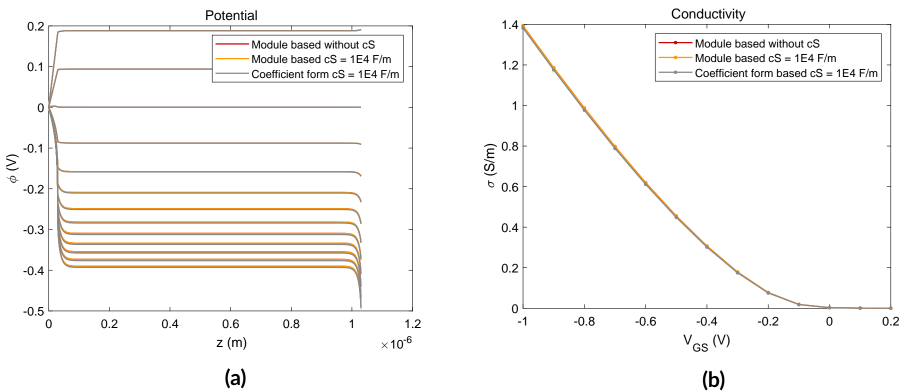

Figure A.1: (a) Overlay of the potential along the EGOFET of the one-dimensional models . Two models are with the modules ‘Electrostatics’ and ‘Transport of Diluted Species’ and one model with the coefficient form PDE tool of COMSOL Multiphysics 5.5. For an interfacial capacitance of $c_{\mathrm{Int}} = c_{\mathrm{S}} > 1 \times 10^4\,\mathrm{F/m}$, the difference is less than %. (b) The overlay of conductivity shows no significant difference.

having a high ratio of smallest to largest element while having a good element quality. The quality can get less if the elements get skewed (having a large side and a small side). However, the triangular elements could not give the required accuracy while keeping computational costs low, so rectangular elements have been chosen. Further explanations are found in Chapter 2.

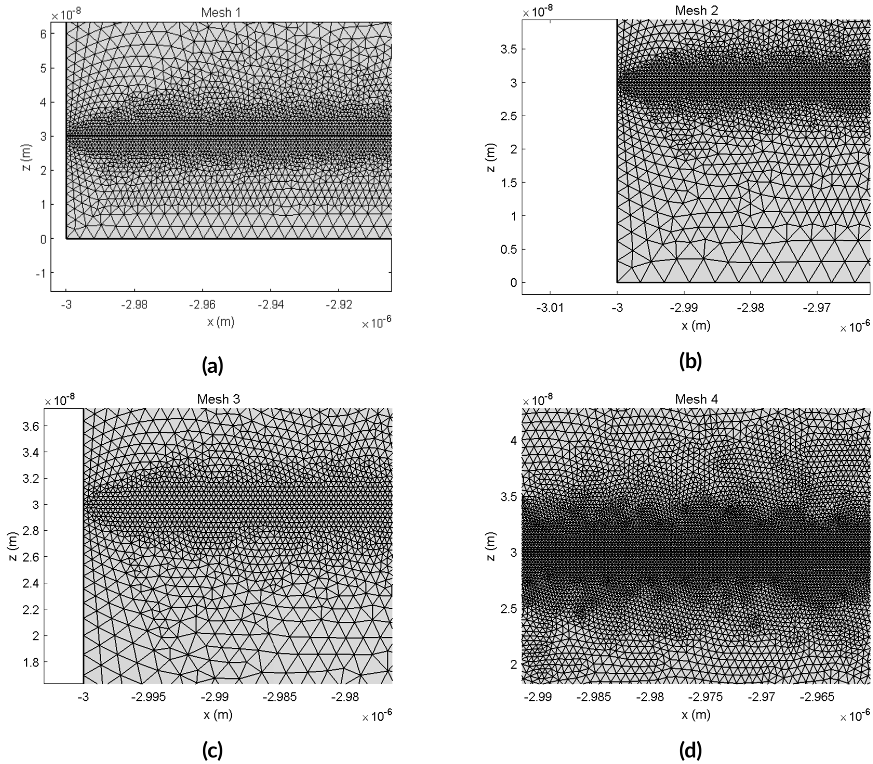

Figure A.2: Mesh 1-4 for mesh independency study.

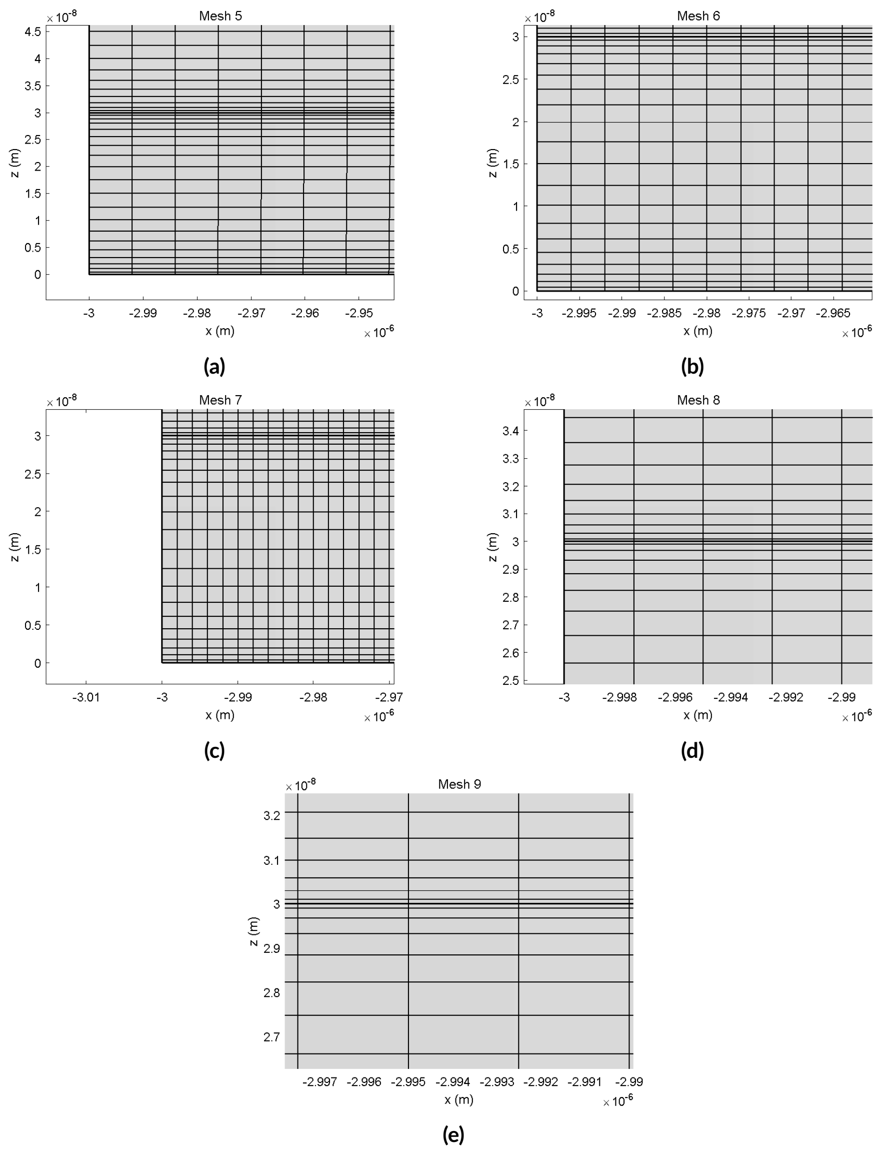

Figure A.3: Mesh 5-9 for mesh independency study.

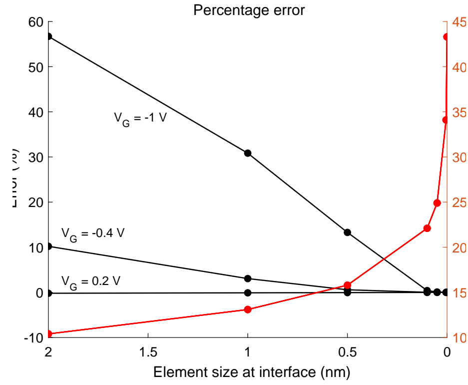

Figure A.4: Percentage error to the one-dimensional model considering the potential distribution over the drain cutline.

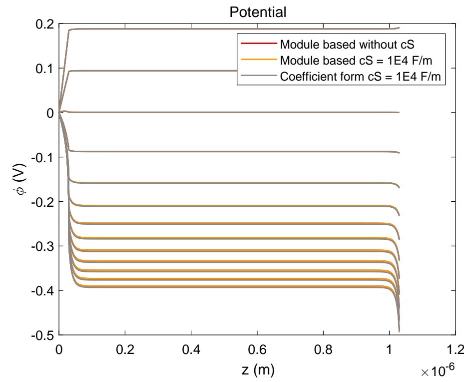

Figure A.5: Potential overlay of two-dimensional simulations with the same framework but different mesh sizes.

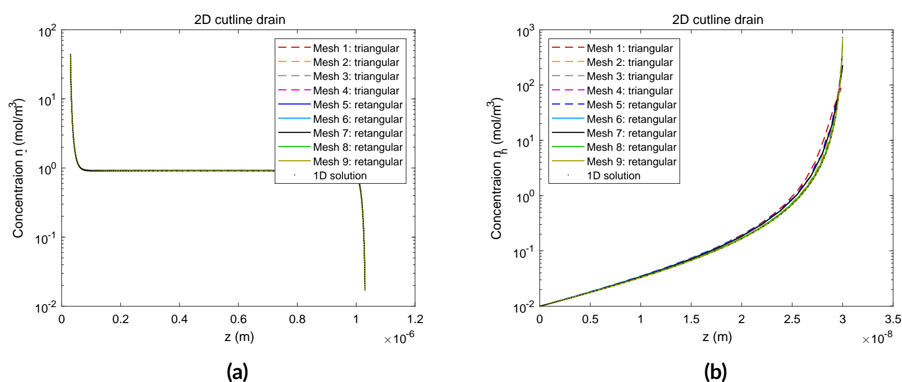

Figure A.6: (a) The concentration of the negative ions for $V_{GS} = -1$ V along (z-direction) the EGOFET. No significant difference between the meshes was observed. (b) The hole concentration inside the semiconductor along the model is shown in the right. At the interface to the electrolyte at $z = 3 \times 10^{-8}$ m, a difference between the meshes is observed.

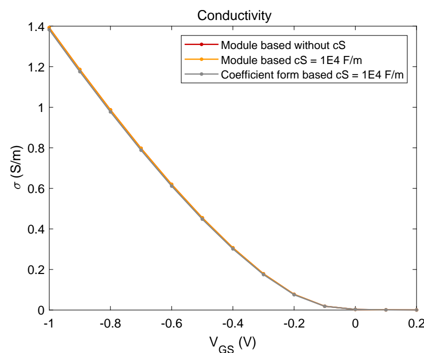

Figure A.7: Conductivity for different meshes within the same system and the one-dimensional solution. The higher the mesh resolution, the closer it gets to the one-dimensional solution.

Appendix **B**

Appendix 2

In Chapter 4, we investigated the influence of the distributed capacitance on the device output. In the following, we show the threshold voltage shift for the studies performed in Chapter 5.

Figure B.2 shows the conductivity and capacitance over the gate voltages for different distributed capacitances. The distributed capacitance and the electrolyte/semiconductor interface c_{int} is kept constant. In Section 4.4.2, we discuss the differences in the placement of the self-assembled monolayer when attached to the source and drain electrode, semiconductor/electrolyte interface, and gate electrode.

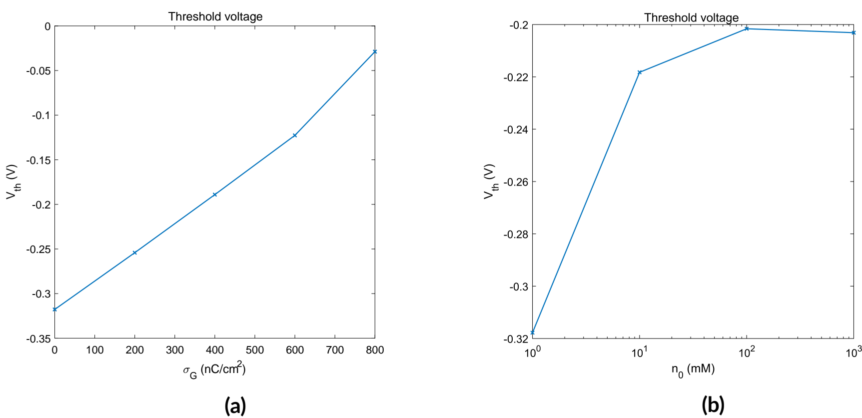

Figure B.1: (a) The influence of distributed capacitance on the threshold voltage is defined in the usual understanding of different distributed capacitances and (b) different ion concentrations.

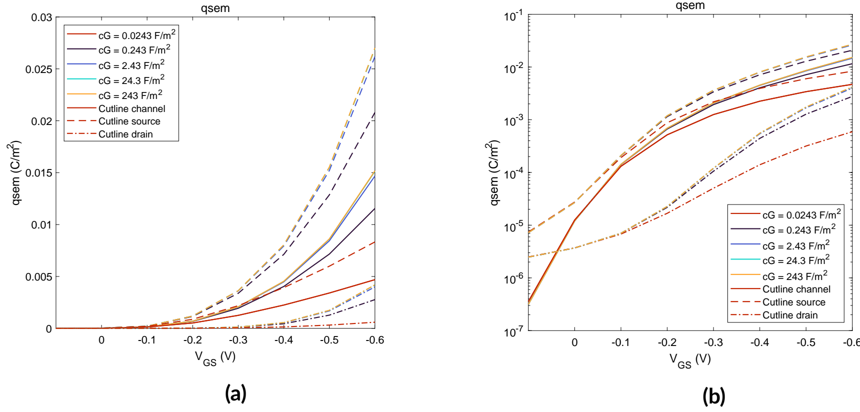

Figure B.2: Distributed capacitance of SAM at the gate and $c_{\text{int}} = 0.0243\,\text{F/m}^2$.

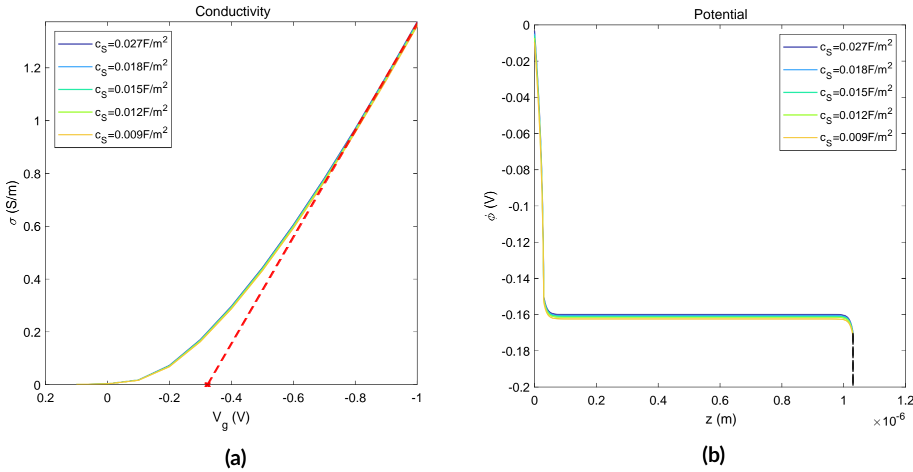

Figure B.3: Conductivity over gate potential for different source interfacial capacitances c_S. The threshold voltage remains the same. The corresponding potential distribution for $V_{GS} = -0.2\,\text{V}$ is given, where little changes in the bulk potential can be seen.

We repeated the study to place the SAM at the source and drain electrode. Figure B.3 demonstrates that the SAM has no significant influence in the absence of the metal work function for $V_{DS} = 0\,\text{V}$. However, this remains to investigate for an applied drain voltage.

Appendix C

Appendix 3

The potential distribution in the EGOFET is defined by the electrostatics and the concentration of the charge carriers. In the following, the potential distribution of the device with the parameters shown in Chapter 5 is shown. The graphs in Figure C.1 together with the those shown already in Section 5.3 provide the potential distributions in the typical operational range of an EGOFET.
The conductive channel between source and drain is formed by the high accumulation of charge carriers (holes). In the following, we show the evolution of charge accumulation at $V_{\mathrm{GS}} == \{-0.2, -0.4\}$ V. for $V_{\mathrm{DS}} = \{0, -0.2, -0.6\}$ V. In the Figures C.2 and C.3, it is observed that the formation of the conductive channel is local at the interface to the electrolyte, as expected. There is nearly no additional carrier accumulation in the areas close to $z = 0\,\mathrm{m}$.

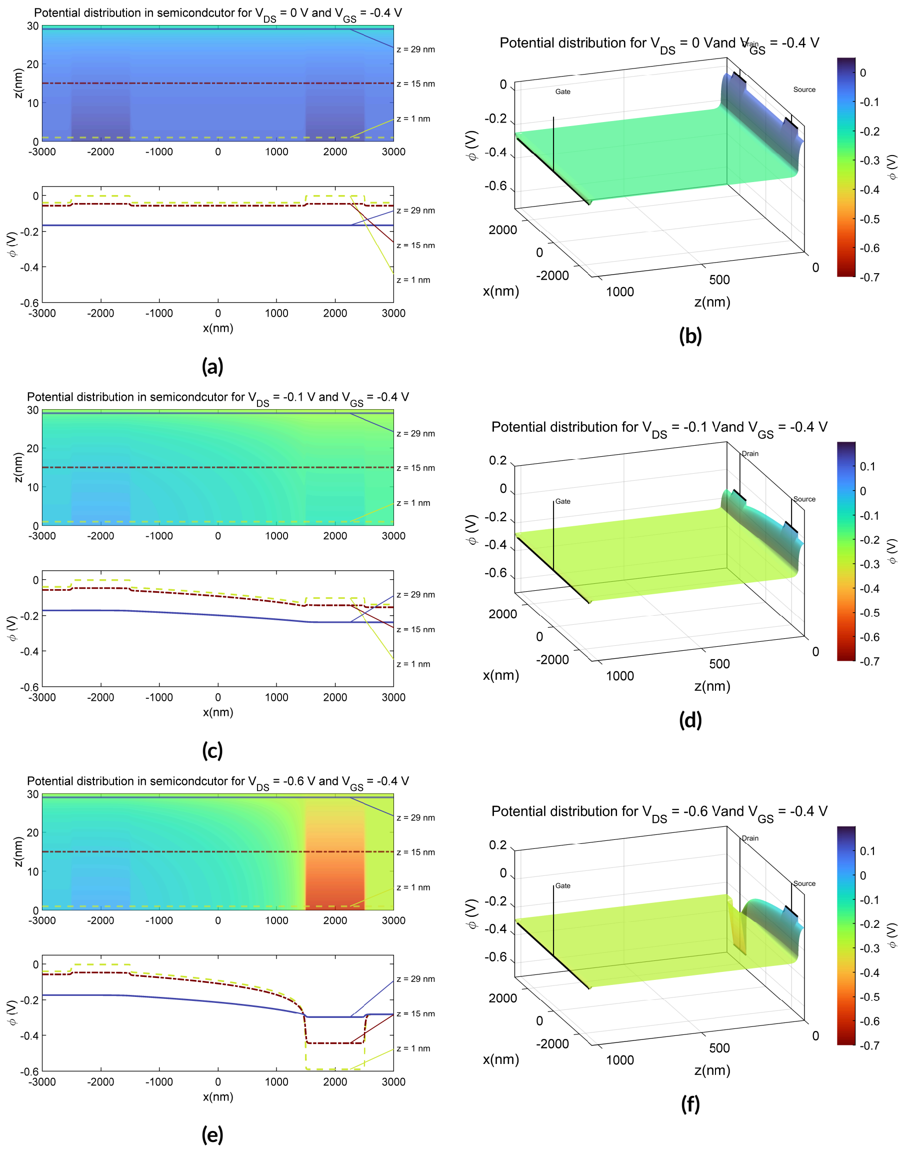

Figure C.1: Potential distribution in 2D for $V_{GS} = -0.4$ V and the evolution over the gate voltage for $V_{DS} = \{0, -0.4, -0.6\}$ V. In the right the potential over the full device is shown. In the graphs in the right, the potential inside the semiconductor with horizontal cutlines at $z = 1, 14, 29$ nm is displayed.

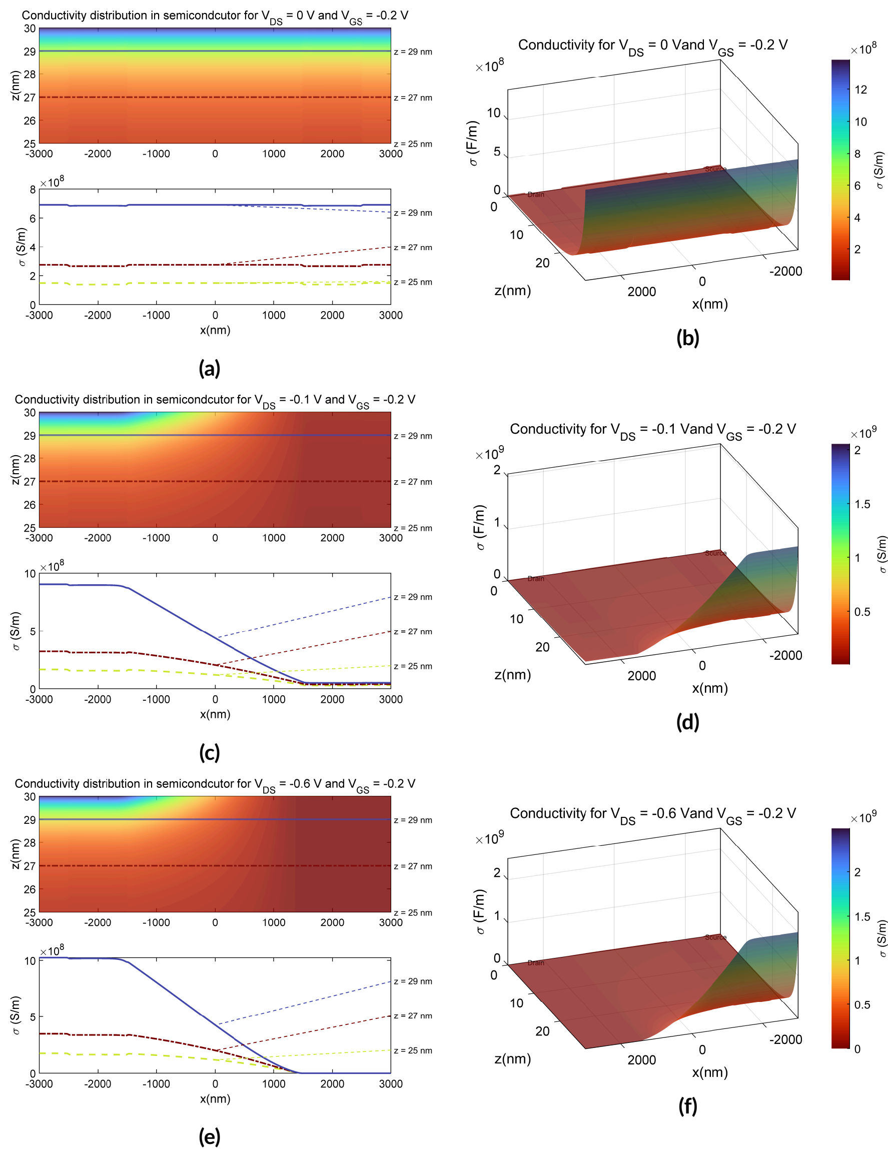

Figure C.2: Conductivity inside the semiconductor for $V_{\mathrm{DS}} = \{0, -0.4, -0.6\}$ V and $V_{\mathrm{GS}} = -0.2V$. The colormaps in (a), (b) and (c) 2 nm of the semiconductor next to the interface with the electrolyte. Horizontal cutlines of $z = [25, 27, 29]$ nm are shown on the left side.

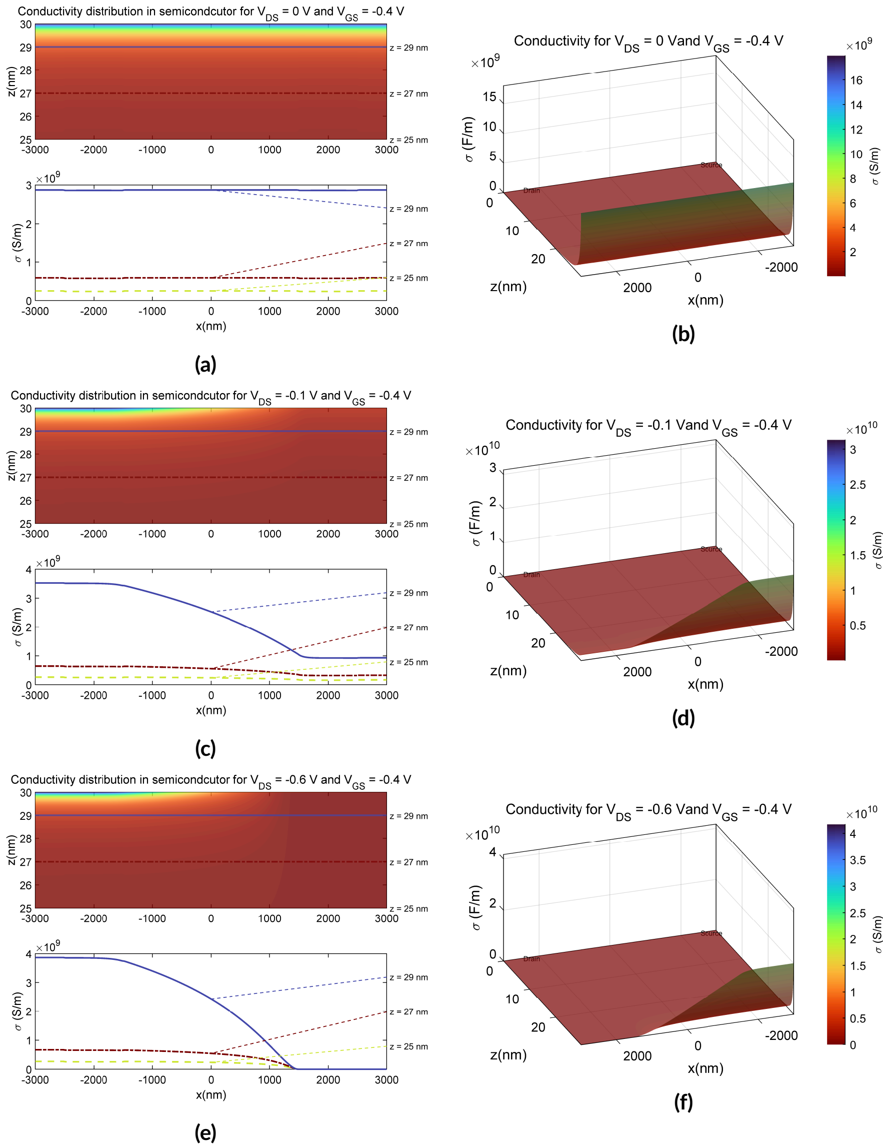

Figure C.3: Conductivity inside the semiconductor for $V_{DS} = \{0, -0.4, -0.6\}$ V and $V_{GS} = -0.4V$. The colormaps in (a), (b) and (c) 2 nm of the semiconductor next to the interface with the electrolyte. Horizontal cutlines of $z = [25, 27, 29]$ nm are shown on the left side.

Appendix **D**

Appendix 4

Chapter 5 shows the influence of the hole concentration on the transfer curve. The transfer curves are correlated with the conductivity changes in the semiconductor. These conductivity changes are calculated from the accumulated charges q_{sem} in the semiconductor. Figure D.1 gives the charge accumulation above the source and drain electrode and the channel. For lower hole concentrations, we observe a proportional increase in the current in relation to the increase of the hole concentration, whereas, for higher concentrations, it tends to reach a maximum (see Section 4.5).

In Chapter 4, we discussed the influence of the ion concentration in the one-dimensional model in the NPP framework. We repeated the simulations in the two-dimensional framework in the following, finding the same conclusions. However, transfer curves are calculated directly, whereas only conductivity curves have been analyzed in the one-dimensional framework.

We checked the independency of the electrode length to the simulation. In real devices, the electrode is usually longer. However, as we assume an ideal contact, the electrode length does not influence distributions in the performed studies. In the two-dimensional studies, we used an electrode length of 1 µm.

We repeated the parameter study for the role of the distributed capacitance at the gate electrode. We found that for higher distributed capacitances, the current also increases. All the studies are performed with a gate distributed capacitance of $c_{\mathrm{G}} = 0.0243\,\mathrm{F/m2}$, which corresponds to the distributed capacitance of the Stern layer. If the capacitance is high, it acts like an absence of the Stern layer. This leads to unphysical results. The distributed capacitance at the gate limits the current.

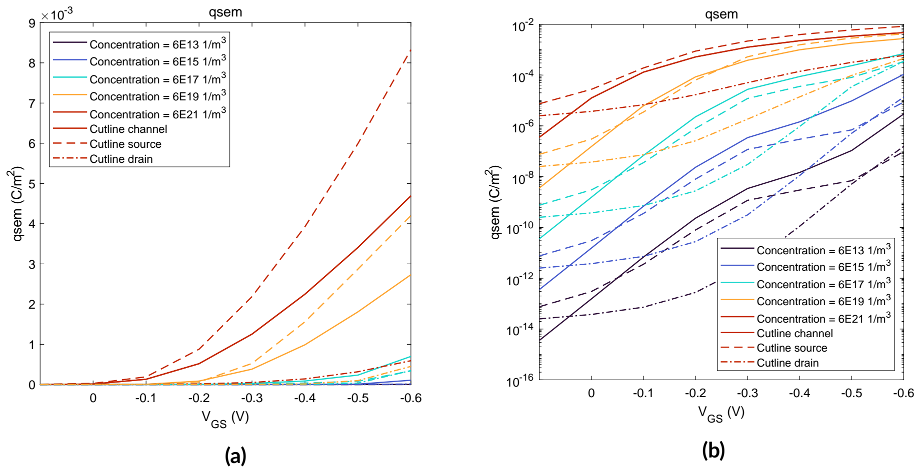

Figure D.1: Accumulated charges in the semiconductor sheet above the channel, source and drain electrode at $V_{\mathrm{DS}} = -0.4\,\mathrm{V}$ for the hole concentrations of $n_{\mathrm{h}} = \{6\times10^{13}\,1/\mathrm{m}, 6\times10^{15}\,1/\mathrm{m}, 6\times10^{17}\,1/\mathrm{m}, 6\times10^{19}\,1/\mathrm{m}, 6\times10^{21}\,1/\mathrm{m}\}$ in (a) linear and (b) logarithmic scale.

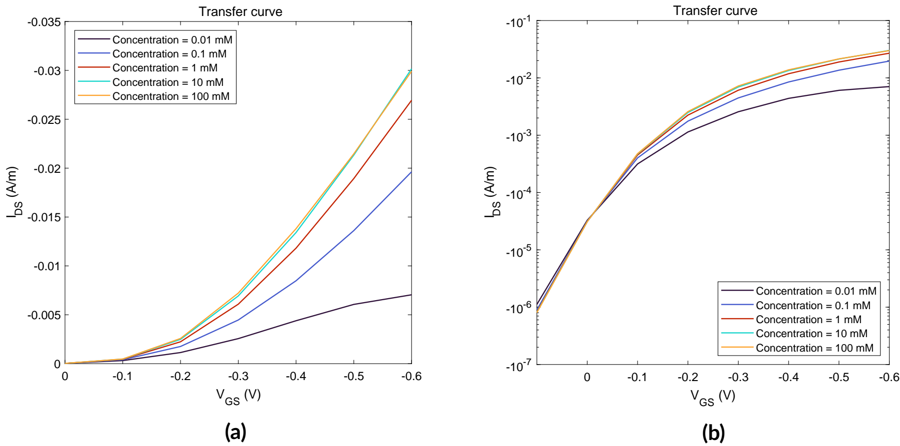

Figure D.2: (a) Transfer curves in both linear and (b) logarithmic scale at $V_{\mathrm{DS}} = -0.4\,\mathrm{V}$ for different ion concentrations $n_0 = \{0.01, 0.1, 1, 10, 100\}$ mM.

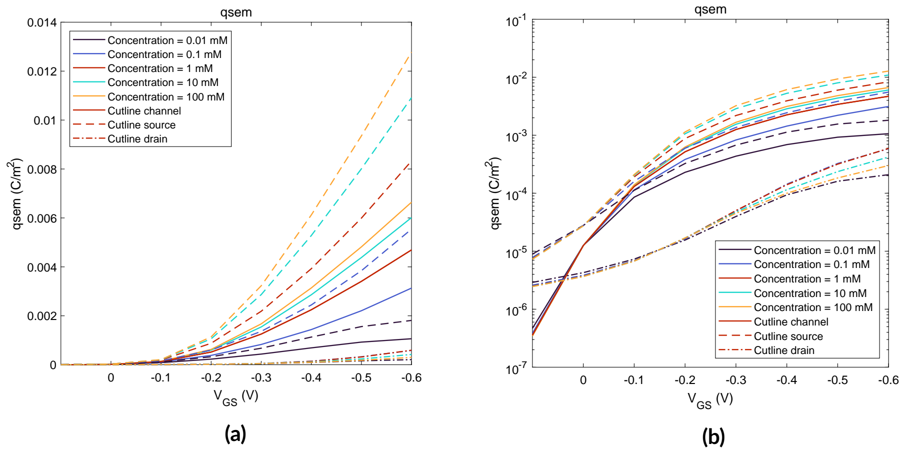

Figure D.3: Accumulated charges in the semiconductor sheet above the (a) source and (b) channel electrode at $V_{\mathrm{DS}} = -0.4\,\mathrm{V}$ for different ion concentrations $n_0 = \{0.01, 0.1, 1, 10, 100\}$ mM.

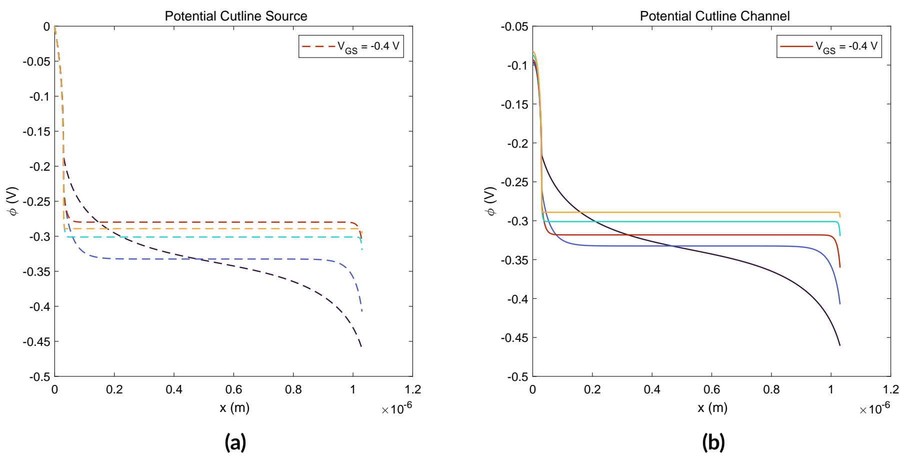

Figure D.4: Potential distribution above the (a) source and (b) channel electrode at $V_{\mathrm{DS}} = -0.4\,\mathrm{V}$ for different ion concentrations $n_0 = \{0.01, 0.1, 1, 10, 100\}$ mM. For very high concentrations, the double layers of the gate/electrolyte interface and the semiconductor/electrolyte interface are overlapping.

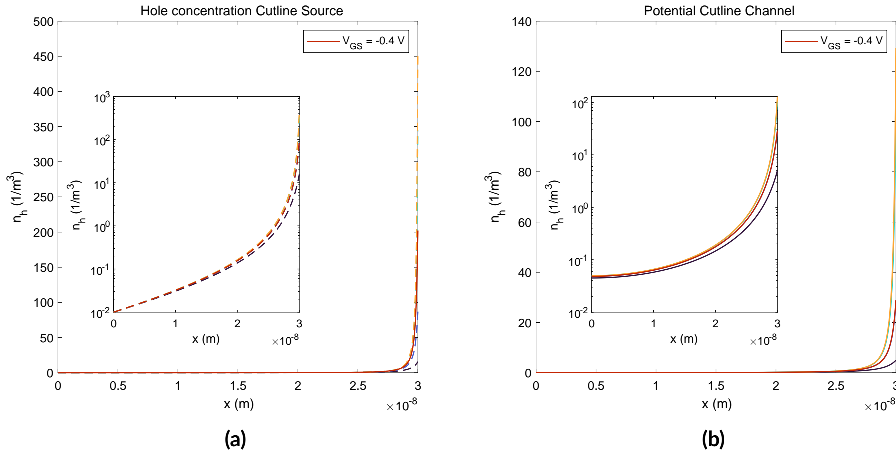

Figure D.5: Hole concentration distribution in the semiconductor sheet above the (a) source electrode and (b) at $V_{\mathrm{DS}} = -0.4\,\mathrm{V}$ for different ion concentrations $n_0 = \{0.01, 0.1, 1, 10, 100\}$ mM.

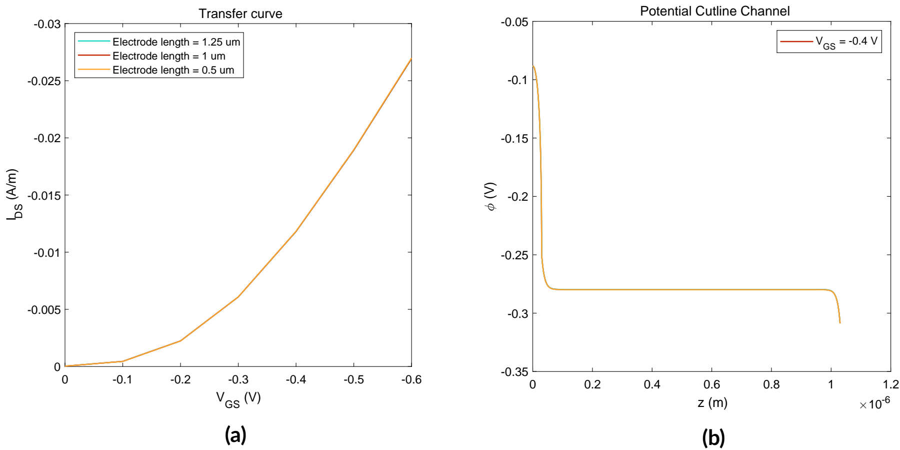

Figure D.6: Transfer curves (left) and potential cutline above the channel (right) at $V_{\mathrm{DS}} = -0.4\,\mathrm{V}$ for different electrode length of $l_{\mathrm{electrode}} = \{1.25, 1, 0.5\}\,\mu\mathrm{m}$.

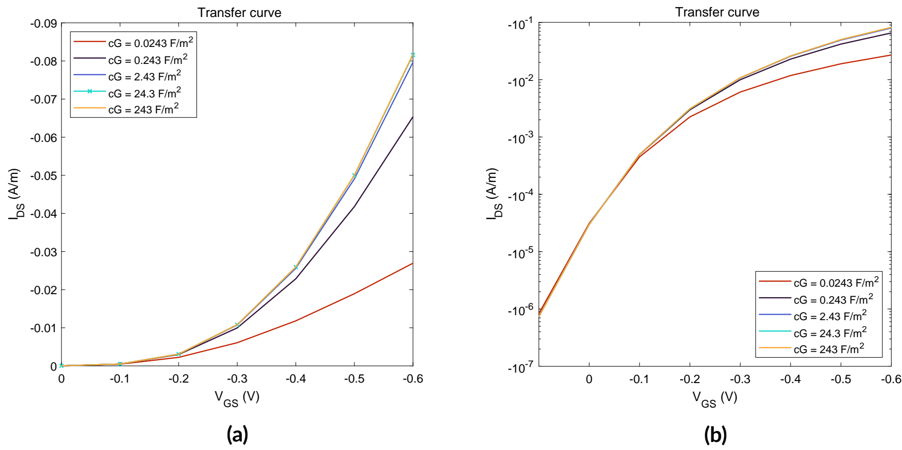

Figure D.7: Transfer curves in both (a) linear and (b) logarithmic scale at $V_{DS} = -0.4\,\mathrm{V}$ for different distributed capacitance $c_G = \{0.0243, 0.243, 2.43, 24.3243\}\,\mathrm{F/m^2}$.

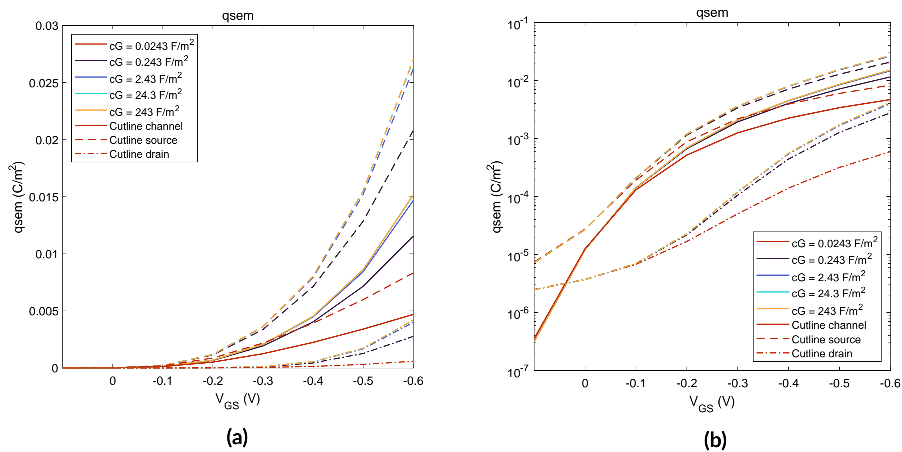

Figure D.8: Accumulated chares in both (a) linear and (b) logarithmic scale at $V_{DS} = -0.4\,\mathrm{V}$ for different distributed capacitance $c_G = \{0.0243, 0.243, 2.43, 24.3243\}\,\mathrm{F/m^2}$.

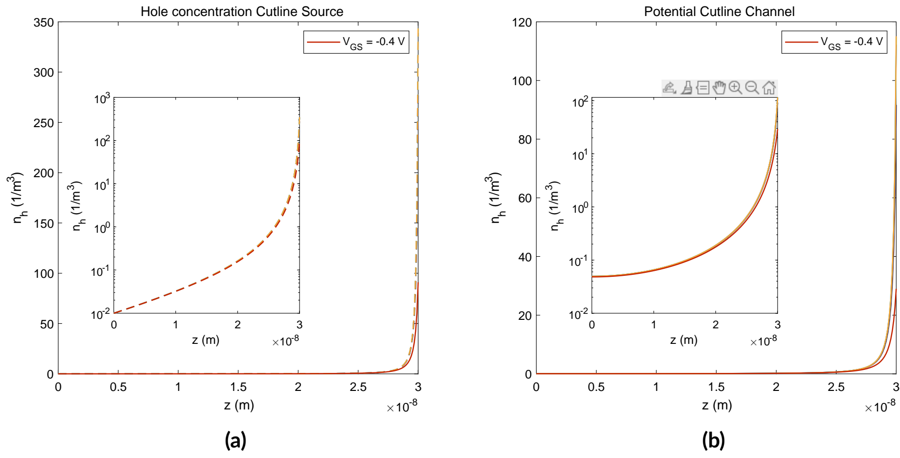

Figure D.9: Hole concentration above the (a) source electrode and (b) the channel at $V_{DS} = -0.4\,\text{V}$ for different distributed capacitance $c_G = \{0.0243, 0.243, 2.43, 24.3243\}\,\text{F/m}^2$.

Appendix **E**

Appendix 5

As modeling tools are demanded while designing and explaining experiments, we developed a modeling app for EGOFET interpretation and experimental evaluation. The app is based on MATLAB application tools and can be installed with MATLAB compiler.

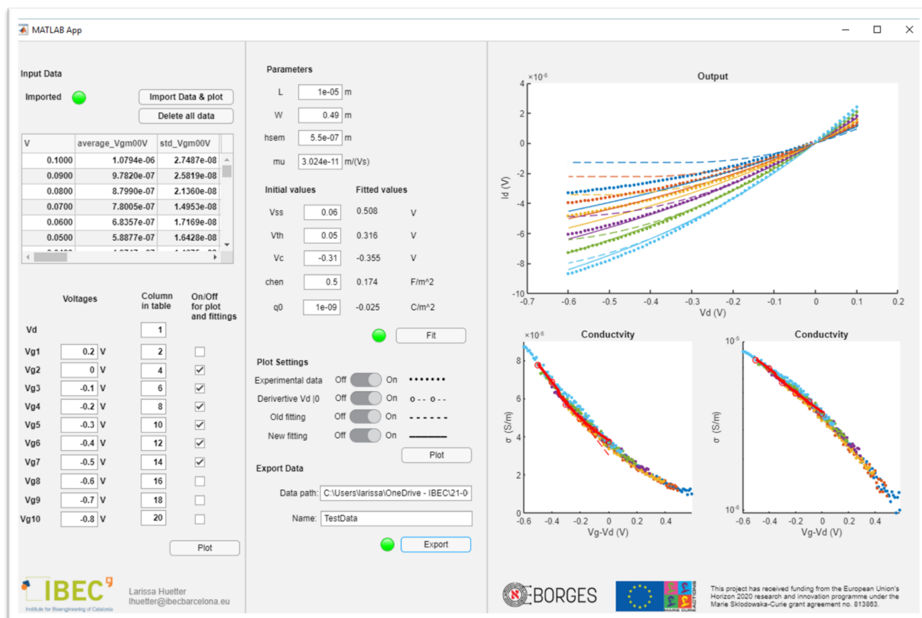

Figure E.1: Modeling EGOFET app, based on a MATLAB application.

Appendix F

Constants and Units

Parameter	Description	Value	Unit
ε_0	Vacuum permittivity	8.8541×10^{-12}	F/m
k_B	Boltzmann constant	1.3806×10^{-23}	J/K
e	Elementary charge	4.8032×10^{-10}	C
N_A	Avogadro constant	6.0221×10^{23}	1/mol

Parameter	Description	Unit
L	Channel length	m
W	Channel width	m
D_{elec}	Electrolyte diffusion coefficient	m^2/s
h_{elec}	Electrolyte length	m
μ_{elec}	Electrolyte mobility	$m^2/(Vs)$
$\varepsilon_{r,elec}$	Electrolyte relative permitivitty	-
c_G	Gate distributed capacitance	F/m^2
c_{Int}	Interfacial distributed capacitance	F/m^2
$\varepsilon_{r,int}$	Interfacial relative permitivitty	-
$\varepsilon_{r,SAM}$	SAM relative permitivitty	-
d_{SAM}	SAM thickness	m
h_{elec}	Semiconductor length	m
μ_{sem}	Semiconductor mobility	$m^2/(Vs)$
$\varepsilon_{r,sem}$	Semiconductor relative permitivitty	-
c_S	Source distributed capacitance	F/m^2
T	Temperature	K
V_{DS}	Source-drain voltage	V
V_{GS}	Source-gate voltage	V

References

[1] E. MacChia, R. A. Picca, K. Manoli, et al., "About the amplification factors in organic bioelectronic sensors," *Materials Horizons*, vol. 7, pp. 999–1013, 2020. doi:10.1039/C9MH01544B

[2] A. Kyndiah, F. Leonardi, C. Tarantino, et al., "Bioelectronic Recordings of Cardiomyocytes with Accumulation Mode Electrolyte Gated Organic Field Effect Transistors," *Biosensors and Bioelectronics*, vol. 150, p. 111844, 2020. doi:10.1016/j.bios.2019.111844

[3] F. Torricelli, D. Z. Adrahtas, Z. Bao, et al., "Electrolyte-gated transistors for enhanced performance bioelectronics," *Nature Reviews Methods Primers 2021 1:1*, vol. 1, pp. 1–24, 2021. doi:10.1038/S43586-021-00065-8

[4] FORTUNE Business Insights, "The global semiconductor market," 2021.

[5] The Royal Swedish Academy of Science, "The Nobel Prize in Chemistry," 2000. www.kva.se

[6] D. Khodagholy, T. Doublet, P. Quilichini, et al., "In vivo recordings of brain activity using organic transistors," *Nature Communications*, vol. 4, 2013. doi:10.1038/ncomms2573

[7] S. R. Forrest, "Waiting for Act 2: What lies beyond organic light-emitting diode (OLED) displays for organic electronics?" *Nanophotonics*, vol. 10, pp. 31–40, 2020. doi:10.1515/nanoph-2020-0322

[8] P. Friederich, A. Fediai, S. Kaiser, et al., "Toward Design of Novel Materials for Organic Electronics," *Advanced Materials*, vol. 31, p. 1808256, 2019. doi:10.1002/ADMA.201808256

[9] G. Hong, X. Gan, C. Leonhardt, et al., "A Brief History of OLEDs—Emitter Development and Industry Milestones," *Advanced Materials*, vol. 33, p. 2005630, 2021. doi:10.1002/ADMA.202005630

[10] S. Forrest, *Organic electronics: foundations to applications*. Oxford University Press, 2020.

[11] M. J. Mirshojaeian Hosseini and R. A. Nawrocki, "A Review of the Progress of Thin-Film Transistors and Their Technologies for Flexible Electronics," *Micromachines 2021, Vol. 12, Page 655*, vol. 12, p. 655, 2021. doi:10.3390/MI12060655

[12] J. Wang, D. Ye, Q. Meng, C. a. Di, and D. Zhu, "Advances in Organic Transistor-Based Biosensors," *Advanced Materials Technologies*, vol. 5, p. 2000218, 2020. doi:10.1002/ADMT.202000218

[13] K. Feron, R. Lim, C. Sherwood, A. Keynes, A. Brichta, and P. C. Dastoor, "Organic Bioelectronics: Materials and Biocompatibility," *International Journal of Molecular Sciences 2018, Vol. 19, Page 2382*, vol. 19, p. 2382, 2018. doi:10.3390/IJMS19082382

[14] V. Naresh and N. Lee, "A Review on Biosensors and Recent Development of Nanostructured Materials-Enabled Biosensors," *Sensors 2021, Vol. 21, Page 1109*, vol. 21, p. 1109, 2021. doi:10.3390/S21041109

[15] M. Y. Mulla, L. Torsi, and K. Manoli, "Electronic biosensors based on EGOFETs," *Methods in Enzymology*, vol. 642, pp. 403–433, 2020. doi:10.1016/BS.MIE.2020.07.003

[16] Z. Bao and J. Locklin, "Organic Field-Effect Transistors," *Organic Field-Effect Transistors*, 2007. doi:10.1201/9781420008012

[17] L. Kergoat, L. Herlogsson, D. Braga, et al., "A water-gate organic field-effect transistor," *Advanced Materials*, vol. 22, pp. 2565–2569, 2010. doi:10.1002/ADMA.200904163

[18] R. A. Picca, K. Manoli, E. Macchia, et al., "Ultimately Sensitive Organic Bioelectronic Transistor Sensors by Materials and Device Structure Design," *Advanced Functional Materials*, vol. 30, pp. 1–23, 2020. doi:10.1002/adfm.201904513

[19] Y. S. T. M. T Minamiki, Y Hashima, "An electrolyte-gated polythiophene transistor for the detection of biogenic amines in water," *Chem. Commun.*, vol. 54, pp. 6907–6910, 2018.

[20] C. F. K. D. SP White, S Sreevatsan, "Rapid, selective, label-free aptameric capture and detection of ricin in potable liquids using a printed floating gate transistor," *ACS Sens.*, vol. 1, pp. 1213–1216, 2016.

[21] C. Cea, "Enhancement-mode ion-based transistor as a comprehensive interface and real-time processing unit for in vivo electrophysiology," *Nat. Mater.*, vol. 19, pp. 679–686, 2020.

[22] Z. Stojek, "The electrical double layer and its structure," *Electroanalytical Methods: Guide to Experiments and Applications*, pp. 3–9, 2010. doi:10.1007/978-3-642-02915-8{_}1/COVER/

[23] M. A. Brown, A. Goel, and Z. Abbas, "Effect of Electrolyte Concentration on the Stern Layer Thickness at a Charged Interface," *Angewandte Chemie*, vol. 128, pp. 3854–3858, 2016. doi:10.1002/ANGE.201512025

[24] M. Khademi and D. P. Barz, "Structure of the Electrical Double Layer Revisited: Electrode Capacitance in Aqueous Solutions," *Langmuir*, vol. 36, pp. 4250–4260, 2020. doi:10.1021/ACS.LANGMUIR.0C00024

[25] T. Cramer, A. Kyndiah, M. Murgia, F. Leonardi, S. Casalini, and F. Biscarini, "Double layer capacitance measured by organic field effect transistor operated in water," *Applied Physics Letters*, vol. 100, p. 143302, 2012. doi:10.1063/1.3699218

[26] T. Cramer, A. Campana, F. Leonardi, et al., "Water-gated organic field effect transistors-opportunities for biochemical sensing and extracellular signal transduction," pp. 3728–3741, 2013. doi:10.1039/c3tb20340a

[27] Y. Wang, Y. Song, and Y. Xia, "Electrochemical capacitors: mechanism, materials, systems, characterization and applications," *Chem. Soc. Rev*, vol. 45, p. 5925, 2016. doi:10.1039/c5cs00580a

[28] Y. H. Hung, T. C. Chang, Y. Z. Zheng, et al., "Investigation of Thermal Behavior on High-Performance Organic TFTs Using Phase Separated Organic Semiconductors," *IEEE Electron Device Letters*, vol. 42, pp. 859–862, 2021. doi:10.1109/LED.2021.3072410

[29] M. Di Lauro, S. Casalini, M. Berto, et al., "The substrate is a pH-controlled second gate of electrolyte-gated organic field-effect transistor," *ACS Applied Materials and Interfaces*, vol. 8, pp. 31 783–31 790, 2016. doi:10.1021/acsami.6b06952

[30] H. Šípová-Jungová, L. Jurgová, K. Mrkvová, N. S. Lynn, B. Špačková, and J. Homola, "Biomolecular charges influence the response of surface plasmon resonance biosensors through electronic and ionic mechanisms," *Biosensors and Bioelectronics*, vol. 126, pp. 365–372, 2019. doi:10.1016/j.bios.2018.11.002

[31] A. Goyal and M. T. Koper, "The Interrelated Effect of Cations and Electrolyte pH on the Hydrogen Evolution Reaction on Gold Electrodes in Alkaline Media," *Angewandte Chemie - International Edition*, vol. 60, pp. 13 452–13 462, 2021. doi:10.1002/anie.202102803

[32] F. Leonardi, A. An Tamayo, S. Casalini, and M. Mas-Torrent, "Modification of the gate electrode by self-assembled monolayers in flexible electrolyte-gated organic field effect transistors: work function vs. capacitance effects," 2018. doi:10.1039/c8ra05300f

[33] A. Kumatani, Y. Li, P. Darmawan, T. Minari, and K. Tsukagoshi, "On Practical Charge Injection at the Metal/Organic Semiconductor Interface." doi:10.1038/srep01026

[34] H. H. Choi, K. Cho, C. D. Frisbie, H. Sirringhaus, and V. Podzorov, "Critical assessment of charge mobility extraction in FETs," *Nature Materials 2017 17:1*, vol. 17, pp. 2–7, 2017. doi:10.1038/nmat5035

[35] A. Ortiz-Conde, F. J. García Sánchez, J. J. Liou, A. Cerdeira, M. Estrada, and Y. Yue, "A review of recent MOSFET threshold voltage extraction methods," *Microelectronics Reliability*, vol. 42, pp. 583–596, 2002. doi:10.1016/S0026-2714(02)00027-6

[36] W. S. P. o. t. IRE and u. 1952, "A unipolar" field-effect" transistor," *ieeexplore.ieee.org*. https://ieeexplore.ieee.org/abstract/document/4050836/

[37] C. R. Newman, C. Daniel Frisbie, D. A. Da, et al., “Introduction to organic thin film transistors and design of n-channel organic semiconductors,” *ACS Publications*, vol. 16, pp. 4436–4451, 2004. doi:10.1021/cm049391x

[38] C. Liao, M. Zhang, M. Y. Yao, T. Hua, L. Li, and F. Yan, “Flexible Organic Electronics in Biology: Materials and Devices,” *Advanced Materials*, vol. 27, pp. 7493–7527, 2015. doi:10.1002/ADMA.201402625

[39] J. Obrzut and K. A. Page, “Electrical conductivity and relaxation in poly(3-hexylthiophene),” *Physical Review B - Condensed Matter and Materials Physics*, vol. 80, 2009. doi:10.1103/PhysRevB.80.195211

[40] L. Weber and E. Gmelin, “Physics A "’ Transport Properties of Silicon,” *Appl. Phys. A*, vol. 53, pp. 136–140, 1991.

[41] R. A. Serway, *Principles of physics*. Saunders College Pub, 1998.

[42] P. A. Markowich, C. A. Ringhofer, and C. Schmeiser, *Semiconductor equations*. Springer Science & Business Media, 2012.

[43] S. Sze, Y. Li, and K. Ng, *Physics of semiconductor devices*. Wiley, 2021.

[44] M. Okereke and S. Keates, “Finite Element Mesh Generation,” *Springer Tracts in Mechanical Engineering*, pp. 165–186, 2018. doi:10.1007/978-3-319-67125-3{_}6

[45] N. Lu, W. Jiang, Q. Wu, D. Geng, L. Li, and M. Liu, “A Review for Compact Model of Thin-Film Transistors (TFTs),” *Micromachines*, vol. 9, 2018. doi:10.3390/MI9110599

[46] N. Delavari, K. Tybrandt, M. B. J. o. P. D. . . . , and u. 2021, “Nernst–Planck–Poisson analysis of electrolyte-gated organic field-effect transistors,” *iopscience.iop.org*, vol. 54, p. 415101, 2021. doi:10.1088/1361-6463/ac14f3

[47] K. Melzer, M. Brändlein, B. Brändlein, et al., “Characterization and simulation of electrolyte-gated organic field-effect transistors,” *Faraday Discussions*, p. 399, 2014. doi:10.1039/c4fd00095a

[48] D. Popescu, B. Popescu, M. Brändlein, K. Melzer, and P. Lugli, “Modeling of Electrolyte-Gated Organic Thin-Film Transistors for Sensing Applications,” vol. 62, pp. 4206–4212, 2015.

[49] N. Delavari, K. Tybrandt, G. Mattana, B. Piro, V. Noël, and I. Zozoulenko, “Modelling of Electrolyte-Gated Organic Field-Effect Transistor,” in *COMSOL Conference Camebridge*, 2019.

[50] A. Groß, “Theory of Solid/Electrolyte Interfaces,” 2020.

[51] H. Helmholtz, “Ueber einige Gesetze der Vertheilung elektrischer Ströme in körperlichen Leitern, mit Anwendung auf die thierisch-elektrischen Versuche (Schluss.),” *Annalen der Physik*, vol. 165, pp. 353–377, 1853. doi:10.1002/ANDP.18531650702

[52] D. Wang, V. Noël, and B. Piro, “Electrolytic Gated Organic Field-Effect Transistors for Application in Biosensors-A Review,” *Electronics*, vol. 5, p. 9, 2016. doi:10.3390/electronics5010009

[53] S. Jung, C. Kim, Y. B. J. o. P. D. . . . , and u. 2015, “Injection barrier at metal/organic semiconductor junctions with a Gaussian density-of-states,” *iopscience.iop.org*, 2015. doi:10.1088/0022-3727/48/39/395103

[54] G. Gomila, J. R. J. o. a. physics, and u. 1997, “Relation for the nonequilibrium population of the interface states: Effects on the bias dependence of the ideality factor,” *aip.scitation.org*, vol. 81, p. 2674, 1997. doi:10.1063/1.364305

[55] B. Burtscher, P. A. Manco Urbina, C. Diacci, et al., “Sensing Inflammation Biomarkers with Electrolyte-Gated Organic Electronic Transistors,” *Advanced Healthcare Materials*, vol. 10, 2021. doi:10.1002/ADHM.202100955

[56] Larissa Huetter, Adrica Kyndiah, and Gabriel Gomila, “Physical Modelling of Electrolyte Gated Organic Field Effect Transistors in the Nernst-Planck-Poisson framework.”

[57] Larissa Huetter, Adrica Kyndiah, and Gabriel Gomila, “Analytical Physical Modelling of Organic Metal-Electrolyte-Semiconductor Capacitors.”

[58] COMSOL, “Semiconductor Module User’s Guide,” Tech. Rep., 2018. www.comsol.com/

[59] *AC/DC Module User’s Guide*, 2019. www.comsol.com/blogs

[60] COMSOL, “Multiphysics Reference Manual,” 2019. www.comsol.com/blogs

[61] M. Bollhöfer, O. Schenk, R. Janalik, S. Hamm, and K. Gullapalli, “State-of-The-Art Sparse Direct Solvers. Parallel Algorithms in Computational Science and Engineering, Modeling and Simulation in Science, Engineering and Technology,” *SIAM Journal on Scientific Computing*, vol. 7, pp. 380–401, 2020.

[62] Larissa Huetter, Adrica Kyndiah, and Gabriel Gomila, “Analytical Physical Model for Electrolyte Gated Organic Field Effect Transistors in the Helmholtz Approximation Approximation.”

[63] T. Fujimoto and K. Awaga, “Electric-double-layer field-effect transistors with ionic liquids,” *Physical Chemistry Chemical Physics*, vol. 15, pp. 8983–9006, 2013. doi:10.1039/C3CP50755F

[64] K. Solodka, M. Berto, D. Ferraro, et al., “Detection of Neurofilament Light Chain with Label-Free Electrolyte-Gated Organic Field-Effect Transistors,” *Advanced Materials Interfaces*, 2022. doi:10.1002/ADMI.202102341

[65] P. A. Manco Urbina, M. Berto, P. Greco, et al., “Physical insights from the Frumkin isotherm applied to electrolyte gated organic transistors as protein biosensors,” *Journal of Materials Chemistry C*, vol. 9, pp. 10 965–10 974, 2021. doi:10.1039/D1TC02546E

[66] A.-M. Pappa, “Organic transistor arrays integrated with finger-powered microfluidics for multianalyte saliva testing,” *Adv. Healthc. Mater.*, vol. 5, pp. 2295–2302, 2016.

[67] C. Diacci, M. Berto, M. D. Lauro, et al., "Label-free detection of interleukin-6 using electrolyte gated organic field effect transistors," *avs.scitation.org*, vol. 12, p. 05F401, 2017. doi:10.1116/1.4997760

[68] K. Melzer, "Selective ion-sensing with membrane-functionalized electrolyte-gated carbon nanotube field-effect transistors," *Analyst*, vol. 139, pp. 4947–4954, 2014.

[69] E. Macchia, R. A. Picca, A. Tricase, C. D. Franco, and A. Mallardi, *Organic Bioelectronic Transistors: From Fundamental Investigation of Bio-Interfaces to Highly Performing Biosensors*, vol. 56, 2019. doi:10.21741/9781644900376-1

[70] D. Ohayon, "Biofuel powered glucose detection in bodily fluids with an n-type conjugated polymer," *Nat. Mater.*, vol. 19, pp. 456–463, 2020.

[71] M. Di Lauro, S. Casalini, M. Berto, et al., "The substrate is a pH-controlled second gate of electrolyte-gated organic field-effect transistor," *ACS Applied Materials and Interfaces*, vol. 8, pp. 31 783–31 790, 2016. doi:10.1021/ACSAMI.6B06952

[72] N. Lago, N. Wrachien, M. G. Pedersen, and A. Cester, "Simultaneous stimulation and recording of cell activity with reference-less sensors: Is it feasible?" *Organic Electronics*, vol. 62, pp. 676–684, 2018. doi:10.1016/J.ORGEL.2018.07.007

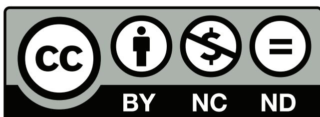

This document - excluding the cover, pictures, tables and graphs - is licensed under the Creative Commons Attribution-NonCommercial-NoDerivs 4.0 International License (CC BY-NC-ND 4.0): https://creativecommons.org/licenses/by-nc-nd/4.0/